Climate change analysis from the TOA spectrally resolved IR radiation

By

Fang Pan

A dissertation submitted in partial fulfillment
of the requirements for the degree of
Doctor of Philosophy
(Atmospheric, Oceanic, and Space Science)
in the University of Michigan
2017

Doctoral Committee:

Associate Professor Xianglei Huang, Chair

Assistant Professor Kerri Pratt

Professor Richard B. Rood

Professor Christopher Ruf

Fang Pan

fangpan@umich.edu

ORCID iD: 0000-0003-2113-8319

Acknowledgement

This thesis would not be brought into fruition without the engagement of numerous people. I am indebted to all the kindly help I received!

There are no proper words to convey me deep gratitude and respect to my advisor, Professor Xianglei Huang. Without his support, patience and generosity I would not have finished this study. Professor Huang has also shown me an excellent role model of righteousness and professionalism that will benefit me in the long-term career.

I would also like thank my other dissertation committee members: Professors Christopher Ruf, Richard B. Rood, and Kerri Pratt for their time to evaluate my research work. I also greatly appreciate Dr. Stephen Leroy for his support and guidance in my research.

I am grateful to my classmates and colleagues who have taken me many delightful experiences inside and outside of the CLaSP. I would not forget the wonderful time we have spent wonderful time together and I really enjoy your company which makes my PhD life much more enjoyable. Thank you, my dear friends.

Last but not least, many thanks to my dear family. Without your unconditional support and confidence in me I wouldn’t have been here today. Your encouragement accompany me all the years, I love you.

Table of Content

List of Figures

List of Tables

Abstract

Radiation plays a central role in the global energy budget. It is closely intertwined with atmospheric dynamics and cloud microphysics that lie at the heart of global climate change studies. On the other hand, radiation is not merely a type of energy flux. It is spectrally dependent, and such spectrally resolved radiation contains detailed information about geophysical variables. Recently more and more high-quality measurements of top-of-atmosphere (TOA) longwave radiation at very high spectral resolution (~1cm^{-1} or higher; a.k.a. hyperspectral measurements) have become available. Motivated by such measurements, in particular by their perspectives for climate studies, this thesis explores which new insights into the climate change and variability we could draw from the spectral dimension of such measurements and their counterparts based on model simulation and reanalysis data.

First the spectrally resolved radiances in stratospheric channels observed by AIRS (Atmospheric infrared Sounder) over the last decade have been examined. Their secular trends are estimated and compared with counterparts of two sets of synthetic AIRS radiances. One set was generated using atmospheric profiles from the free-running GFDL AM3 forced by the observed sea surface temperature and the other using ECMWF ERA-interim reanalysis. AIRS lower-stratospheric channels exhibit a cooling trend of brightness temperature no more

than 0.23 K decade^{-1} while its middle- and upper-stratospheric channels consistently show a statistically significant cooling trend of brightness temperature as large as 0.58 K decade^{-1}. Neither of the synthetic radiances is capable of capturing these trends.

Optimal fingerprinting technique is further applied to the trends of radiances in AIRS stratospheric channels and in AMSU stratospheric channels to derive global-mean temporal changes of stratospheric temperature and CO_2 due to anthropogenic activities (so-called average-then-retrieve approach). The retrievals are not only consistent with trend estimates using other data sets such as layer-mean stratospheric temperature observations by SSU but also improve the vertical resolution of such temperature trend estimates. Furthermore, synergistic use of microwave radiances effectively helps to disentangle covariance of the temperature and CO_2 changes.

Traditionally, radiative feedbacks have been considered regarding the perturbation to broadband flux. Because of the compensating biases among spectral bands, it is possible that global climate models (GCMs) produce similar broadband feedback but the spectral decomposition of such broadband feedback can be considerably different, implying various changes of geophysical variables leading to such seemingly agreement in the broadband feedback. Spectral relative humidity (RH) longwave feedbacks of CMIP5 GCMs are calculated and then are analyzed utilizing the spectral RH radiative kernels. The spectral and spatial compensations lead to a consistent and nearly zero RH broadband feedback among models, usually referred to as “constant RH” concerning global warming. Further analysis

reveals that spectral details in RH feedbacks can provide more information about the changes of geophysical variables than the broadband RH feedback does.

Similar to the trend-detections studies for the stratospheric temperatures and CO_2, the hyperspectral measurements also have the potential for providing constraints on the changes of temperature, humidity, and cloud properties in the troposphere using the average-then-retrieve approach. Meanwhile, more than a decade of hyperspectral data also provides a new opportunity to test climate models more rigorously by comparing the spectrally resolved radiances. Discrepancies in such comparison can be more attributable to the causes than those in broadband comparison, thus bridging the model assessments in the radiation field and in the geophysical field.

Chapter 1

Introduction

1.1 Hyperspectral measurements and potentials of their retrievals

Over the last 15 years, space-borne earth observations were featured with a new generation of hyperspectral instruments such as the Atmospheric Infrared sounder (AIRS) aboard NASA Aqua launched in 2002 (Chahine et al., 2006), Cross-track Infrared Sounder (CrIS) aboard Suomi NPP launched in 2011 (Han et al., 2013), and the Infrared Atmospheric Sounding Interferometer (IASI) aboard Eumetsat Metop-A launched in 2006 (Hilton et al., 2012). Such instruments measure spectrally resolved outgoing longwave radiation with high spectral resolution and pinpoint accuracy. The performances of these instruments have been shown to be excellent and stable. Having taken for an example the AIRS, the initial in-flight calibrations estimated a radiometric accuracy of 0.3K or higher for a target with 250K brightness temperature (Pagano et al. 2003), as well as a spectral accuracy of 0.01 of the full width at half maximum of each channel (Gaiser et al. 2003). Aumann et al. (2006) estimated the calibration accuracy to be better than 0.2K and the stability to be better than 16×10^{-3}K per year. Later Aumann and Pagano (2008) updated the stability estimate to ~4×10^{-3}K per year. AIRS collects ~3 million spectra per day and can achieve global coverage within 2 days. Such unprecedentedly extensive, accurate and stable measurements of spectral radiances in

the thermal-IR, together with the geophysical retrieval products based on the radiances, advance our capacity of assimilating satellite data for the weather forecast, improve our understanding to the changing climate, and can be valuable data set for testing climate models.

A great amount of work has taken the advantage of the high-spectral-resolution radiance measurements to estimate the temperature and humidity profiles with higher vertical resolution and better accuracy than what the previous generation of satellite sounders can provide. It has become possible to retrieve the concentration of several minor gases contributing to Earth sciences and available data sets (Marshall et al., 2006). Improvement in weather forecast has been demonstrated by the assimilation of AIRS retrieval product. Atlas (2005) assimilated the retrieved temperature profiles into FVDAS (Finite Volume Data Assimilation System) and showed an improvement in forecasting the intensity and position of cyclones. SPoRT (Short-term Prediction Research and Transition) center found that assimilation of temperature and moisture profiles into regional models can enhance prediction of pressure anomalies and rainfall (Zavodsky et al., 2007). In climate study, AIRS data also provides valuable source of global 3D moisture field for the model validation of climatology. Using AIRS data to evaluate major climate models, Pierce et al. (2006) suggested systematic model errors of drier pattern in the tropics below 800hPa while moister conditions between 300-600hPa in the extra tropics. Additionally, preliminary assessment of AIRS temperature trends also has been presented for insight into climate changes (Molnar & Susskind, 2007). In regards to the atmospheric composition, AIRS retrievals provide means to understand and monitor the distribution, transportation and trends of trace gases like CO_2,

CO, and SO_2 (Aumann et al., 2005; Chahine et al., 2008; McMillan et al., 2005; Tiwari et al., 2006; Wright et al., 2005).

1.2 Direct exploitation of hyper-spectral radiances

In addition to the retrievals from the hyper-spectral measurements, extensive spectral information in the hyperspectral radiances can be directly exploited for the climate studies and model evaluations.

1.2.1 Detection of climate changes

Usually, the detection of climate changes is performed in two stages: the first stage is to retrieve the atmospheric profiles, cloud and surface properties from the satellite observations and then the second stage is to estimate how the averages of these instantaneous retrievals change with time, usually referred to as retrieve-then-average approach. The retrieve-then-average approach faces some difficulties in how to trace error propagation from the instantaneous retrieval of the individual footprint to final conclusions about climate change or climate data records. Changes in instrument calibration, secular drift in stability, and *a priori* constraints used for the retrievals can all contribute to the retrieval errors. The complexity of retrieval algorithm could further make it more challenging to evaluate the error propagations, especially if the error is time-dependent (Kato et al., 2014). A complimentary approach is to first average the radiances over time and space and then directly relate the anomalies of hyper-spectral radiances to the changes of atmospheric properties (hereafter referred as average-then-retrieve approach).

There are three assumptions in the average-then-retrieve approach. They have been validated for certain spatial and temporal scales by Kato et al. (2010; 2014) and are as follows:

1) Averaged TOA spectral radiance change can be well-approximated by a linear combination of spectral radiance changes caused by cloud and atmospheric properties;

2) The magnitude of spectral radiance changes linearly corresponding to a small perturbation of cloud or atmospheric property, at least in the relevant parts of the spectrum;

3) Changes of atmospheric properties provide unique spectral radiance that can be separated by a linear regression approach. In terms of relating the changes of atmospheric, surface and cloud properties with the spectral anomalies, it is based on the detection of a predicted signal emerging from the noisy time series (Goody et al., 1998). Santer et al. (1996) and Leroy (1998) had done some preliminary explorations for the optimal detection of signals. (For our purpose, the signals are the sensitivity of TOA hyper-spectral radiances to the changes of atmospheric properties.) Afterward, the average-then-retrieve approach has been applied to synthetic infrared radiance. It helped to study the longwave spectral forcing and feedbacks (Leroy et al., 2008; Huang et al., 2010a & 2010b) as well as to synthetic shortwave spectral radiances to study the variations of climate parameters (Feldman et al., 2011; Jin et al., 2011). This thesis research applies the average-then-retrieve approach to observed infrared radiances and microwave radiances, i.e., AIRS radiances in the CO_2 ν_2 band and AMSU radiances in channel 10-14 to detect the secular trend of stratospheric temperatures and CO_2.

1.2.2 Evaluation of model simulations

As far as model evaluation is concerned, the conventional approach is to retrieve the model-equivalent geophysical products from the satellite measurements for the sake of comparison. However, this approach is limited by various assumptions and *a priori* input used in the retrieval process. The alternative approach is to feed simulated atmospheric profiles to a forward model to produce synthetic radiances and then to compare with observed radiances (usually referred as satellite simulator; e.g. Bodas-Salcedo et al., 2011). The spectrally resolved radiation can provide more valuable information for model diagnostics than broadband OLR (outgoing longwave radiation) fluxes. The seemingly good agreement of broadband fluxes between model simulations and the observations could be due to the compensating biases from different spectral bands. On the contrary, spectral details in the radiances can expose the signatures associated with particular climate processes masked by the broadband fluxes. Thus, one straightforward and strict method to test a climate model with higher level confidence is to compare the simulations and observations on the spectral dimension (Huang et al., 2002, 2006). Huang et al. (2006) used IRIS (Infrared interferometer Spectrometer) spectra to quantify the bias in GFDL (Geophysical Fluid Dynamical Laboratory) AM2-simulated clear-sky OLR. Against the AIRS observations, Huang et al. (2007) then examined the GFDL AM2-simulated clear-sky and cloudy-sky spectra. They found the existence of radiance biases of opposite signs in different regions which suggest a seemingly good agreement of the model's broadband longwave flux with observations may be due to a fortuitous cancellation of spectral errors. In this thesis research, we compare the spectrally resolved radiances in stratospheric channels observed by AIRS over the last decade

with counterparts of two sets of synthetic radiances. One set was generated using atmospheric profiles from the free-running GFDL AM3 forced by the observed sea surface temperature and the other using ERA-interim reanalysis. The comparison would demonstrate whether the model simulations or reanalysis can capture the observed stratospheric changes.

The spectral discrepancies between the satellite measurements and the synthetic simulations are resulted from the biases of geophysical variables, such as temperature, humidity, cloud and surface properties in models. To identify such error biases in models, it is also feasible to utilize the same average-then-retrieve approach as in the detection of climate changes. Their underlying objectives are the same, namely, attributing differences in radiances to anomalies in associated geophysical variables. For instance, when one uses the spectral radiance difference of two time periods, if we can quantitatively relate contributions of these variables to the spectral radiance changes, we can infer how these variables change between the two time periods. Similarly, when the differences between observed and simulated spectral radiances are made available, we could infer the discrepancies in temperature, humidity, and cloud properties between model and observation, as long as we can separate contributions of bias errors in the model inputs to the spectral radiance differences. For example, to validate the forecast capability of the CGEM (Canadian Global Environmental multi-scale) model at the radiance level, Bani et al. (2016) assessed the radiance biases in synthetic spectra from short-term CGEM forecast against the AIRS observations. They successfully identified the contribution of the biases of surface temperature and atmospheric temperature, atmospheric humidity and clouds to the radiances biases.

In the context of climate change, another essential metric element to the assessment of models is radiative feedback, including humidity feedback, lapse rate feedback, and cloud feedback. Traditionally such radiative feedbacks are studies in terms of broadband flux. However, radiative feedbacks have an intrinsic dimension of spectrum. Because of the compensating biases among spectral bands, it is possible that some global climate models (GCMs) produce similar broadband feedback but the spectral decomposition of such broadband feedback can be considerably different. Therefore, Huang et al. (2014) developed the spectral radiative kernel method to compute the longwave spectral radiative feedbacks. They found that the lapse rate and longwave water vapor feedbacks reveal spectrally dependent difference among GCMs. Taking relative humidity (RH) feedback as an example, this thesis research calculates spectral RH feedbacks in 16 GCMs and explores what extra information can be inferred from the spectral dimension of the RH radiative feedbacks.

1.3 Motivations and research objectives

The theme of this thesis is to explore what new insights about climate change and climate variability can be gleaned from spectrally resolved measurements, such as the AIRS and their counterparts of synthetic radiances based on model simulation or reanalysis. For climate change study, here we focus on the detection of stratospheric changes. Using forward model PCRTM (Principle Component-based Radiative Transfer Model, Liu et al., 2006) we generated two sets of synthetic radiances, one set using atmospheric profiles from the free-running GFDL AM3 and the other using ERA-interim reanalysis, and then compare them with observed radiances by AIRS in the CO_2 v_2 band. The average-then-retrieve approach is

applied to the radiance trends observed by AIRS to detect the changes of stratospheric temperature and CO_2. In addition, we also explore the novel use of spectral dimension of climate feedbacks in which the average-then-retrieve approach is also applied to the changes in simulated radiances. Through these explorations of observed and simulated hyper-spectral radiances, this thesis strives to address the following questions:

1. Can any statistically significant linear trends already be detected from certain AIRS channels that are sensitive to absorptions and emissions in the stratosphere?

2. Do the synthetic spectral radiances based on model simulations and reanalysis fully agree with observations?

3. Can we directly estimate the changes of stratospheric temperature and CO_2 from the observed time series of averaged radiances by AIRS? How can synergistic measurements improve such estimates?

4. Although globally averaged broadband RH feedbacks in all GCMs are close to zero, will they also show same consistency in the spectral details of the RH feedbacks?

5. Can we quantitatively relate the changes of relative humidity profiles with the spectral RH radiative feedbacks?

Rest chapters of this thesis are organized as follows. Chapter 2 examines the secular trends in the radiances observed by AIRS in the CO_2 v_2 band and compares them with the synthetic radiances based on GFDL AM3 model simulations and ERA-interim reanalysis. Chapter 3 detects the changes of stratospheric temperature and CO_2 directly from the

observed radiances by AIRS. Chapter 4 explores the spectral relative humidity feedbacks among 16 CMIP5 GCMs and retrieves the RH profiles from the changes of simulated spectral radiances. Finally, the summary of these findings and thoughts on future work is presented in Chapter 5.

Reference

1. Aumann, H. H., M. T.Chahine, C.Gautier, M. D.Goldberg, E.Kalnay, L. M.McMillin and J.Susskind, 2003: AIRS/AMSU/HSB on the Aqua mission: Design, science objectives, data products, and processing systems. *IEEE Trans. Geosci. Remote Sens.*, **41**(2), 253–264, doi:10.1109/TGRS.2002.808356.

2. Aumann H. H., D. Gregorich, S. Gaiser 2005, AIRS hyper-spectral measurements for climate research: Carbon dioxide and nitrous oxide effects, *Geophys. Res. Lett*., **32**, L05806, doi:10.1029/2004GL021784.

3. Aumann, H. H., S. Broberg, D. Elliott, S. Gaiser, and D. Gregorich, 2006: Three years of AIRS radiometric calibration validation using sea surface temperatures, *J. Geophys. Res.*, **111**, D16S90, doi:10.1029/2005JD006822.

4. Aumann, H. H., and T. S. Pagano, 2008: Using AIRS and IASI data to evaluate absolute radiometric accuracy and stability for climate applications. *Proc. SPIE Int. Soc. Opt. Eng.*, **7085**, doi: 10.1117/12.795225.

5. Bani Shahabadi, Maziar., et al., 2016, Validation of a weather forecast model at radiance level against satellite observations allowing quantification of temperature, humidity, and cloud-related biases. *Journal of Advances in Modeling Earth Systems* **8**(3): 1453-1467.

6. Bodas-Salcedo, A., et al., 2011, COSP: Satellite simulation software for model assessment, *Bull. Am. Meteorol. Soc.*, **92**, 1023–1043, doi:10.1175/2011BAMS2856.1.

7. Chahine, M. T., and Coauthors, 2006: AIRS: Improving weather forecasting and providing new data on greenhouse gases. *Bull. Amer. Meteor. Soc*., **87**, 911–926, doi:10.1175/BAMS-87-7-911.

8. Chahine, M.T. et al., 2008, Satellite Remote Sounding of Mid-Tropospheric CO_2, *Geophys. Res. Lett.*, **35**, doi:10.1029/2008GL035022.

9. Feldman, D. R., C. A. Algieri, J. R. Ong, and W. D. Collins, 2011, CLARREO shortwave observing system simulation experiments of the twenty-first century: Simulator design and implementation. *J. Geophys. Res*., **116**, D07107, doi:10.1029/2010JD015350.

10. Goody, R., Anderson, J., and North, G., 1998, Testing climate models: An approach. *Bulletin of the American Meteorological Society*, **79**(11), 2541-2549.

11. Han, Y., and Coauthors, 2013: *Suomi NPP* CrIS measurements, sensor data record algorithm, calibration and validation activities, and record data quality. *J. Geophys. Res. Atmos.,* **118,** 12 734–12 748, doi:10.1002/2013JD020344.

12. Hilton, Fiona, et al., 2012, Hyperspectral Earth observation from IASI: Five years of accomplishments." *Bulletin of the American Meteorological Society* **93**(3), 347-370, doi:10.1175/BAMS-D-11-00027.1.

13. Huang, X.L., J. Farrara, S. S. Leroy, Y. L. Yung, and R. M. Goody, 2002, Cloud Variability as Revealed in Outgoing Infrared Spectra: Comparing Model to Observation with Spectral EOF Analysis, *Geophys. Res. Lett.*, **29**, doi:10.1029/2001GL014176.

14. Huang, X.L., V. Ramaswamy, and M.Daniel Schwarzkopf, 2006, Quantification of the source of errors in AM2 simulated tropical clear-sky outgoing longwave radiation, *J. Geophys. Res*, **111**, D14107, doi:10.1029/2005JD006576.

15. Huang, X., X. Chen, B. J. Soden, and X. Liu, 2014, The spectral dimension of longwave feedback in the CMIP3 and CMIP5 experiments, *Geophys. Res. Lett.*, **41**, 7830–7837, doi:10.1002/2014GL061938.

16. Huang, Y., Ramaswamy, V., Huang, X.L., Fu, Q., Bardeen, C., 2007, A strict test in climate modeling with spectrally resolved radiances: GCM simulation versus AIRS observations, *Geophys. Res. Lett.*, **34**(24), L24707.

17. Huang, Y., S. Leroy, P. J. Gero, J. Dykema, J. Anderson, 2010a, Separation of Longwave Climate Feedbacks from Spectral Observations, *J. Geophys. Res.*, **115**, D07104, doi:10.1029/2009JD012766.

18. Huang, Y., S. S. Leroy, J. G. Anderson, 2010b, Determining longwave forcing and feedback using infrared spectra and GNSS radio occultation, *J. Climate*, **23**, 6027-6035, doi:10.1175/2010JCLI3588.1.

19. Jin, Z., B. A. Wielicki, C. Loukachine, T. P. Charlock, D. Young, S. Noel, 2011: Spectral kernel approach to study radiative response of climate variables and interannual variability of reflected solar spectrum. *J. Geophys. Res*., **116**, D10113, doi:10.1029/2010JD015228.

20. Kato, S., et al., 2011: Detection of atmospheric changes in spatially and temporally averaged infrared spectra observed from space, *J. Climate*, **2**4, 6392-6407, doi: 10.1175/JCLI-D-10-05005.1.

21. Kato, S., et al., 2014, Retrieval of atmospheric and cloud property anomalies and their trend from temporally and spatially averaged infrared spectra observed from space. *J. Climate*, **27**(12), 4403-4420, doi:10.1175/JCLI-D-13-00566.1.

22. Le Marshall, J., et al., 2006, Improving global analysis and forecasting with AIRS. *Bulletin of the American Meteorological Society* **87**(7), 891-894, doi:10.1175/BAMS-87-7-891.

23. Leroy, S. S., 1998, Detecting climate signals: Some Bayesian aspects, *J. Climate*, **11**, 640-651.

24. Leroy, S., J. G. Anderson, J. Dykema, and R. Goody ,2008, Testing climate models using thermal infrared spectra, *J. Climate*., **21**, 1863-1875.

25. Liu, X., W. L. Smith, D. K. Zhou and A. Larar, 2006, Principal component-based radiative transfer model for hyperspectral sensors: theoretical concept, *Applied optics*, **45**, 201-209, doi:10.1364/AO.45.000201.

26. McMillan W. W., et al., 2005, Daily global maps of carbon monoxide from NASA's Atmospheric Infrared Sounder, *Geophys. Res. Lett*., **32**, L11801, doi:10.1029/2004GL021821.

27. Molnar, G.I. and Susskind, J., 2007, Utility of AIRS retrievals for climate studies. P*roc. SPIE* **6565**, Algorithms and Technologies for Multispectral, Hyperspectral, and Ultraspectral Imagery XIII, 65651I, doi:10.1117/12.718466

28. Pierce D. W., T. P. Barnett, E. J. Fetzer, P. J. Gleckler, 2006, Three-dimensional tropospheric water vapor in coupled climate models compared with observations from the AIRS satellite system, *Geophys. Res. Lett*., **33**, L21701, doi:10.1029/2006GL027060.

29. Santer, B. D., T. M. L. Wigley, T. P. Barnett, and E. Anyamba, 1996, Detection of climate change and attribution of causes. Cambridge University Press, Cambridge, United Kingdom and New York, NY, USA, 407–444.

30. Wright, R., Carn, S. A., Flynn, L. P., 2005, A satellite chronology of the May-June 2003 eruption of Anatahan volcano, *Journal of Volcanology and Geothermal Research*, **146**, 102-116. doi: 10.1016/j.jvolgeores.2004.10.021.

31. Zavodsky, B.T., Chou, S.H., Jedlovec, G. and Lapenta, W., 2007, The impact of atmospheric infrared sounder (AIRS) profiles on short-term weather forecasts. *Proc. SPIE* **6565**, Algorithms and Technologies for Multispectral, Hyperspectral, and Ultraspectral Imagery XIII, 65651J, doi:10.1117/12.718121.

Chapter 2

Linear trends and closures of 10-year observations of AIRS stratospheric channels

The material of this chapter was published in

Pan, F., Huang, X., Strow, L.L. and Guo, H., 2015. Linear trends and closures of 10-yr observations of AIRS stratospheric channels. *J. Clim.*,28(22), doi: 10.1175/JCLI-D-1500418.1.

2.1. Introduction

Stratospheric cooling over last several decades, especially its relation with global warming, has been extensively studied using both observations and numerical models. The observational data sets used in such trend studies include radiosonde observations as well as microwave observations from multiple satellites, namely MSU (Microwave Sounding Unit), AMSU (Advance Microwave Sounding Unit), and SSU (Stratospheric Sounding Unit). These observations inevitably suffer from various issues such as the calibration of radiometers, the drift of orbits, and the stability of instruments. The cooling trend is detectable from such satellite observations, although considerable uncertainties still exist in the estimation of magnitudes (Ramaswamy et al. 2001, Seidel et al. 2011, Thompson et al. 2012, and

references there-in). A large amount of efforts then had to be invested in making these data sets climate-quality data records, as discussed by Zou et al. (2006; 2009; 2010; 2011) and RSS (Remote Sensing Systems) team (Mears et al. 2009; 2011). Climate model simulations are also useful in such studies, especially for the detection and attribution studies (e.g., Shine et al. 2003, Ramaswamy et al. 2006, and Forster et al. 2011). Reanalyses, on the other hand, are suffering from issues such as data inhomogeneities and time-dependent biases in observation systems, making them not well suited for trend analysis of the stratospheric temperature (Thorne and Vose 2010).

A potentially valuable data set for investigating stratospheric temperature trend and variability is AIRS (Atmospheric infrared Sounder) aboard NASA Aqua satellite launched in 2002 (Pagano et al. 2003). The AIRS L1b (Level-1b) radiances have been shown to be well calibrated and have little secular drift since it started to record hyperspectral radiances in September 2002 (Aumann and Pagano 2008). Given the rich information contained in the AIRS spectrum, more than a decade of global observations with dense sampling patterns, and the good performance in calibration and stability, a few meaningful questions can be investigated using the AIRS data are:

(1) Can any statistically significant linear trends be detected already from certain AIRS channels that are sensitive to absorptions and emissions in the stratosphere (hereafter, for brevity, referred as stratospheric channels)? Note this is about the linear trend during the period of AIRS observation. Such linear trend might be attributed to not only anthropogenic

climate change but also decadal climate variability (e.g. stratospheric temperature variability due to solar cycle).

(2) Are such statistically significant trends, if exist, consistent with the trends of AIRS L2 (level-2) retrievals? In another word, as far as the trend is concerned, does a closure exist between AIRS L1 and L2 data products, at least in terms of globally averaged quantities?

(3) Can free-running climate models forced by observed sea surface temperatures (SSTs) and CO_2 concentrations over the same period reproduce the trends in AIRS stratospheric channels? How about reanalysis?

This study is motivated by above questions and we carry out both data analysis and model simulations to investigate these questions. The rest of this chapter is arranged as follows. Section 2.2 describes AIRS L1b calibrated radiances and L2 retrievals, GFDL CM3 model, and ERA-interim reanalysis, as well as the spectral radiative kernels. The linear trends of brightness temperatures of stratospheric channels in the CO_2 ν_2 band are showed and discussed in Section 2.3. Section 2.4 presents conclusions and further discussions.

2.2. AIRS data and its processing, forward model, and synthetic AIRS radiances

We have processed and archived 10-year AIRS data from January 2003 to December 2012. As a comparison, synthetic AIRS radiances are simulated using two data sets as input to a radiative transfer model: one is simulations by a free-running GFDL (Geophysical Fluid Dynamics Laboratory) AM3 model forced by the observed SST over the same period, and the other is ECMWF (European Centre for Medium-Range Weather Forecasts) ERA-interim

reanalysis. This section will introduce the data processing of AIRS radiances, the GFDL AM3 model and ECMWF ERA-interim reanalysis, as well as the radiative transfer tools used in following sections.

2.2.1 AIRS measurements and L1b data processing

AIRS is a grating spectrometer with 2378 channels. The spectral coverage is from 3.7μm to 15.4μm with gaps in between. Its resolving power ($\lambda/\delta\lambda$) is 1200, i.e., ~0.5cm^{-1} spectral resolution in the CO_2 v_2 fundamental band (also known as the 15μm band). The initial in-flight calibrations estimated a radiometric accuracy of 0.3K or higher for a target with 250K brightness temperature (Pagano et al. 2003), as well as a spectral accuracy of 0.01 of the full width at half maximum of each channel (Gaiser et al. 2003). Aumann et al. (2006) estimated the calibration accuracy to be better than 0.2K and the stability to be better than 16x10^{-3}K per year. Aumann and Pagano (2008) updated the stability estimate to ~4x10^{-3}K per year. AIRS collects ~3 million spectra per day and can achieve global coverage within 2 days. It has been operating since September 2002. Such accuracy, stability, dense spatial coverage, and long-term record from one single instrument makes AIRS radiances an attractive data set in the studies of stratospheric variability and trend.

In this study we examine 10 years of AIRS L1b calibrated radiances from January 2003 to December 2012. Following Huang and Yung (2005), we apply quality controls to each AIRS spectrum to detect abnormal channels. For each AIRS scanning cycle, the AIRS spectra within ±5° scanning angle (cos5°=0.996) are averaged and deemed as a nadir-view spectrum. Such nadir-view spectra are then averaged onto 2.5° longitude by 2° latitude grid

boxes. The averaging onto the grid boxes is done separately for the descending node and the ascending node. Then for every 16 days (i.e. the repeating period for Aqua satellite) of observations, results of the descending node and ascending node are equally averaged to attain a 16-day average. By doing this, we can minimize any sampling disparity between the ascending and descending nodes. Figure 2.1 shows the

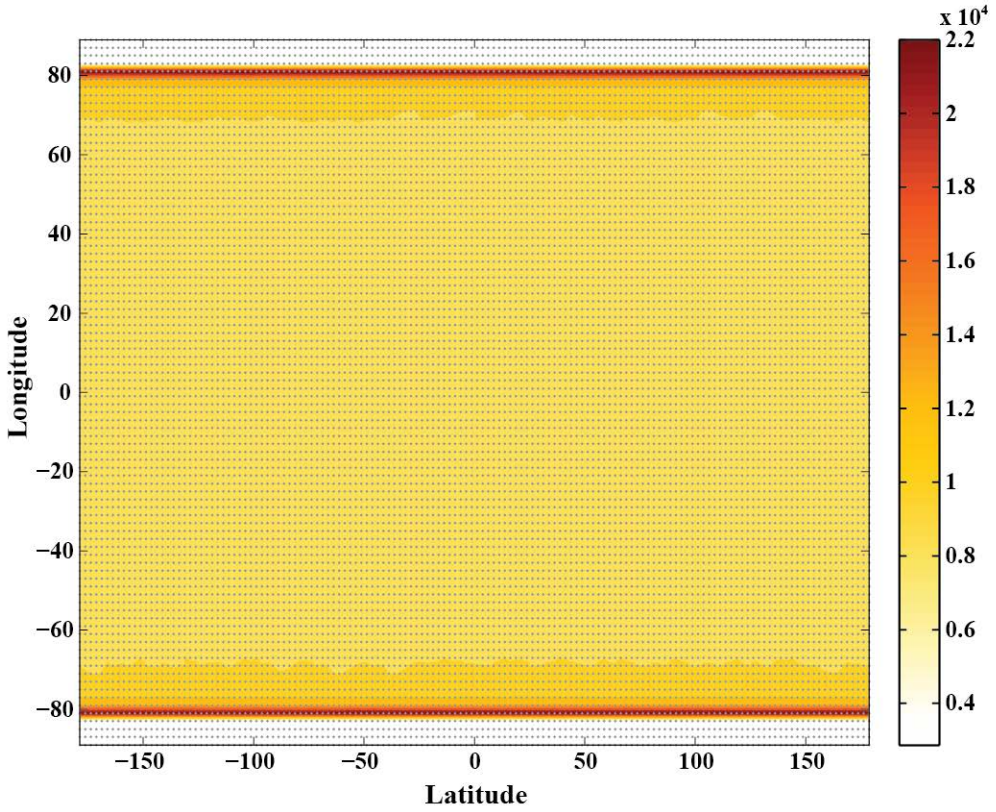

Figure 2.1. Number of qualified AIRS spectra used for averaging over the entire year of 2004 in each 2.5°×2° grid box. The spatial sampling is essentially uniform for each latitude zone.

number of qualified spectra used for average in each grid box for the entire year of 2004.

The sampling is essentially uniform for each latitude band within ±81°, beyond which there is no AIRS nadir-view observation. The number of observations increases considerably

as the sun-synchronous satellite Aqua approaches its north and south boundaries. This is why the numbers of qualified spectra in 81°S-79°S and 79°N-81°N latitudinal bands are much larger than the rest.

We focus on global-mean spectra. Moreover, we only focus on channels in the CO_2 15μm band that are most sensitive to the stratospheric absorption and emission. 50 AIRS channels between 662.5 and 674.9cm^{-1} are chosen because the peaks of their weighting functions (i.e. the derivation of their transmission function with respect to the pressure) locate in the stratosphere (between 1hPa and 100hPa). These channels are affected little by the variations of the tropospheric clouds. We do not choose channels in the CO_2 ν_3 fundamental band because they can be affected by solar radiation in addition to thermal emission and absorption. As an example, Fig. 2.2 shows time series of such global-mean brightness temperature anomalies (deseasonlized deviations from long-term global means) of two stratospheric channels used in our analysis. One channel is 666.02cm^{-1} sensitive to the absorption and emission in the lower stratosphere and the other is 667.78cm^{-1} sensitive to the middle-stratospheric absorption and emission.

2.2.2 Synthetic AIRS radiances

In parallel to the AIRS radiance observations, we analyze synthetic AIRS radiances computed using a state-of-the-art radiance simulator (Chen et al. 2013) based on the PCRTM (Principle Component-based Radiative Transfer Model, Liu et al. 2006). The PCRTM is a fast and accurate radiative transfer model that has been widely used in hyperspectral sounding community. Chen et al. (2013) developed a radiance simulator based on the

PCRTM, which is tailored for climate model output as well as reanalysis data and is able to take sub-grid variability of clouds into account. More details can be found in Chen et al. (2013).

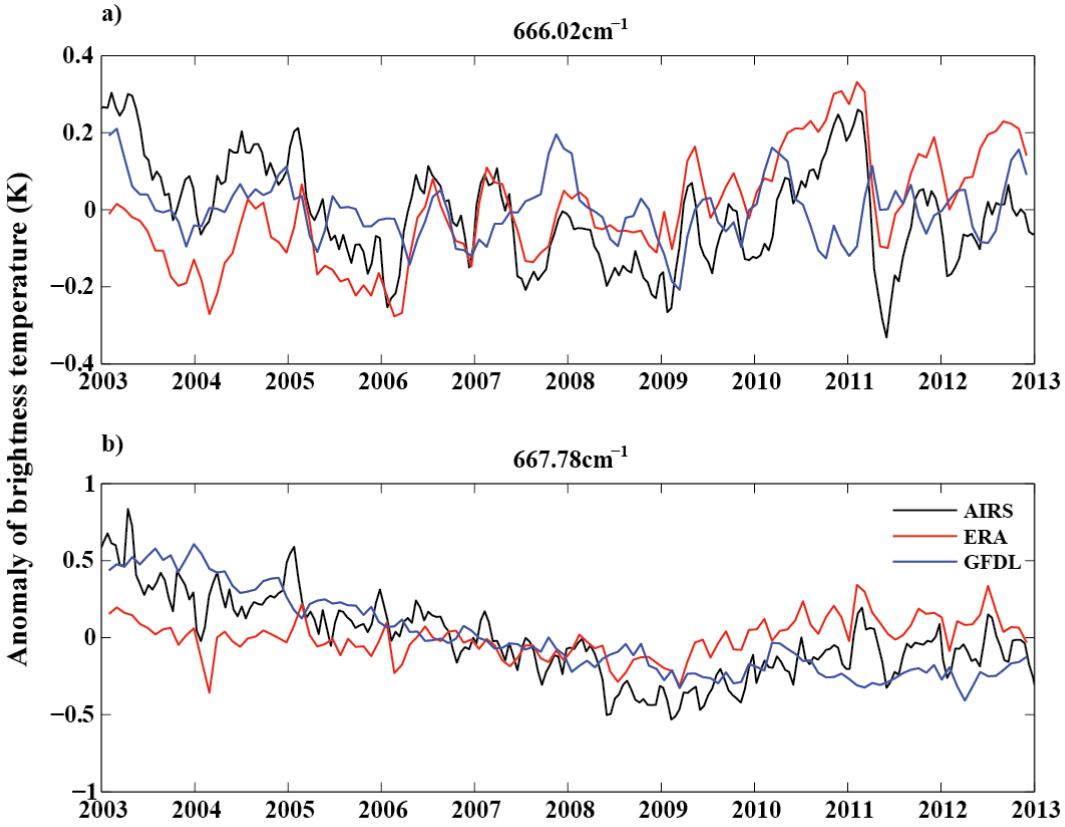

Figure 2.2. Time series of global-mean brightness temperature anomalies of two channels (a) 666.02cm^{-1} (weighting function peaks at ~66hPa) and (b) 667.78cm^{-1} (weighting function peaks at ~2hPa). Black line is AIRS observation. Red and blue lines show the synthetic AIRS radiance based on ERA-interim reanalysis and GFDL AM3 simulation, respectively.

We generate two sets of synthetic AIRS radiance datasets. One is based on 6-hourly output from a GFDL AM3 model run forced by the observed SST from 2003 to 2012. The AM3 model (Donner et al. 2011) is the latest atmospheric GCM developed by the GFDL. The horizontal resolution is 2.5° longitude by 2° latitude, and it consists of 48 vertical levels with the top at 0.01hPa. It has 25 levels in the stratosphere and includes on-line chemistry in

both stratosphere and troposphere. The second set of synthetic AIRS radiance is based on the 6-hourly ERA-interim reanalysis (Dee et al. 2011). The ERA-interim is the latest reanalysis from the ECMWF. Its horizontal resolution is 1.5° latitude by 1.5° longitude. It has 60 vertical layers with 24 layers in the stratosphere. For both cases, the temperature, humidity, ozone, and cloud profiles are interpolated onto the AIRS trajectories and then fed into the radiance simulator to generate the AIRS radiances; then such synthetic AIRS radiances are averaged and processed in the same way as the observed AIRS radiances. The blue and red lines in Fig. 2.2 show the global-mean radiance anomalies from the synthetic AIRS radiances based on GFDL AM3 model simulation and the ERA-Interim reanalysis, respectively.

2.2.3 Trends estimated using the spectral radiative kernel techniques

In order to carry out the "closure" study mentioned in Section 1, we will need to compute the trends of synthetic radiances based on the AIRS L2 retrievals. Given the focus here are the global-mean radiances and their trends; we adopt a spectral radiative kernel approach for this investigation. Specifically, the brightness temperature (BT) of a given channel v at the top of atmosphere (TOA) can be written as the function of atmospheric parameters: $BT_v = f_v$ (Ts, Ta, H_2O, CO_2…) and the deviation of the BT_v from its long-term time-invariant mean state can be expressed as:

$$\Delta BT_v = \frac{\partial f_v}{\partial T_s}\Delta T_s + \sum_i \frac{\partial f_v}{\partial T_a^i}\Delta T_a^i + \sum_i \frac{\partial f_v}{\partial H_2O^i}\Delta H_2O^i + \frac{\partial f_v}{\partial CO_2}\Delta CO_2 + Residual \qquad (2.1)$$

Its time derivative can be written as

$$\Delta_t BT_\nu = \frac{\partial f_\nu}{\partial T_s}\Delta_t T_s + \sum_i \frac{\partial f_\nu}{\partial T_a^i}\Delta_t T_a^i + \sum_i \frac{\partial f_\nu}{\partial H_2O^i}\Delta_t H_2O^i + \frac{\partial f_\nu}{\partial CO_2}\Delta_t CO_2 + Residual \qquad (2.2)$$

Where Δ is the deviation from the mean state (i.e. anomaly) and Δ_t is the first order derivation with respect to time and $\frac{\partial f_\upsilon}{\partial X}$ is the radiative kernel. T_a and T_s denote air temperature and surface temperature, respectively. Superscript *i* refers to the i-th layer in the atmosphere. H_2O and CO_2 refer to the mixing ratios of water vapor and carbon dioxide, respectively. According to equation (2.2), linear trends of temperatures and trace gas mixing ratios can be used to estimate the corresponding trend of BT at an AIRS stratospheric channel as long as the spectral radiative kernel kernels, $\frac{\partial f_\upsilon}{\partial X}$, are available.

We follow the approach in Huang et al. (2014) to construct the spectral radiative kernel. Specifically, the spectral radiative kernels are computed using the PCRTM-based radiance simulator for each ERA-interim grid box, then they are weighted by the cosines of their latitudes and averaged to obtain a set of global-mean radiative kernels. Figure 2.3 shows the global-mean spectral radiative kernels with respect to air temperatures, CO_2 and H_2O mixing ratios at different pressure levels. Fig. 2.3a and 3b clearly show that the AIRS stratospheric channels examined in this study have little sensitivity to temperatures and CO_2 concentrations below 200hPa. Fig. 2.3c reconfirms that stratospheric water vapor variations contribute little to the radiance variations in the stratospheric channels within the CO_2 15 μm band. For 1ppmv variation of H_2O, it can only cause ~1.67×10^{-4} K or less change of brightness temperature in the stratospheric channels examined here, which is only ~1.2% or less of the change caused by 1ppmv variation of CO_2. Moreover,

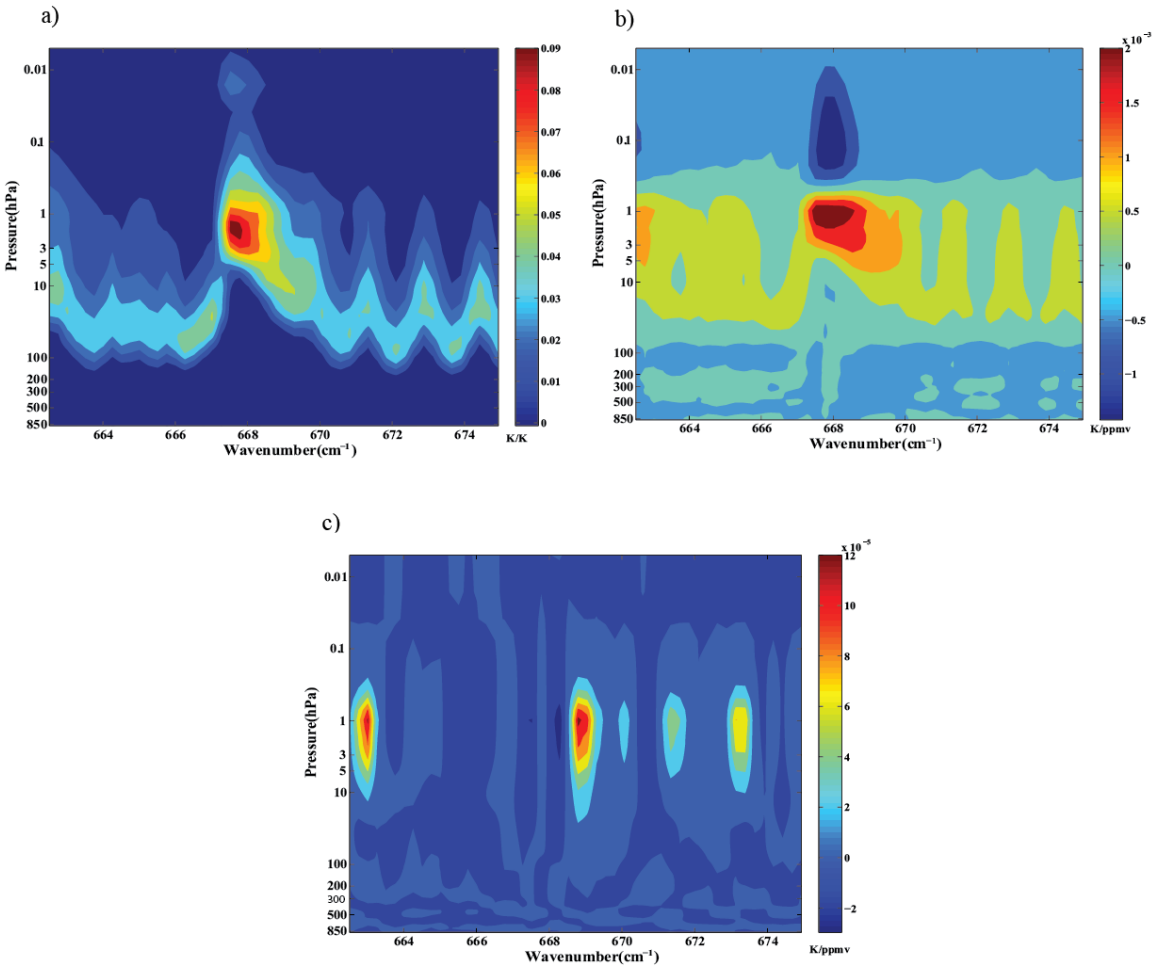

Figure 2.3. (a) Global-mean radiative kernel with respect to the air temperature which is expressed as the change of brightness temperature in K for 1 K change of air temperature. (b) Same as (a) except for CO2 in ppmv. (c) Same as (a) except for H2O in ppmv.

eight years of MLS (microwave limb sounder) measurements (EOS MLS Science Team et al. 2011) indicate that the year-to-year variation of global-mean H_2O mixing ratio between 0.7hPa and 3.3hPa is no more than 0.2ppmv. No statistical significant trends are derivable from the 8 years of MLS data (Nedoluha et al. 2013). Thus, the contribution of water vapor long-term change to the trends of BTs is negligible and we will ignore it in the following discussion.

As for the trends of geophysical parameters in equation (2.2), the temperature trend is derived using AIRS L2 temperature retrievals (Chahine et al. 2006). Similar to the data processing of AIRS radiances, we average the AIRS L2 temperature retrievals onto 2.5° longitude by 2° latitude grid boxes and then get the monthly-mean temperature profiles on the global scale. L2 temperature retrievals have 28 vertical levels between 1100hPa and 0.1hPa with a horizontal resolution of ~45km. Intensive validation of the AIRS retrievals showed that AIRS retrieval achieves about 1K RMS (root mean square) accuracy over ocean and about 1.7K RMS accuracy over land (Fetzer et al. 2003, Chahine et al. 2006). CO_2 is assumed uniformly mixed over the atmosphere and the monthly-mean concentration of CO_2 is based on the measurements from NOAA Earth System Research Laboratory (Tans and Keeling 2011). Based on the assumptions and the measurements, the linear increment trend of well-mixed CO_2 is 1.95ppmv per year throughout the entire atmosphere. With the radiative kernels and linear trends of temperatures and CO_2 mixing ratios derived, we can use equation (2.2) to calculate linear trends of the brightness temperatures to the first-order approximation, and then compare them with those derived directly from the AIRS L1 radiance records. This is the closure study referred in Section 1.

2.3. Results

2.3.1. Linear trend analysis

Linear trend of the time series of brightness temperature of each stratospheric channel is estimated in following ways: first the mean value is subtracted from the time series and then the time series is deseasonalized by removing the mean seasonal cycle. Then the trend is

estimated by linear regression. The uncertainty associated with the trend is estimated with the auto-correlation time scale taken into account (Weatherhead et al. 1998).

Figure 2.4 shows the peaks of weighting functions of the 50 stratospheric channels used in this study, which indicates to which pressure level the radiance in each channel is most sensitive. The peaks are all in the stratosphere between 100hPa and 1hPa.

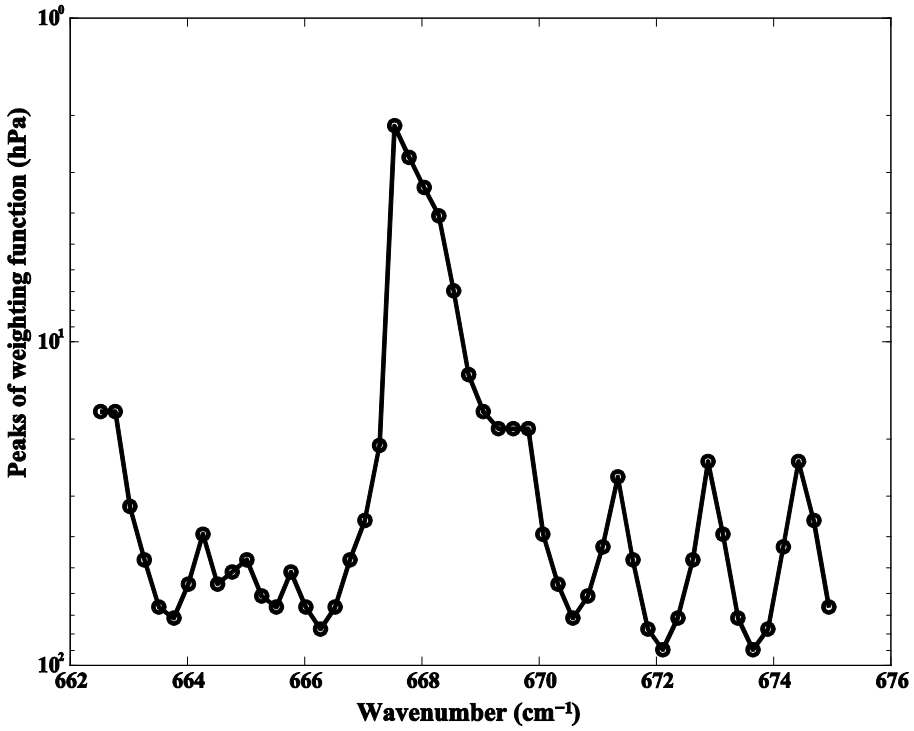

Figure 2.4. Peaks of the weighting functions for the AIRS channels in the CO_2 ν_2 band used in this study. Profiles of 1976 US Standard Atmosphere are used in the calculation of the weighting functions.

Figure 2.5 plots the linear trends of the 50 channels derived from AIRS observations with respect to the peak pressure level of their weighting functions. Note this is for a convenient way of visualizing the results and the ordinate is not pressure coordinate. The counterparts derived from the synthetic AIRS radiances based on the GFDL AM3 simulation and the ERA-interim reanalysis are shown in the same figure as well. The AIRS channels with peaks

above 47hPa all show statistically significant cooling trends. Furthermore, the higher the peak is, the larger the cooling trend generally is. Between 47hPa and 30hPa, BT cooling trend is about 0.1-0.25K/decade. Above 10hPa, the cooling trend is as large as 0.5-0.6K/decade. Below 47hPa, the trend is generally negative at about -0.1K/decade but statistically insignificant. Similar trend tendencies are captured by the free-running GFDL AM3 simulation except that the model overestimates the

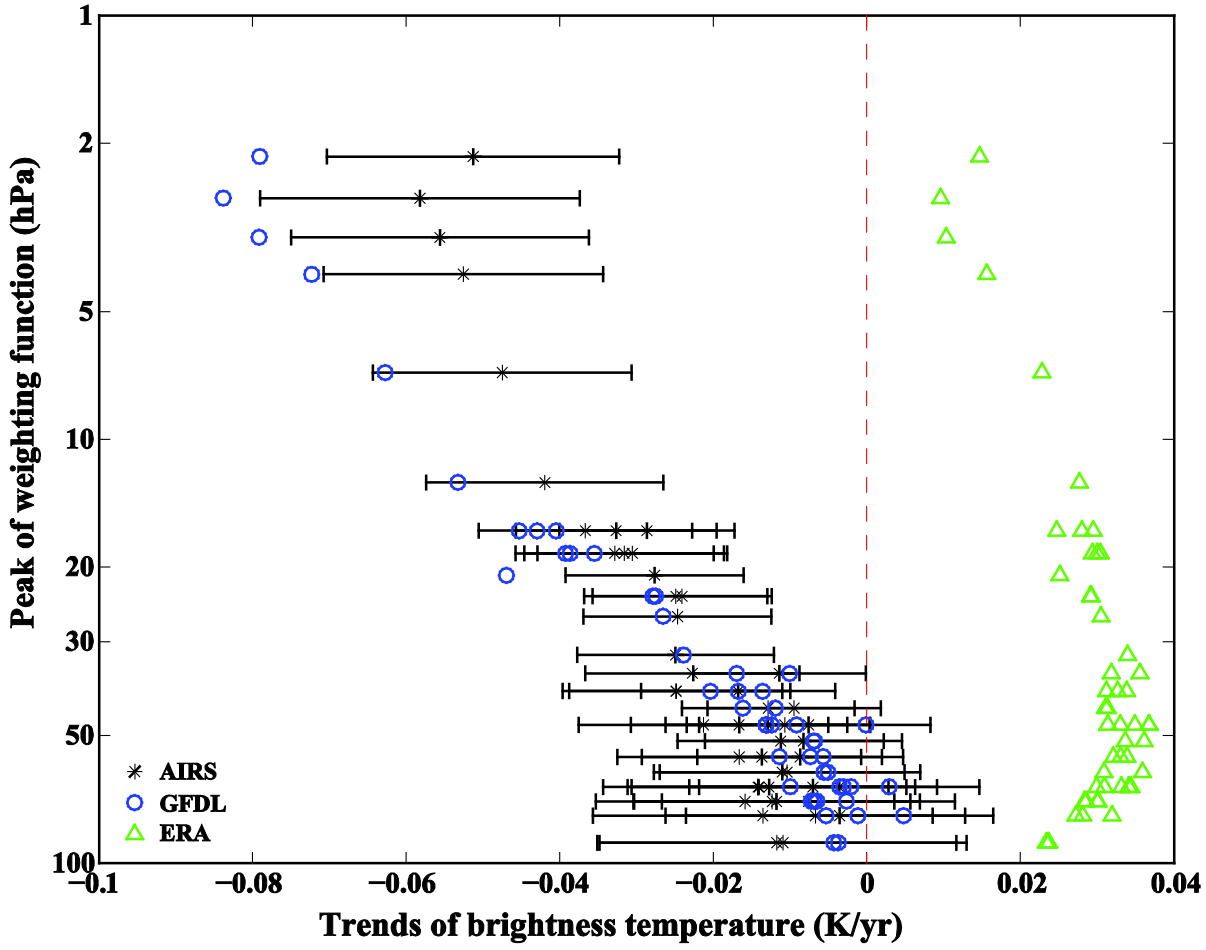

Figure 2.5. Black stars are linear trends of brightness temperatures in the AIRS stratospheric channels plotted with respect to the peaks of the weighting functions of the corresponding channels. Black ticked bars denote 95% confidence levels with the correlation timescale taken into account. Blue circles are the linear trends based on the synthetic AIRS radiances computed using the GFDL AM3 simulation output. Green circles are results using the ERA-interim reanalysis. Please note the ordinate is for the peaks of the weighting function, instead of the conventional pressure coordinate.

cooling trends above 15hPa. In contrast, results based on the ERA-interim reanalysis show statistically significant positive trends in virtually all the stratospheric channels. This could be related to the time-dependent warm biases in the ERA-interim reanalysis (Dee et al. 2011). Since it is not expected for the meteorological reanalysis to have accurate representation of the secular trend in the stratosphere, we do not investigate the cause of the positive trends of ERA-interim further.

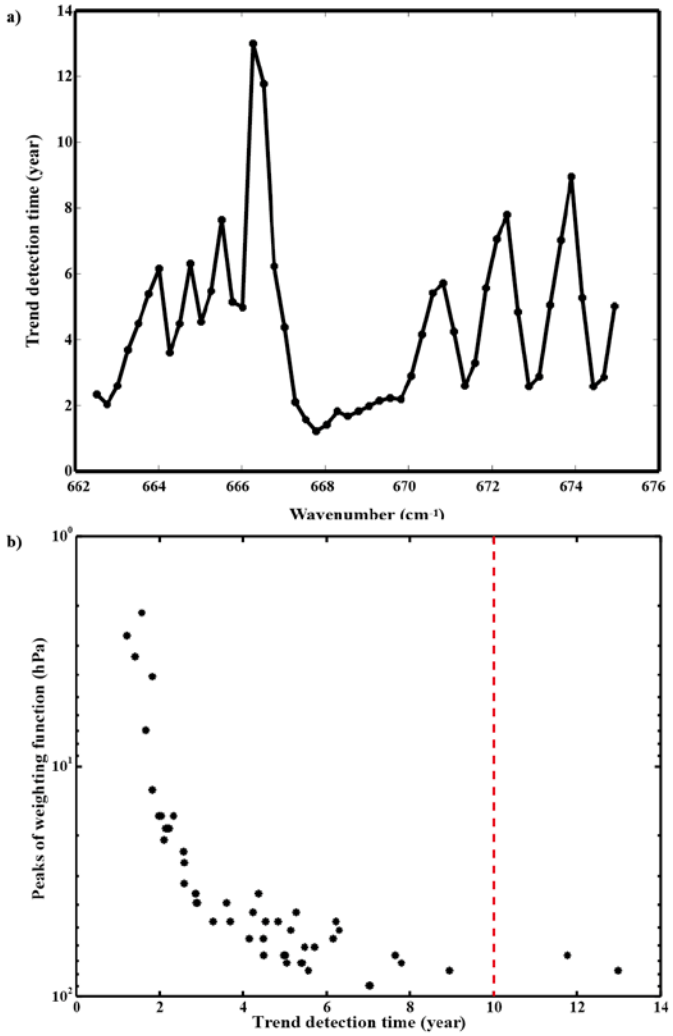

Figure 2.6. (a) Time for trend detection in the presence of natural variability for each AIRS stratospheric channel examined here. The natural variability is derived from 500 years of the GFDL AM3 runs and the signal-to-noise ratio is set to 5. (b) Same as (a) except that the time for trend detection is plotted with respect to the peak of the weighting function of each the AIRS stratospheric channel.

Given the presence of natural variability, one inevitable question to explore is: how long it would take for a trend signal to emerge in the presence of natural variability. We estimate the minimum time for detecting secular trend out of the BT time series of the 50 AIRS stratospheric channels using a formula proposed by Leroy et al. (2008):

$$n = \left[\frac{12 s^2}{m_{est}^2} \sigma_{\mathrm{var}}^2 \tau_{\mathrm{var}} \right]^{1/3} \left(1 + f^2\right)^{1/3} \qquad (2.3),$$

where n is the time needed to detect a trend signal; m_{est} is the trend to be detected and s is the signal-to-noise ratio ($m_{est}/\delta m_{est}$); τ_{var} is the correlation time of natural variability σ_{var} that is defined as the standard deviation of the data set; f is the measurement uncertainty and is set to zero in our estimation. Given the AIRS radiometric uncertainty is ~0.3K for a 250K BT target, f is about 0.0012, which justifies our choice of simply ignoring it. The natural variability is obtained from the simulated synthetic AIRS radiance based on the output from a 500-year control run by the GFDL most recent coupled-GCM, the CM3 (Donner et al. 2011). Using above information, we compute n for each channel and the results are shown in Fig. 2.6. The estimated time for trend detection is less than 10 years for all the channels except 666.27cm^{-1} (weighting function peaks at 77.24hPa) and 666.52cm^{-1} (weighting function peaks at 66.13hPa). Though such estimate is based on modeled natural variability and correlation timescale from one particular GCM simulation, Fig. 2.6a and 6b suggest that statistical significant trends can be derived within a 10-year timeframe for most channels examined here. This is consistent with what is shown in Fig. 2.5.

2.3.2. Closure Study Using Radiative Kernel Technique

As described in Subsection 2.2.3, we use the linear trends of air temperature and CO_2 at all pressure levels together with pre-computed spectral radiative kernels to compute the trend in each AIRS stratospheric channel (black line in Fig. 2.7), as well as the contribution of air temperature and CO_2 to such trend, respectively (blue and green

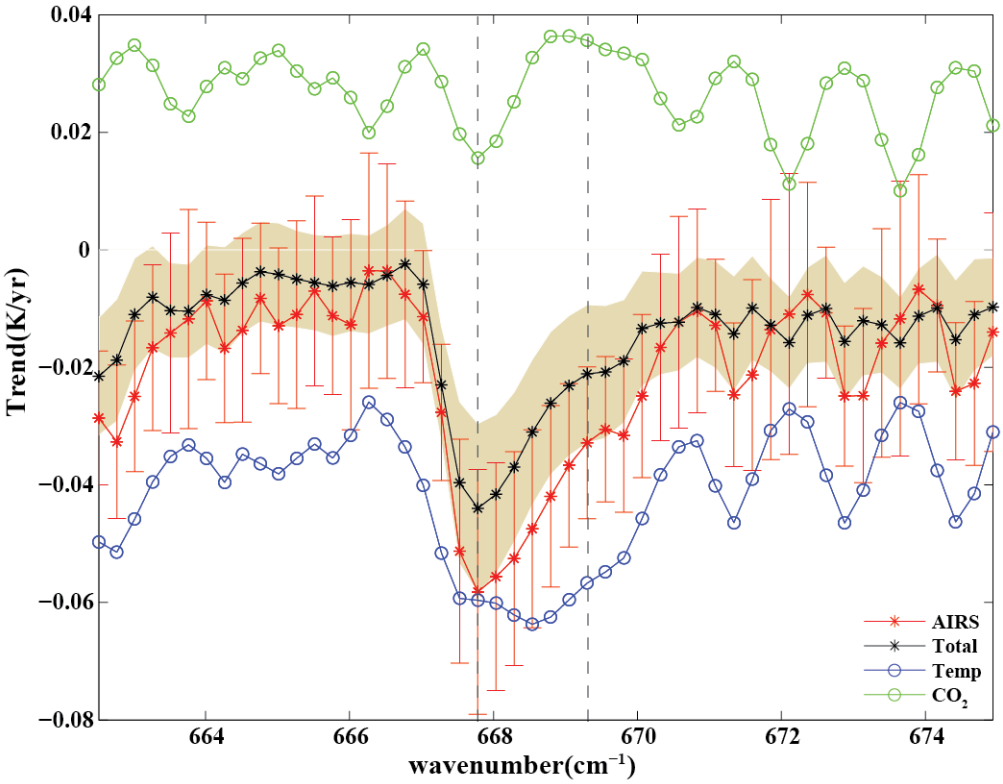

Figure 2.7. The BT linear trends derived from AIRS radiance time series are shown as red stars with 95% confidence interval (vertical ticked red line). The BT linear trends estimated using the global-mean spectral radiative kernels and linear trends of surface CO_2 observations and AIRS L2 retrieved temperatures are shown as black stars with 95% confidence interval (yellow shades). The individual contributions of air temperature (blue circles) and CO_2 (green circles) to the estimated BT trends are shown as well. Two vertical black dash lines denote the spectral region where the observed and estimated BT trends differ the most.

lines in Fig. 2.7). The trends from actual AIRS radiance time series are plotted in red. The estimated trend using air temperature and CO_2 linear trends falls within 95% confidence interval of the actual AIRS trends for all the stratospheric channels examined here. The good

agreement suggests that the AIRS L2 retrievals and surface observations of CO_2 mixing ratio can largely reproduce the BT trends derived from the AIRS L1b radiance time series. The largest discrepancies between actual and computed trends are seen between ~668-670cm^{-1}, i.e. on the R branch of the CO_2 ν_2 band, where observed BT trends are out of the 95% confidence intervals of the estimated trends using Equation (2.2). A couple of possible reasons for the discrepancies in this spectral range are:

(1) The linear approximation employed in Equation (2.2) is not enough to explain the actual trends. The nonlinear terms should be taken into account.

(2) The uncertainty associated with the spectral radiative kernel used in Fig. 2.7.

As for (1), the previous study by Chen et al. (2013) has shown that, at least for the globally average radiances, the linear approximation is a valid approximation for the frequencies examined in this study. As for (3), we use following method to quantify the uncertainties associated with construction of the spectral radiative kernel. We re-compute the linear trend in BT using the zonal-mean spectral radiative kernels of an individual month instead of annual and global-mean spectral radiative kernels. Specifically, the zonal-mean spectral radiative kernels and zonal-mean temperature anomalies are used to estimate the zonal trend of BT for every 2 latitude bin, then such zonal-mean BT trend is weighted by the area and averaged to obtain the global-mean BT trend. We construct such zonal-mean kernels based on 12 months of ERA-interim reanalysis and 12 months of free-running GFDL CM3 simulations, respectively. By doing so, we have 24 estimates of the BT trends in total, which are then used as a measure of uncertainty associated with the construction of the kernels. The

results are shown in Fig. 2.8. Note the spreads in Fig. 2.8 are solely due to different kernels used in the estimates; the uncertainty of the trends in the AIRS L2 temperature retrievals (the orange shades on Fig. 2.7) is not included here. It can be seen that the uncertainty due to different ways of constructing spectral radiative kernels has little impact on the final results and cannot be a major reason for the discrepancies between the observed and estimated BT trends in the stratosphere channels shown in Fig. 2.7.

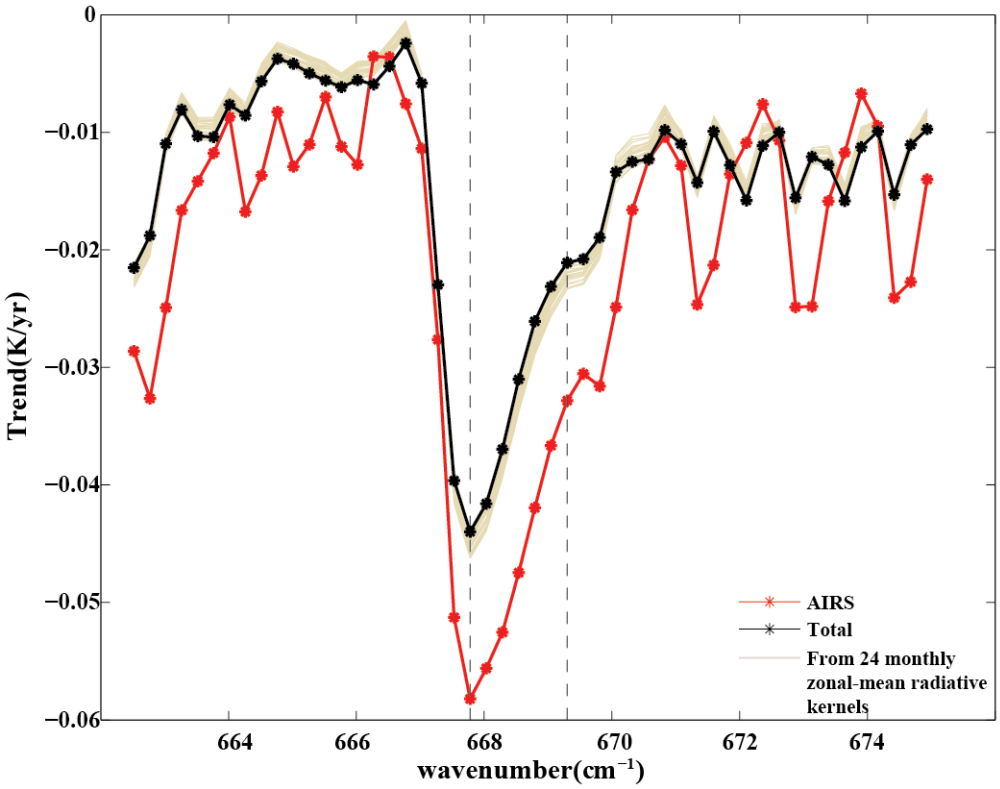

Figure 2.8. The BT trends from actual AIRS radiance time series (red) and the BT trends estimated using global-mean spectral radiative kernel in equation (2.2) (black). Gray lines are the global BT trends estimated using 24 different sets of zonal- and monthly-mean spectral radiative kernels for every 2° latitude bin. 12 sets are from the GFDL CM3 simulations and the rest from the ERA-interim reanalysis. Between the dash lines is the spectral region we are interested in.

Though there are discrepancies in some spectral regions, Fig. 2.7 and Fig. 2.8 show large consistency between the observed trends based on the AIRS L1b radiances, and the

counterparts based on the AIRS L2 retrievals and spectral radiative kernels. As far as the global average is concerned, they show that the secular trends of AIRS L1b radiances and L2 temperature retrievals are consistent with each other.

2.4. Conclusion and Discussion

Motivated by the excellent performance of AIRS instrument, we compile 10-year (2003-2012) AIRS L1b radiances and estimate the linear trends of global-mean radiances at 50 stratospheric channels in the CO_2 ν_2 band. For comparison, two set of synthetic AIRS radiances at these channels are simulated using two different inputs: simulation from a free-running GFDL AM3 model and the ECMWF ERA-interim reanalysis. While the results based on the GFDL AM3 model can agree with the observed trends to some extent, the trends based on the ERA-interim have opposite signs compared to the observed ones. This reaffirms that cautions must be taken in the use of reanalysis stratospheric data in the study of trends and variability over multiple years.

Employing a radiative kernel technique, we show that the secular linear trends of the AIRS L1b radiances in these channels can be largely reproduced using AIRS L2 retrievals and surface observations of CO_2 mixing ratios. Though there are discrepancies around ~668-670cm^{-1} between the L1b trends and the trends based on the L2 retrievals, the general agreements are satisfactory. The discrepancies around ~668-670cm^{-1} could be due to other reasons, e.g. undetected spectral shift over such long period or the breakdown of linearity assumption needed for the radiative kernel analysis.

This study is focused on the conventional linear trend analysis from the actual AIRS radiances. As shown in Fig. 2. 6, the detection of trends in the presence of natural variability can be achieved at many channels using 10 year or less of data. This suggests that formal detection and attribution studies might be possible using the 10+ years of the AIRS L1 radiances, such as the optimal spectral fingerprinting technique in Leroy et al. (2008). Observationally, careful examinations are warranted to ensure the long-term performance of the AIRS instruments, especially for the possible drift of radiometric or spectral calibrations. On the other side, spectral fingerprints need to be constructed correctly in such detection and attribution studies. One particular challenge would be how to take the actual solar variation into account, as the 11-year solar cycle can likely affect the stratospheric temperatures (Coughlin and Tung 2004). These would be the focuses of our follow-up studies.

2.5 Acknowledgements

The AIRS Level-1b data are obtained from NSA GSFC DAAC and the AIRS L2 data from http://disc.sci.gsfc.nasa.gov/AIRS/data-holdings/by-data-product-V6. The ECMWF ERA-Interim data are from http://apps.ecmwf.int/datasets/data/interim-full-daily/. We thank Dr. X.H. Chen for her help in the early stage of this study. This research is supported by NASA grants NNX11AE68G and NNX15AC25G awarded to the University of Michigan.

Reference:

1. Aumann, H. H., M. T. Chahine, C. Gautier, M. D. Goldberg, E. Kalnay, L. M. McMillin and J. Susskind, 2003: AIRS/AMSU/HSB on the Aqua mission: Design, science objectives, data products, and processing systems. *IEEE Trans. Geosci. Remote Sens.*, **41**(2), 253–264, doi: 10.1109/TGRS.2002.808356.

2. Aumann, H. H., S. Broberg, D. Elliott, S. Gaiser, and D. Gregorich, 2006: Three years of AIRS radiometric calibration validation using sea surface temperatures, *J. Geophys. Res.*, **111**, D16S90, doi: 10.1029/2005JD006822.

3. Aumann, H. H., and T. S. Pagano, 2008: Using AIRS and IASI data to evaluate absolute radiometric accuracy and stability for climate applications. *Proc. SPIE Int. Soc. Opt. Eng.*, **7085**, doi: 10.1117/12.795225.

4. Chahine, M. T., and Coauthors, 2006: The atmospheric infrared sounder (AIRS): Improving weather forecasting and providing new data on greenhouse gases. *Bull. Am. Meteorol. Soc.*, **87**(7), 911–926.

5. Chen, X. H., X. L. Huang, N. G. Loeb, and H. L. Wei, 2013: Comparisons of clear-sky outgoing far-IR flux inferred from satellite observations and computed from the three most recent reanalysis products. *J. Climate*, **26**, 478–494, doi: 10.1175/JCLI-D-12-00212.1.

6. Coughlin, K., and K. K. Tung, 2004: Eleven-year solar cycle signal throughout the lower atmosphere. *J. Geophys. Res*, **109**, D21105, doi: 10.1029/2004JD004873.

7. Dee, D. P., and Coauthors, 2011: The ERA-Interim reanalysis: configuration and performance of the data assimilation system. *Quart. J. Roy. Meteor. Soc.*, **137**, 553-597, doi: 10.1002/qj.828.

8. Donner, L. J., and Coauthors, 2011: The dynamical core, physical parameterizations, and basic simulation characteristics of the atmospheric component AM3 of the GFDL global coupled model CM3. *J. Clim.*, **24**, 3484-3519, doi: 10.1175/2011JCLI3955.1.

9. EOS MLS Science Team, 2011: *MLS/Aura Level 2 Water Vapor (H2O) Mixing Ratio, version 003*, Greenbelt, MD, USA: NASA Goddard Earth Science Data and Information Services Center.

10. Fetzer, E., and Coauthors, 2003: AIRS/AMSU/HSB validation. *IEEE Trans. Geosci. Remote Sens.*, **41**(2), 418–431, doi: 10.1109/TGRS.2002.808293.

11. Forster, P. M., and Coauthors, 2011: Evaluation of radiation scheme performance within chemistry climate models. *J. Geophys. Res*, **116**, D10302, doi: 10.1029/2010JD015361.

12. Gaiser, S. L., H. H. Aumann, D. T. Gregorich, and T. J. Hearty, 2003: In-flight refinement of the radiometric, spectral, and spatial calibration of the atmospheric infrared sounder (AIRS). In *Optical Science and Technology, SPIE's 48th Annual Meeting*. International Society for Optics and Photonics, 232-243, doi: 10.1117/12.506380.

13. Huang, X., and Y. L. Yung, 2005: Spatial and spectral variability of the outgoing thermal IR spectra from AIRS: A case study of July 2003. *J. Geophysical Res.*, **110**, D12102, doi: 10.1029/2004JD005530.

14. Huang, X., X. Chen, B. J. Soden, and X. Liu, 2014: The spectral dimension of longwave feedback in the CMIP3 and CMIP5 experiments. *Geophysical Research Letters*, **41(22)**, 7830-7837, doi: 10.1002/2014GL061938.

15. Leroy, S., J. Anderson, J. Dykema, and R. Goody, 2008: Testing climate models using thermal infrared spectra. *J. Climate*, **21**, 1863-1875, doi: /10.1175/2007JCLI2061.1.

16. Leroy, S. S., J. G. Anderson, and G. Ohring, 2008: Climate signal detection times and constraints on climate benchmark accuracy requirements. *J. Climate*, **21**, 841-846, doi: 10.1175/2007JCLI1946.1.

17. Liu, X., W. L. Smith, D. K. Zhou, and A. Larar, 2006: Principal component-based radiative transfer model for hyperspectral sensors: theoretical concept. *Applied optics*, **45(1)**, 201-209, doi: 10.1364/AO.45.000201.

18. Mears, C. A., and F. J. Wentz, 2009: Construction of the Remote Sensing Systems V3.2 Atmospheric Temperature Records from the MSU and AMSU Microwave Sounders. *J. Atmos. Oceanic Technol.*, **26**, 1040–1056, doi: 10.1175/2008JTECHA1176.1.

19. Mears, C. A., F. J. Wentz, P. Thorne, and D. Bernie, 2011, Assessing uncertainty in estimates of atmospheric temperature changes from MSU and AMSU using a Monte-Carlo estimation technique, *J. Geophys. Res.*, **116**, D08112, doi: 10.1029/2010JD014954.

20. Nedoluha, G. E., R. Michael Gomez, D. R. Allen, A. Lambert, C. Boone, and G. Stiller, 2013, Variations in middle atmospheric water vapor from 2004 to 2013, *J. Geophys. Res. Atmos.*, **118**, 11,285–11,293, doi:10.1002/jgrd.50834.

21. Pagano, T. S., H. H. Aumann, D. E. Hagan, and K. Overoye, 2003: Prelaunch and in-flight radiometric calibration of the Atmospheric Infrared Sounder (AIRS). *Geoscience and Remote Sensing, IEEE Transactions on*, **41(2)**, 265-273, doi: 10.1109/TGRS.2002.808324.

22. Ramaswamy, V., and Coauthors, 2001: Stratospheric temperature trends: Observations and model simulations. *Rev. Geophys.*, **39**, 71-122, doi: 10.1029/1999RG000065.

23. Ramaswamy, V., M. D. Schwarzkopf, W. J. Randel, B. D. Santer, B. J. Soden, and G. L. Stenchikov, 2006: Anthropogenic and natural influences in the evolution of lower stratospheric cooling. *Science*, **311**, 1138-1141. doi: 10.1126/science.1122587.

24. Seidel, D. J., N. P. Gillett, J. R. Lanzante, K. P. Shine, and P. W. Thorne, 2011: Stratospheric temperature trends: Our evolving understanding. *Wiley Interdiscip. Rev. Clim. Change*, **2**, 592-616, doi: 10.1002/wcc.125.

25. Shine, K. P., and Coauthors, 2003: A comparison of model-simulated trends in stratospheric temperatures. *Q. J. R. Meteorol. Soc.*, **129**, 1565–1588, doi: 10.1256/qj.02.186.

26. Tans, P., and R. Keeling, 2011: Trends in atmospheric carbon dioxide. *NOAA Earth Systems Research Laboratory.*

27. Thompson, D. W., and Coauthors, 2012: The mystery of recent stratospheric temperature trends. *Nature*, **491**(7426), 692-697, doi: 10.1038/nature11579.

28. Thorne, P. W., and R. S. Vose, 2010: Reanalyses suitable for characterizing long-term trends: Are they really achievable? *Bull. Amer. Meteor. Soc.*, **91**, 353-361, doi: 10.1175/2009BAMS2858.1.

29. Weatherhead, E. C., and Coauthors, 1998: Factors affecting the detection of trends: Statistical considerations and applications to environmental data. *J. Geophys. Res.*, **103**, 17149-17161, doi: 10.1029/98JD00995.

30. Zou, C. Z., M. D. Goldberg, Z. Cheng, N. C. Grody, J. T. Sullivan, C. Cao, and D. Tarpley, 2006: Recalibration of microwave sounding unit for climate studies using simultaneous nadir overpasses. *J. Geophys. Res.*, **111**, D19114, doi: 10.1029/2005JD006798.

31. Zou, C. Z., and W. Wang, 2009: Diurnal drift correction in the NESDIS/STARMSU/AMSU atmospheric temperature climate data record. *Atmospheric and Environmental Remote Sensing Data Processing and Utilization V: Readiness for FEOSS III*, C.-Z.Zou and W. Wang, Eds., Internaltional Soceity for Optical Engineering (SPIE Proceedings, Vol. 7456), 74560G, doi: 10.1117/12.824459.

32. Zou, C. Z., and W. Wang, 2010: Stability of the MSU-derived atmospheric temperature trend. *J. Atmos. Oceanic Technol.*, **27**, 1960-1971, doi: 10.1175/2009JTECHA1333.1.

33. Zou, C. Z., and W. Wang, 2011: Intersatellite calibration of AMSU-A observations for weather and climate applications. *J. Geophys. Res.*, **116**, D19114, doi: 10.1029/2011JD016205.

Chapter 3

The stratospheric changes inferred from 10 years of AIRS and AMSU-A radiances

The material of this chapter was published in

Pan, F, X. Huang, S.S. Leroy, P. Lin, L. L. Strow, Y. Ming, V. Ramaswamy, 2017. The stratospheric changes inferred from 10 years of AIRS and AMSU-A radiances. *J. Clim., in press.*

3.1 Introduction

An important topic in the study of climate changes is how the stratospheric temperatures respond to external forcings such as the increases of greenhouse gases, volcano eruptions, secular changes of ozone concentration, and solar cycles (Ramaswamy et al., 2006; Randel et al., 2009 and Seidel et al., 2011). The long-term satellite data used in the study of stratospheric responses to external forcing are usually from the Microwave Sounding Units (MSU) and the Stratospheric Sounding Units (SSU) (Ramaswamy et al., 2001; Randel et al., 2009, 2016; Seidel et al., 2011 and 2016; Thompson et al., 2012; Zou et al., 2014; Zou &

Qian, 2016). A large amount of efforts has been invested in merging multi-decadal time-series for climate trend analysis and making these data sets into climate-quality data record (Christy et al., 2003; Mears & Wentz, 2009; Zou & Wang, 2010; Zou et al., 2014,). Succeeding to MSU and SSU, the AMSU-A aboard several NOAA polar-orbiting satellites since 1998 measures microwave radiances at 15 discreet frequency channels between 23-90 GHz (Mears & Wentz, 2009; Goodrum et al., 2010, Wang & Zou, 2014). Its measurement capability surpasses MSU with six channels sensitive to temperatures in the stratosphere. Although originally designed for weather observation, after homogenizing the data from different satellites the merged and recalibrated AMSU-A radiances can also play a vital role in stratospheric climate study. Another potential valuable data set for stratospheric trend study is AIRS (Atmospheric Infrared Sounder) aboard the NASA Aqua satellite. The AIRS instrument has demonstrated stable and accurate performance (Chahine et al., 2006) since its launch in September 2002. Using 10 years of measurements, statistically significant trends already can be seen from the radiances of AIRS channels sensitive to emission and absorption in the stratosphere (hereafter referred as stratospheric channels, in the CO_2 ν_2 band, Pan et al., 2015). The AIRS radiances of the stratospheric channels, in principle, have considerable information content on vertical temperature profiles because (1) in our study AIRS has 50 channels sensitive to emissions and absorptions in the stratosphere (Fang et al., 2015) and (2) the AIRS stratospheric channels usually have narrower weighting functions than the AMSU-A microwave channels, a common feature in the contrast of IR and microwave soundings. However, all the AIRS stratospheric channels are also sensitive to CO_2 emission and absorption, which makes separation of secular changes of CO_2 and stratospheric temperatures

from such AIRS stratospheric channels a challenging task. The AMSU-A radiances are sensitive to oxygen emission and absorption but not sensitive to CO_2 emission and absorption at all. Thus a synergistic use of AIRS and AMSU observations, in principle, can help better understand the global stratospheric temperature change at a higher vertical resolution than previous studies that employed MSU or SSU measurements. Such synergistic use of AIRS and AMSU can also make it possible to infer CO_2 change in the stratosphere.

Optimal fingerprinting extracts maximum information from data on climate trends in the atmosphere against a background of natural variability. As a detection and attribution technique for climate change studies, optimal fingerprinting was pioneered by Bell (1986), Hasselmann (1993; 1997) and North et al. (1995) and has been applied onto a variety of observational data sets, such as tropopause height (Santer et al., 2003), tropospheric water vapor (Santer et al., 2007) and hydrological cycle in the western United States (Barnett et al., 2008). It has also been applied to synthetic infrared radiances based on climate model simulations (Leroy et al., 2008; Huang et al., 2010a and 2010b) but never applied to observed infrared radiances. In this chapter, we apply optimal detection directly to globally averaged AIRS infrared radiances and AMSU-A microwave radiances measured from 2003 to 2012 to detect the secular trend in the stratospheric temperature with the natural variability taken into account. The rest of this chapter is arranged as follows. Section 3.2 describes the decadal radiance changes in the stratospheric channels observed by AIRS and AMSU-A. The optimal fingerprinting methods and details about how to apply this technique are also explained in the Section 3.2. The detection results of stratospheric changes are shown and discussed in the Section 3.3. Section 3.4 presents conclusions and further discussions.

3.2 Data and Methods

3.2.1 Observed trends of brightness temperatures on the AIRS and AMSU-A stratospheric channels

Procedures to obtain globally averaged radiances from AIRS L1B dataset and then to estimate the trends Δd for AIRS radiances on 50 stratospheric channels between 662.5 and 674.9 cm^{-1} have been explained in Pan et al. (2015). They found a trend of no more than -0.23 K $decade^{-1}$ for brightness temperatures of the AIRS lower stratospheric channels while a statistically significant trend as large as -0.58 K $decade^{-1}$ in the AIRS middle-stratospheric channels. In this chapter, we further improves the estimates of the brightness temperature trends on the AIRS stratospheric channels by taking the secular shift of the center frequency shift of AIRS into account (Strow et al., 2006). While AIRS frequency can be extremely stable and shift below 0.1% of a full width half max for demanding applications like climate monitoring, the brightness temperature trends caused by frequency shift could be non-negligible and need to be removed (Gaiser et al., 2003; Strow et al., 2006). AIRS spectral response functions (SRFs) on each channel are measured during prelaunch testing and available from http:/asl.umbc.edu/pub/airs/srf. Here we assume the SRF shape fixed and only consider the contribution of SRF center frequency shift to brightness temperature bias ΔBT_shift(t, ν) over 2003-2012. Firstly the monthly climatology of radiances with a spectral resolution of 0.001cm^{-1} covering AIRS CO_2 ν2 band were simulated by line-by-line radiative transfer model (LBLRTM) (Clough et al., 2005), into which monthly atmospheric profiles with the horizontal resolution of 1.5°x1.5° in 2008 from ERA-interim reanalysis (Dee et al.,

2011) are taken as input. After this, the monthly climatology of radiances were multiplied by AIRS SRF on each

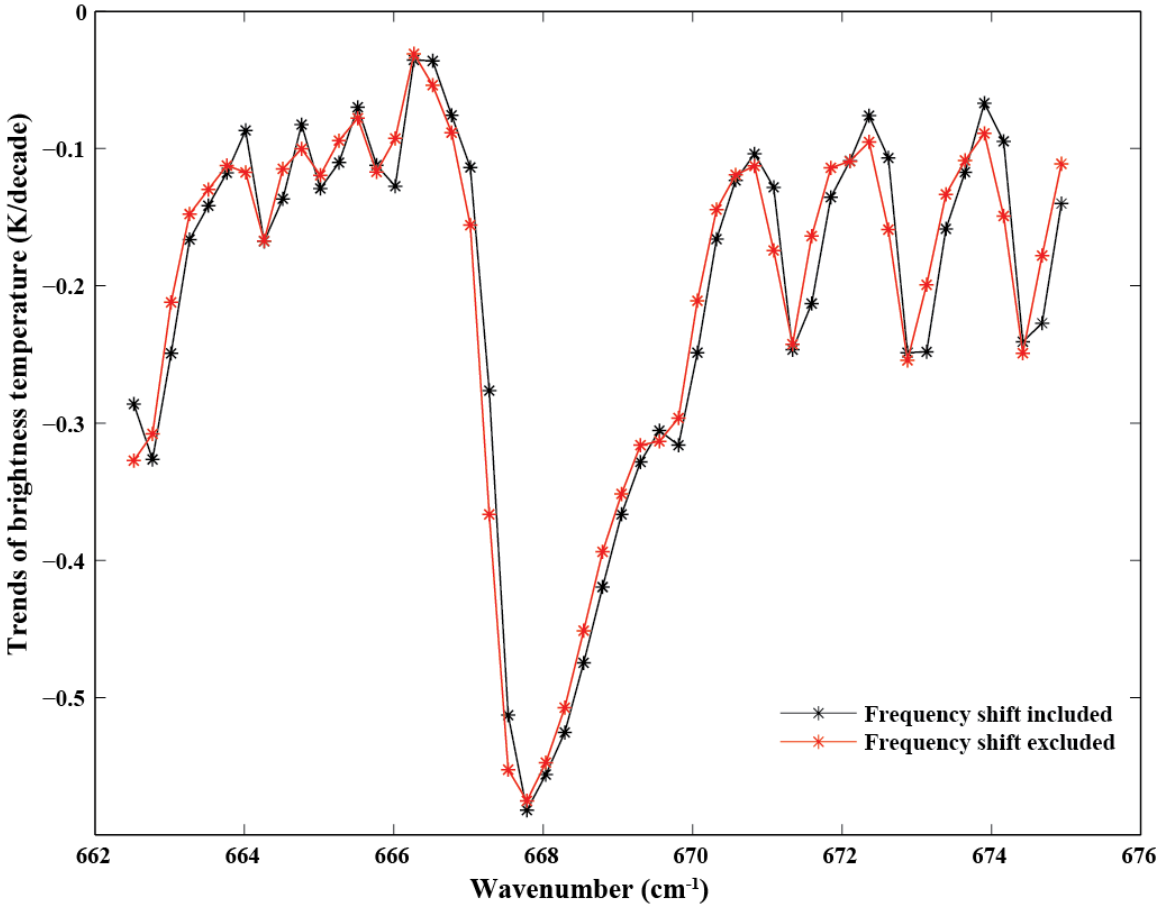

Figure 3.1. The linear trends on 50 AIRS stratospheric channels when the biases due to channel center frequency shift are removed (red line) and not removed (black line).

grid box and averaged into global-mean spectra BT(t, ν) on 50 AIRS stratospheric channels. Then we generate the spectra BT_ shift(t, ν) considering the center frequency shift. The shift of the center frequency of each AIRS channel from 2003 to 2012 was determined using the method depicted in Strow et al. (2006). We add these frequency shifts onto SRFs and obtain time-varying AIRS SRFs. Again, we multiply the monthly climatology of radiances by the new AIRS SRFs to generate the BT_ shift(t, ν). The differences between BT_ shift(t,ν) and

BT(t,ν) are just the brightness temperature biases ΔBT_ shift(t, ν) due to the drift of the center frequency. Finally, we calculate the linear trends Δd_ shift from ΔBT_ shift(t, ν) and remove it from our previous estimate in Pan et al. (2015) to get new Δd to be used in optimal fingerprinting. Both previous and this new estimate of Δd on AIRS stratospheric channels are presented in Fig. 3.1.

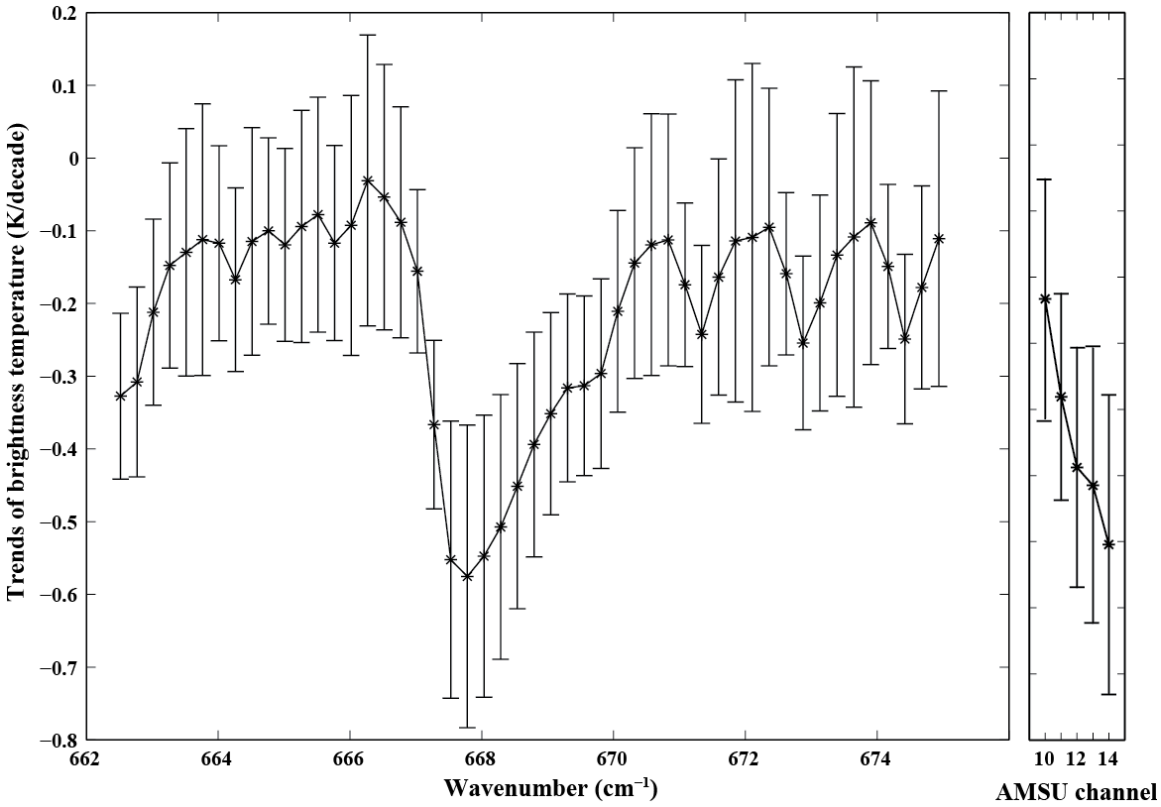

Figure 3.2. 10-year linear trend of global-mean brightness temperature of the AIRS and AMSU-A stratospheric channels. Five AMSU-A channels are labeled with their channel numbers instead of actual frequencies. The error bar denotes 95% confidence interval.

The globally averaged brightness temperatures for the AMSU-A channels 10-14 are directly obtained from the RSS (Remote Sensing System) version 3.3 long-term inter-satellite merging and inter-calibrated radiance product (Mears et al., 2009, 2011). The RSS team showed improved agreement of time series on short time scales and long-term trends between

the radiosonde data and this satellite data. The same method as in Pan et al. (2015) has been used to compute the linear trend of the AMSU-A radiances. Figure 3.2 summarizes the linear trends of global average brightness temperature of the AIRS and AMSU-A stratospheric channels.

Deriving actual stratospheric temperature changes from the radiance trends above in the presence of natural variability is our focus in this study. In our application of optimal fingerprinting, we model the data as linear trends in independent stratospheric layers:

$$\Delta d = \sum_i S_i \Delta\alpha_i + \delta\varepsilon \qquad (3.1)$$

Where Δd just represents the observed trends of brightness temperatures of the 50 AIRS stratospheric channels and of five AMSU-A channels (channel No. 10-14) over 2003-2012, and $\Delta\alpha_i$ is stratospheric change we want: the CO_2 change or temperature change in the *i*'th atmospheric layer as defined below. Spectral fingerprint $\mathbf{S_i}$ is the spectral change associated with unit temperature change in the *i*'th stratospheric layer or unit CO_2 change. The residual term $\delta\varepsilon$ explains all departures of the data from the model, including naturally occurring internal variability, radiance leakage from the troposphere, unaccounted composition change, and unresolved vertical structure. How to derive the $\Delta\alpha_i$ is explained in Section 2.2.

3.2.2 Optimal fingerprinting technique

3.2.2.1 Introduction

The description below largely follows the depiction in Leroy et al. (2006; 2010). Assuming the natural variability observing Gaussian distribution and using the same notation

as Equation (3.1) in the text, the magnitude $\Delta\boldsymbol{\alpha}$ associated with fingerprint **S** can be estimated using the observed climate change $\Delta\mathbf{d}$ in the presence of natural variability $\boldsymbol{\delta\varepsilon}$ as:

$$\Delta\alpha = \mathbf{F}^T \Delta d \qquad (3.2)$$

where

$$\mathbf{F} = \boldsymbol{\Sigma}^{-1}\mathbf{S}(\mathbf{S}^T\boldsymbol{\Sigma}^{-1}\mathbf{S})^{-1} \qquad (3.3)$$

$$\boldsymbol{\Sigma} = \boldsymbol{\Sigma}_{\boldsymbol{n}} + \boldsymbol{\Sigma}_{\boldsymbol{s}} \qquad (3.4)$$

$$\boldsymbol{\Sigma}_{\boldsymbol{n}} = (\delta\varepsilon)(\delta\varepsilon)^T \qquad (3.5)$$

$$\boldsymbol{\Sigma}_{\boldsymbol{s}} = (\delta\boldsymbol{S}\Delta\alpha)(\delta\boldsymbol{S}\Delta\alpha)^T \qquad (3.6)$$

In equation (3.6), $\delta\mathbf{S}$ refers to the uncertainty associated with the fingerprint **S**. Note $\Delta\boldsymbol{\alpha}$ indeed appears in both sides of equation (3.2), which weights the influences between the natural noise $\boldsymbol{\delta\varepsilon}$ and the uncertainty of spectral fingerprint $\delta\mathbf{S}$. In practice, $\Delta\boldsymbol{\alpha}$ is solved iteratively: the first guess of $\Delta\boldsymbol{\alpha}$ is obtained by assuming $\boldsymbol{\Sigma}_s$=0 and then equations (3.2)-(3.6) are solved by iteration until the solution to equation (3.2), $\Delta\boldsymbol{\alpha}$**,** is converged. The 1-σ uncertainty matrix associated with detected magnitude of change $\Delta\boldsymbol{\alpha}$ is

$$\boldsymbol{\sigma} = (\mathbf{S}^T\boldsymbol{\Sigma}^{-1}\mathbf{S})^{-1} \qquad (3.7)$$

3.2.2.2 Construction of spectral fingerprints

Eight spectral fingerprints (S_i in Equation 3.1) are defined in our study, each corresponding to a $\Delta\alpha_i$: one for the uniform change of CO_2 in the atmosphere, and the remaining for temperature changes in seven vertical layers from 300hPa to 0.009hPa (Fig. 3.3). Five of the seven layers are in the stratosphere with pressure centered at 2.7hPa,

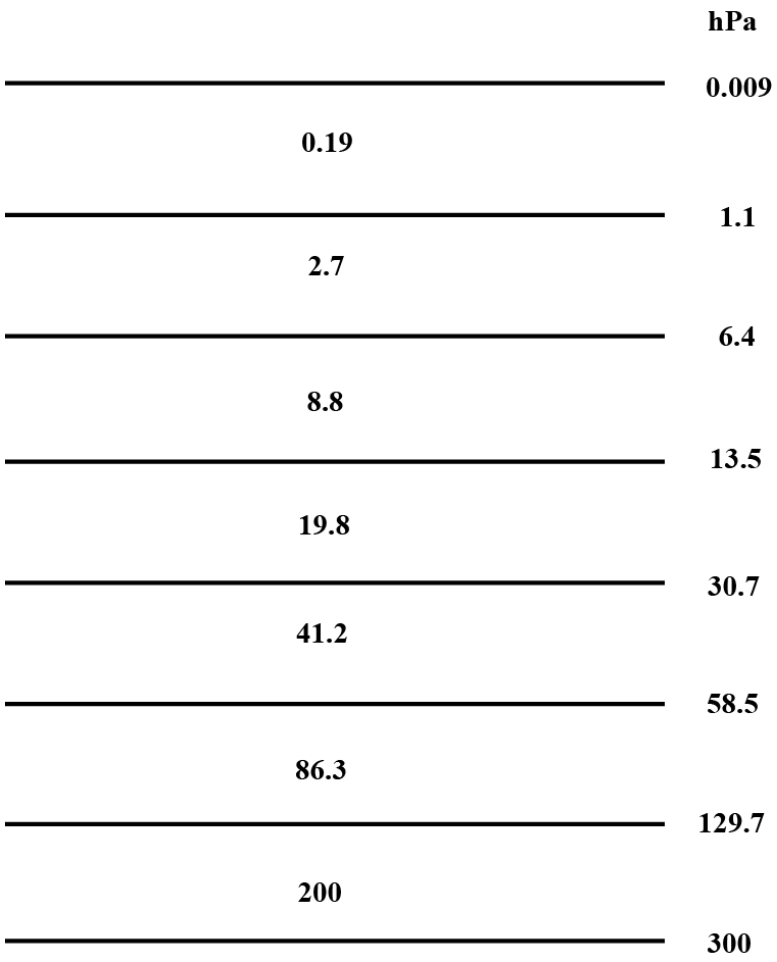

Figure 3.3. The seven layers used in this study for constructing spectral fingerprints for temperature change. The pressure boundary of each layer is labeled at right and layer-averaged pressure is shown in the center. The unit for all values is hPa.

8.8hPa, 19.8hPa, 41.2hPa, and 86.3hPa, respectively. The spectral fingerprints **S** are constructed by perturbing the temperature in different stratospheric layers and CO_2 in the calculation of synthetic radiances mentioned in the previous section. Technically this is done by the spectral radiative kernels technique (Huang et al., 2014; Pan et al., 2015). First the monthly output from 500-year pre-industry control run by GFDL CM3 (Donner et al., 2011) and 240-year pre-industry control run by HadGEM2-CC (Martin et al., 2011) models, both available from the CMIP5 (Couple Model Intercomparison Project, Phase 5) archive, are fed into the PCRTM (Principle Component based Radiative Transfer Model, Liu et al., 2006) to

generate synthetic AIRS radiances and into the CRTM (Community Radiative Transfer Model, Weng et al., 2005) to produce synthetic AMSU-A radiances. The CO_2 spectral fingerprint is then defined as the changes of radiances in response to a 1ppmv increase of CO_2 while other geophysical parameters remain unchanged. The spectral fingerprints for temperature in a given layer are defined as the changes of radiances in response to a 1K increase of temperature in that layer. The monthly spectral fingerprint is computed on each model grid box and then weighted by the cosines of their latitudes to obtain a set of global-mean spectral fingerprint.

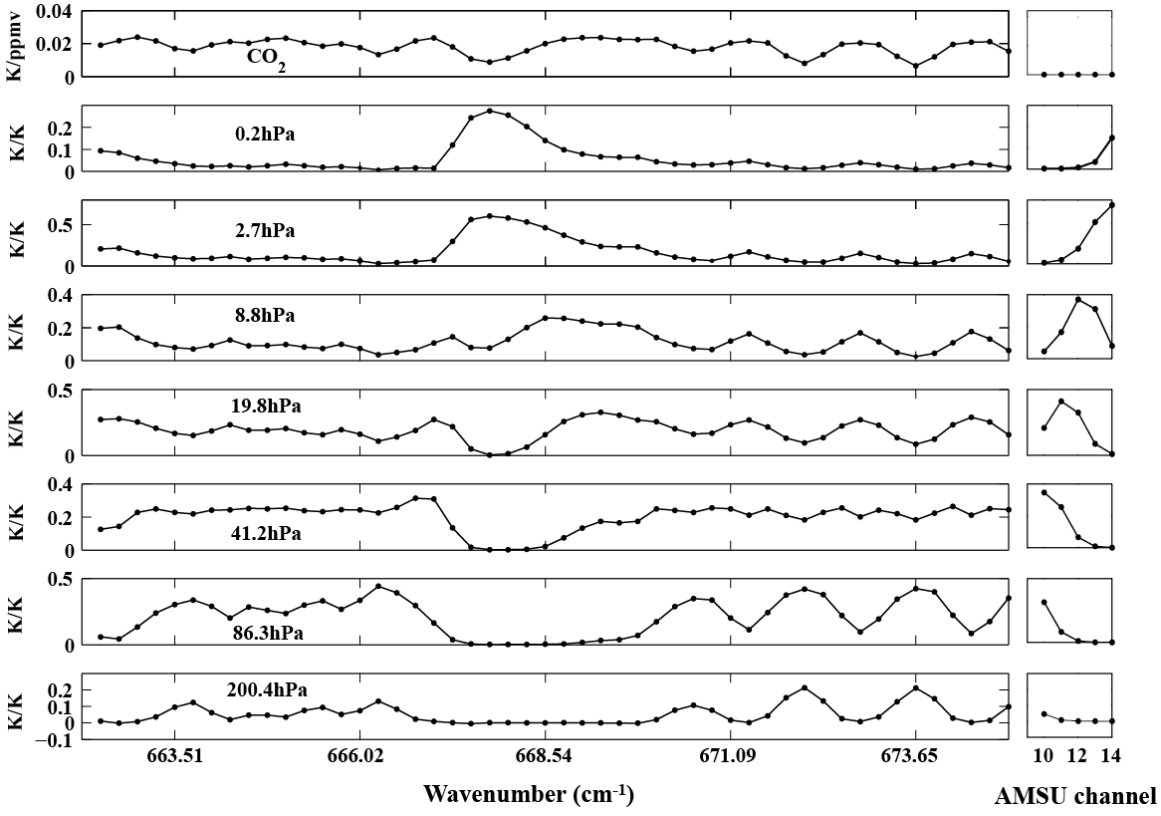

Figure 3.4. The spectral fingerprints for CO_2 and temperature changes in seven different layers. The layer-mean pressure is labeled on the panel. The spectral radiance change is expressed in terms of brightness temperature change with respect to 1ppmv change of CO_2 mixing ratio or 1K change of temperature.

Spectral fingerprints are derived using every 10 years of simulations from the GFDL CM3 and HADGEM2-CC control runs. Thus, we have 74 sets of estimated fingerprints $\mathbf{S_i}$. The mean of the 74 sets of $\mathbf{S_i}$ are used as $\mathbf{S}$ in equation (3.3) and shown in Fig. 3.4. $\delta\mathbf{S_i} = \mathbf{S_i}\text{-}\mathbf{S}$ is then used to construct the fingerprint uncertainty covariance matrix $\mathbf{\Sigma_s}$ in equation (3.6).

3.2.2.3 Estimation of natural variability

The 500-year GFDL CM3 and 240-year HADGEM2-CC control runs are used to construct natural variability of infrared and microwave brightness temperatures. There are several reasons for qualifying climate model output for studies of stratospheric variability, among them the lack of a solar cycle in the forcing of the models and poor reproductions of the quasi-biennial oscillation and polar sudden stratospheric warming events. For these reasons, we compare the two climate models' simulations of stratospheric temperature with 29 years of de-trended radiosonde observations (1979-2007) from 47 stations compiled in the RATPAC-lite data set, a subset of RATPAC (Radiosonde Atmospheric Temperature Products for Assessing Climate) recommended for climate trend studies (Randel et al., 2006; 2009). Figure 3.5 shows the PDFs (probability density functions) of modeled and observed temperature anomalies for four different pressure levels in the stratosphere at six RATPAC-lite stations ranging from south to north. The PDFs for the temperature anomalies by the models' control runs are estimated by computing PDFs for multiple non-overlapping 29-year intervals of control run output and then averaging those PDFs together for each model separately. Overall, the models' PDFs of stratospheric temperature variability correspond well to observed variability in all pressure levels, though both models tend to overestimate

the PDF spread in the polar regions and underestimate it in the tropics. The PDFs for other RATPAC-lite stations are similar to those shown in Fig. 3.5.

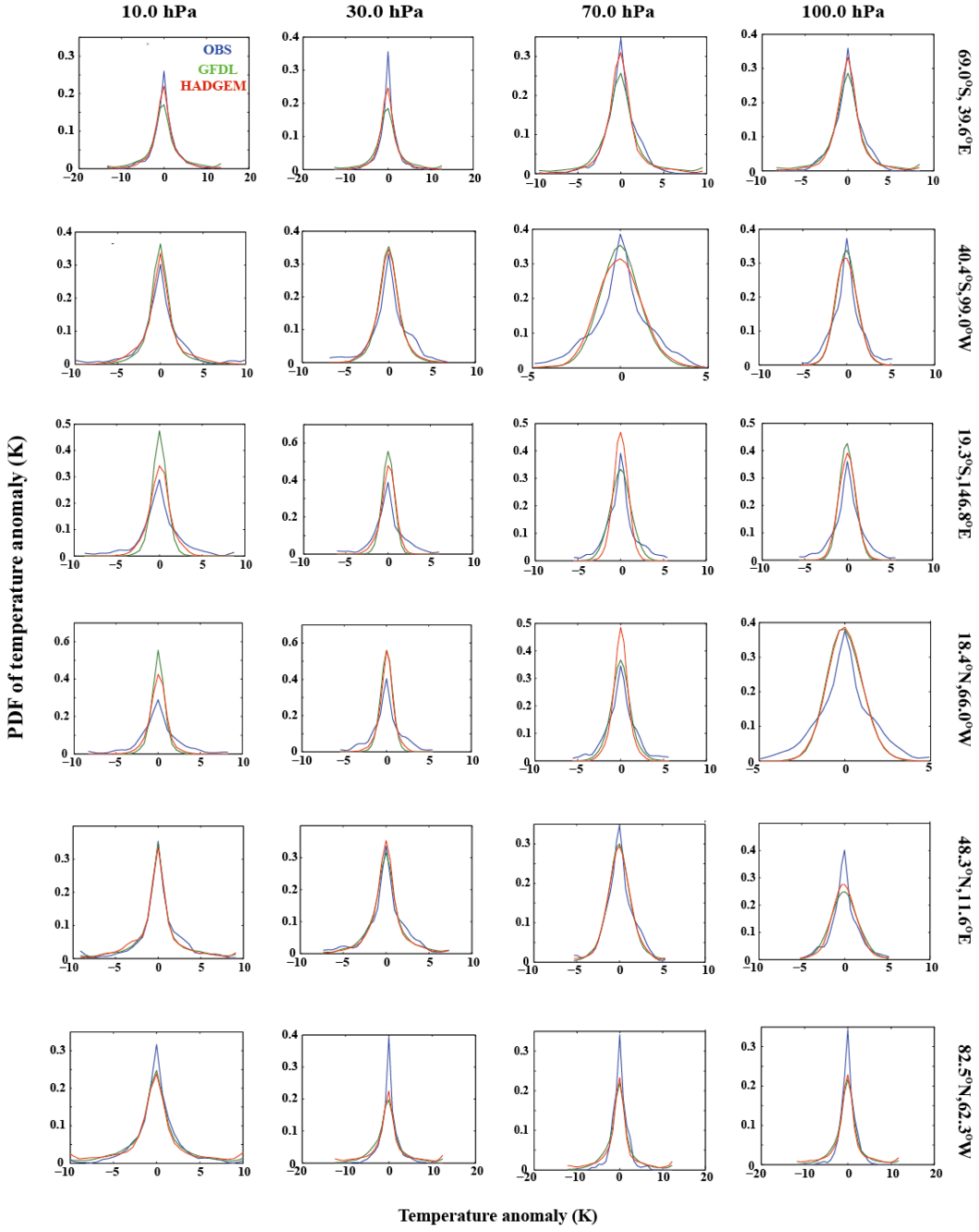

Figure 3.5. The probability density function (PDF) of stratospheric temperature anomalies as simulated by the GFDL CM3 (green curves) and HadGEM2-CC control runs (red curves). The PDF of detrended and deseasonalized monthly-mean temperature anomalies from RATPAC-lite radiosonde observations are shown in blue. The PDFs are shown for six stations from Antarctic region to Arctic region and for four different levels in the stratosphere. The PDF is estimated using kernel density estimation method (*Jones et al.*, 1996) and the unit for abscissa of all panels is K.

Using the output from 500-year GFDL CM3 and 240-year HADGEM2-CC pre-industry control runs, the synthetic brightness temperatures of the 50 AIRS stratospheric channels in CO_2 ν_2 band and of the AMSU-A channel 10-14 are simulated as follows: monthly mean profiles of temperature, humidity, ozone, and cloud on each grid box are fed into the radiative transfer models to generate the brightness temperatures over the stratospheric channels used in this study. Then global averages of simulated synthetic brightness temperature are calculated and are used to form 74 segments of 10-year time series. We use each segment to compute its own 10-year linear trend, in a way similar to how the observed climate change $\Delta\mathbf{d}$ is computed.

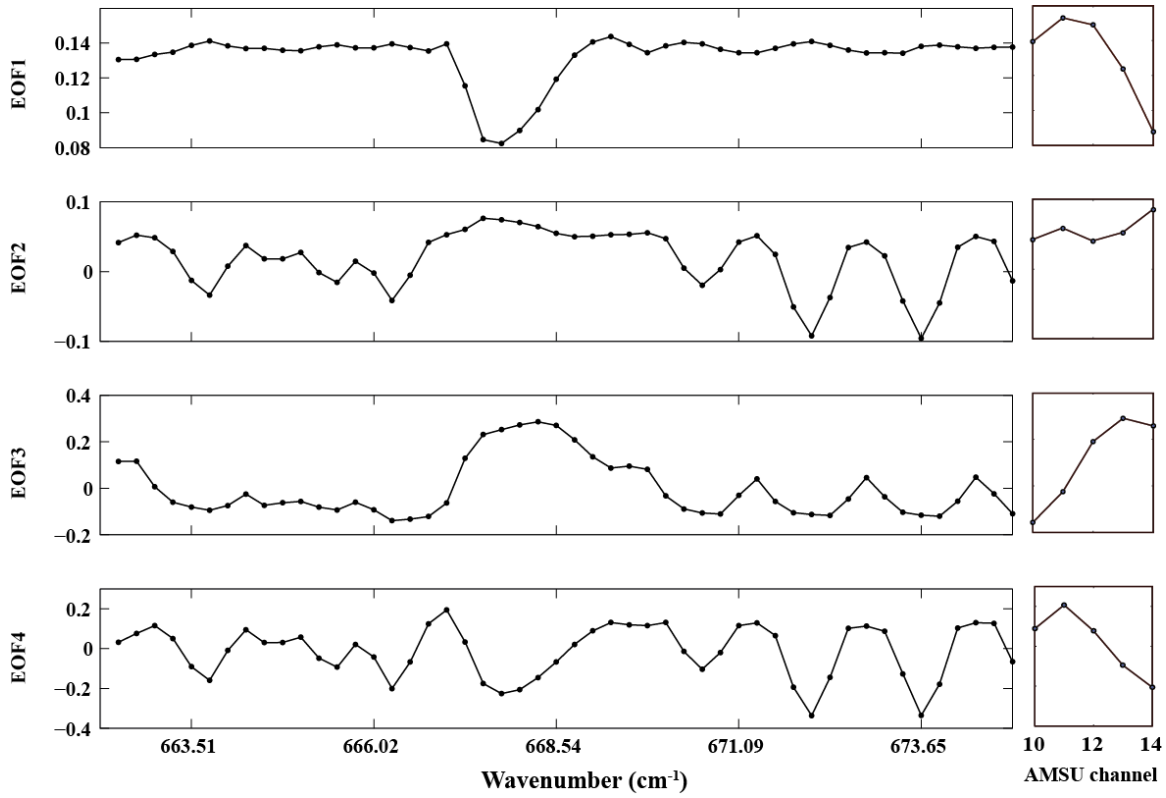

Figure 3.6. The four leading EOFs of the covariance matrix of the natural variability, which are plotted with respect to the AIRS channel frequencies and AMSU-A channel number.

The 74 realizations of such linear trend from GCM control runs form δε in our study. They pass the one-sample Kolmogorov-Smirnov test and thus can be presumed observing Gaussian distribution, an important assumption in the optimal fingerprinting for the natural variability term. Thus we can proceed to calculate the covariance matrix $\mathbf{\Sigma_n}$ using equation (3.5) in the text. To obtain the inverse matrix in equation (3.3) requires EOF (empirical orthogonal function, a.k.a. principal component) decomposition in order to maintain numeric stability in the inversion. Figure 3.6 show the first 4 eigenvectors of the natural variability covariance matrix $\mathbf{\Sigma_n}$. The first 4 eigenvectors explain 67.2%, 22.3%, 8.6% and 1.0% of the total variance, respectively. In practice, 34 leading EOFs are used for inverting the matrix in equation (3.3).

3.3 Results and discussion

3.3.1 Retrieved stratospheric temperature and CO_2 change

Red lines in Fig. 3.7 are decadal stratospheric temperature trends inferred from the AIRS and homogenized AMSU-A data using optimal fingerprinting detection. Taking natural variability as inferred from the climate models (subsection 3.2.2.3) into account, the stratosphere still exhibits cooling trends within 10 years at 95% significance level in all the layers except the lowest layer near 100hPa. The magnitudes of such cooling trends increase with height. The globally averaged cooling rate in the lower stratosphere (30–59hPa) is 0.39±0.32(2σ) K decade^{-1} and for the two middle stratospheric layers (14–30hPa and 6–14hPa) it is 0.46 K decade^{-1}, respectively, all with a 2-σ uncertainty around 0.23 K decade^{-1}. The cooling rate in the upper stratosphere above 6hPa is 0.65±0.11 K decade^{-1}.

Our results for stratospheric temperature trends are consistent with those determined using other data sets. Linear temperature trends in the stratosphere from 1979 to 2007 have been examined using SSU, MSU, and radiosonde data (Randel et al., 2009) and it is found that the upper stratosphere has a larger cooling trend than the lower stratosphere. A recent study (Zou et al., 2016) homogenized SSU observations from 1978 to 2016 for layer-mean

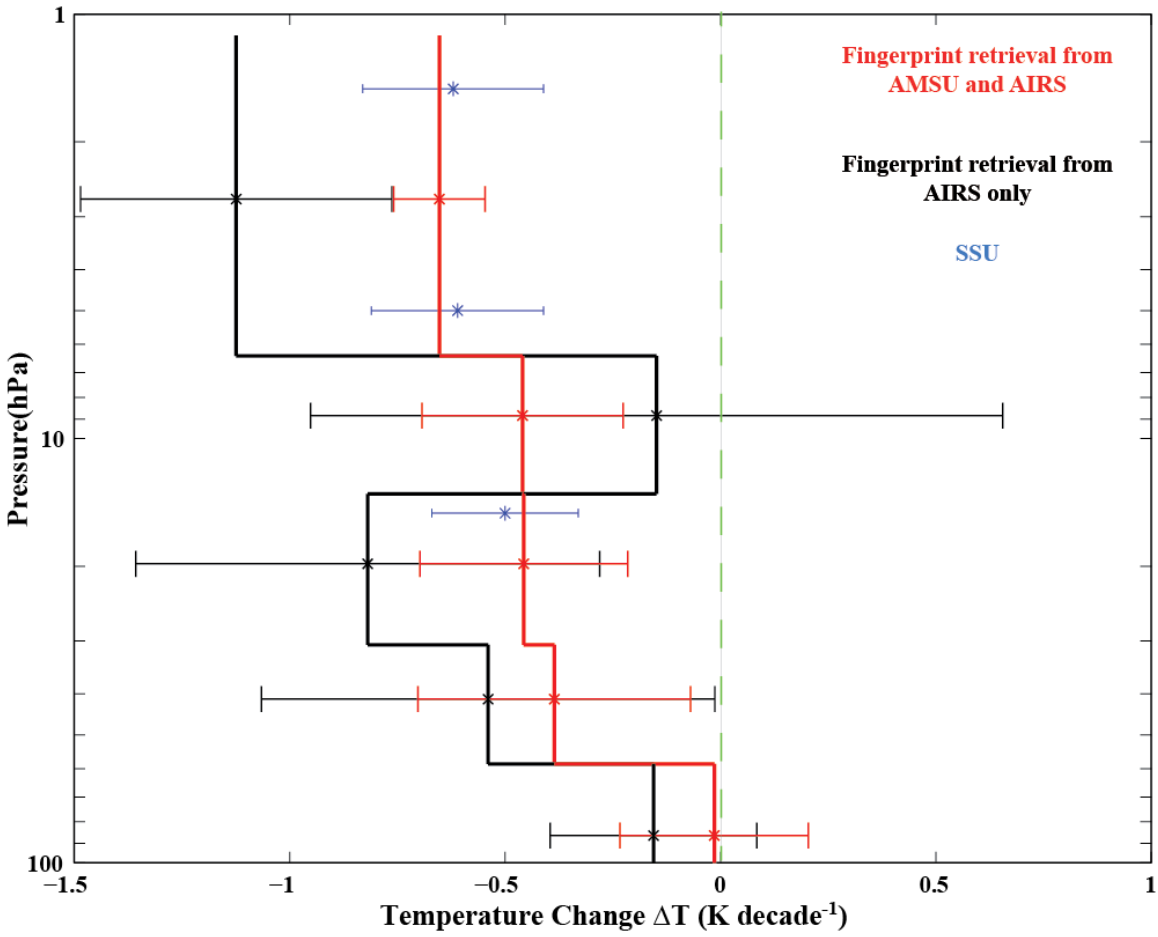

Figure 3.7. The temperature changes of five stratospheric layers due to external forcing as estimated using the optimal fingerprinting technique. Red lines are the results using both the AIRS and AMSU-A observations and black lines are the results using the AIRS data alone. Blue lines are the results for the layer-mean temperatures in TMS, TUS, TTS by homogenized SSU data record. Horizontal ticked line indicates the 2-σ uncertainty.

temperatures of the mid-stratosphere (TMS, centered at ~15hPa), of the upper-stratosphere (TUS, ~5hPa), and of the top-stratosphere (TTS, ~1.5hPa). The global-mean temperature

trends over the period of 2003 to 2012 from the homogenized SSU data record are -0.50±0.17 K decade^{-1} for the TMS, -0.61±0.20 K decade^{-1} for the TUS, and -0.62±0.21 K decade^{-1} for the TTS. These trend estimates (blue stars in Fig. 3.7) are consistent with our results. Note our inference of stratospheric cooling is an optimal determination of the presence of a long-term climate trend distinct from natural variability but is not an attribution to a specific cause such as the solar cycle or increasing stratospheric carbon dioxide.

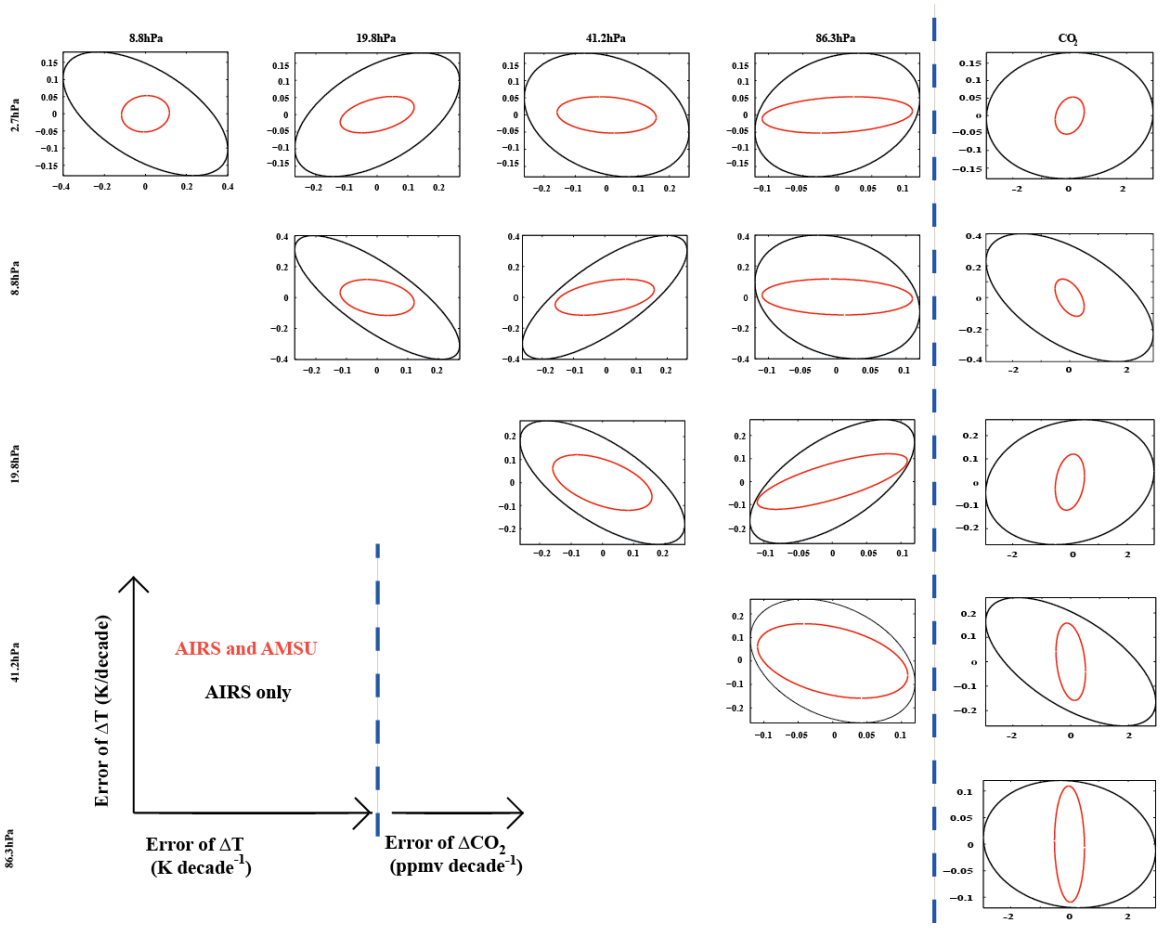

Figure 3.8. 1-σ error covariance for estimated temperature changes and CO_2 changes due to external forcing. The panels are arranged according to the columns (abscissa) and the rows (ordinate), e.g., the first panel on the first row is the error covariance between estimated temperature changes at 2.7hPa and 8.8hPa. The ordinate unit is K decade^{-1} for all panels and the abscissa unit is K decade^{-1} for the first four columns and ppmv decade^{-1} for the last column. Red ellipses are the results using both AIRS and AMSU-A observations while black ones are the results using AIRS alone.

Error covariances between the estimated temperature changes and between estimated temperature and CO_2 changes are shown as red ellipses in Fig. 3.8. Each ellipse shows the 1-σ error with respect to the optimal estimate of $\Delta\alpha_i$ in Equation 3.1. The first four columns of Fig. 3.8 show that errors in estimated temperature change in different layers are largely uncorrelated. Among 10 panels of error covariance between estimated temperatures change in different layers, weak correlations only exist between estimated changes in three layers that are centered at 20hPa, 41hPa, and 86hPa. Anti-correlation of errors between adjacent layers is a signature of over-representation of vertical resolution: a positive error in one layer and a negative error in an adjacent layer roughly cancel each other in order to explain the data, and no information exists to distinguish between the adjacent layers. The last column in Fig. 3.8 shows that error in estimated CO_2 rising rate has little correlation with errors in estimated stratospheric temperature changes in all five layers, which suggests that, if a bias exists in the estimated CO_2 rising rate, it does not affect the estimated temperature changes in all five stratospheric layers.

3.3.2 Further discussion about the stratospheric CO_2 change

Our results give an estimate of the stratospheric CO_2 change at $1.57\pm0.10(2\sigma)$ ppmvyr^{-1}. Transport of CO_2 from the troposphere to the stratosphere suggests that the stratospheric CO_2 change up to 35km is lagged behind the surface CO_2 change by 4-5 years (Engel et al., 2009). Such time lag, usually termed as age of air, can be as large as 5-7 years for the extra tropics in the low-mid stratosphere and for the globe in the upper stratosphere (Table 1 in Waugh et al., (2002), with considerable variation based on location and method of observations). Using the surface observations of CO_2 compiled by NOAA/ESRL (National

Oceanic and Atmospheric Administration, Earth System Research Laboratory, *Tans et al.*, 2011), a ~4year time lag would lead to 1.9 ppmv yr^{-1} increase of the stratospheric CO_2 for the 10-year period examined here, which is larger than our estimate. This underestimate of CO_2 change can be due to a few reasons: 1. The CO_2 natural variability is assumed zero in our method as the climate models that we used do not simulate time-dependent CO_2 concentration but in reality the CO_2 does have spatial and temporal variability; 2. The models are limited to represent the residual term $\boldsymbol{\delta\varepsilon}$ which is more than just natural variability so that the uncertainty of CO_2 increase could be lower-estimated; 3. Given the intrinsic spread in the full age of air spectrum and the transport nature in the stratosphere (Waugh et al., 2002), it is possible that the CO_2 increase rate in the upper stratosphere is smaller than that in the lower and middle stratosphere. For example, an 8-year time lag would lead to a CO_2 trend of 1.8 ppmv yr^{-1}. There have been few in-situ observations available for the age of air in the upper stratosphere (Martell et al., 1973; Waugh et al., 2002), thus it is difficult at this moment to quantify this possible cause further.

To understand the impact of this underestimated CO_2 rising rate on stratospheric temperature changes detected in this study, we have carried out two sensitivity tests (Fig. 3.9a and 3.9b). In the first test, we artificially increase the amplitude of CO_2 spectral fingerprint in Fig. 3.4 by a factor of 10 before applying the optimal fingerprinting study. The estimated temperature changes are then shown as green lines in Fig. 3.9a, which are essentially no difference from the estimated temperature changes in the result section (red lines in Fig. 3.7). In the second test, we assume a different CO_2 vertical profile in the stratosphere from the

default one in the PCRTM, the radiative transfer model used in this study. The default PCRTM CO_2 mixing ratio decreases from 368.3ppmv at 100hPa to 364ppmv at 1hPa.

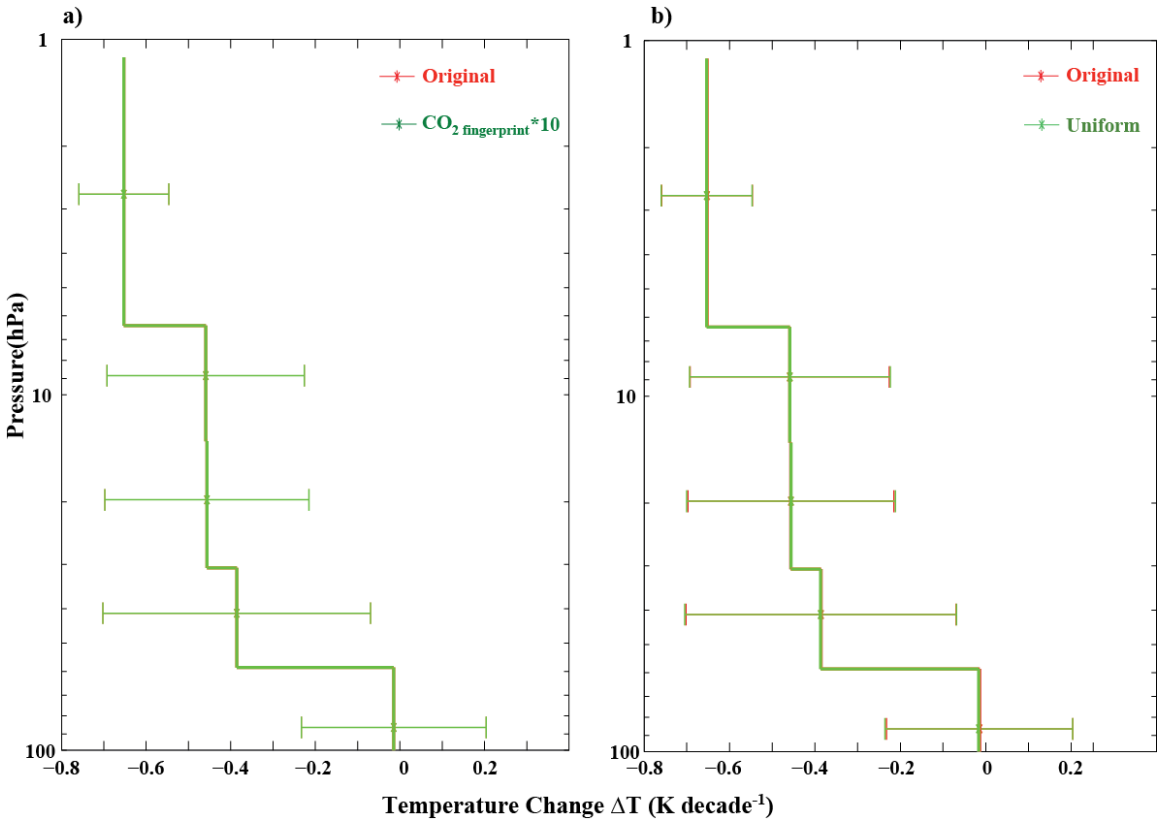

Figure 3.9. The stratospheric temperature changes in response to external forcing. Red lines are the results using AIRS and AMSU-A together shown in Fig. 3.7 in the text, in which the CO2 spectral fingerprint is derived assuming the default CO2 background profile in the PCRTM. a) Green lines are the results when the amplitude of CO2 spectral fingerprint is artificially increased by a factor of 10. b) Green lines are derived using a different background CO2 profile (constant mixing ratio in the stratosphere) in the calculation of CO2 spectral fingerprint.

We here assume a constant mixing ratio of 368.3ppmv through the entire stratosphere. Then we obtain a new CO_2 spectral fingerprint and derive the estimated temperature change accordingly. The results are shown in Fig. 3.9b as green lines. There are only little differences from the results in the section 3.3.1 (red lines in Fig. 3.7). Both results support the inference based on error covariances between CO_2 and temperature estimates as shown in Fig. 3.8, i.e., the error in the estimate of CO_2 rising rate has little impact on the estimated

stratospheric temperature change. The results suggest that the error in CO_2 estimates has little impact on the estimated temperature changes, which is consistent with plots of the error covariance shown in Fig. 3.8 and discussed in the previous paragraph.

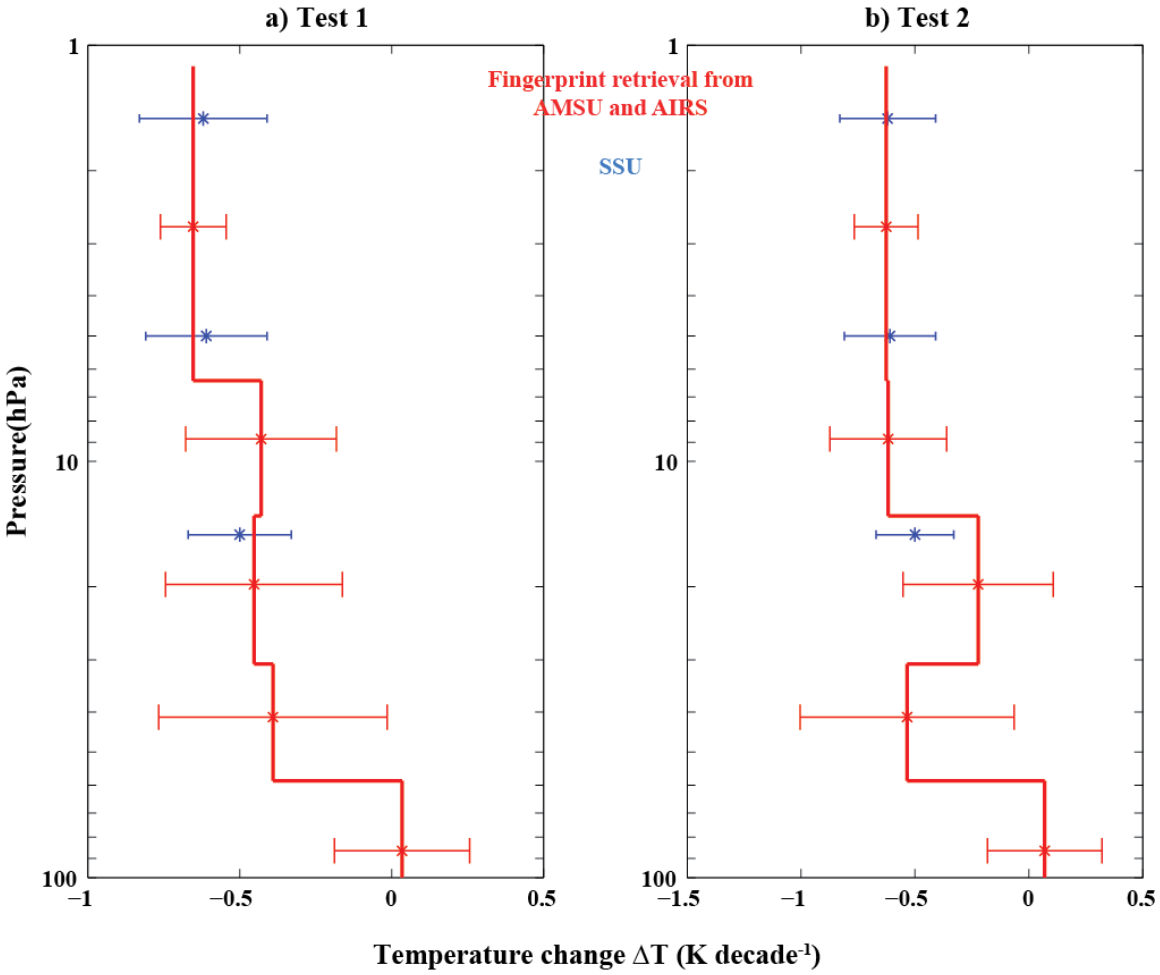

Figure 3.10. The stratospheric temperature changes in response to external forcing when there are two CO_2 fingerprints considering the vertical structure of stratospheric CO_2 change. Red lines are the results using AIRS and AMSU-A together similar to Fig. 3.8 in the text. a) The stratosphere is divided into two uniform layers at 10hPa. b) The magnitude of CO_2 change is assumed linearly decrease from 70hPa to 1hPa. Blue lines are the results for the layer-mean temperatures in TMS, TUS, TTS by homogenized SSU data record.

Since in this study we assume the CO_2 is uniform in the atmosphere while it is possible that CO_2 change in the upper stratosphere is different from that in the middle and

lower stratosphere, we also carry out two test experiments considering the vertical structure of stratospheric CO_2 change by adding one variable for CO_2 in $\Delta\boldsymbol{\alpha}$. In the first test, we separate the stratosphere into two uniform layers for CO_2 change, one is above the 10hPa and the other one is below the 10hPa. Then we perform the optimal fingerprinting technique from the AIRS and AMSU-A data again. The decadal stratospheric temperature trends are shown as red lines in Fig. 3.10a. The decadal CO_2 trend in the upper stratosphere is 1.61±0.27(2σ) ppmv yr^{-1} while in the middle and lower stratosphere it is 1.36±0.27(2σ) ppmv yr^{-1}. The CO_2 changes in the two layers are highly correlated with an error correlation of -0.71. In the second test, one variable is still for uniform CO_2 in the stratosphere. The other one represents how much the CO_2 change at 1hPa is less than the change at 70hPa when the CO_2 change linearly decrease from 70hPa to 1hPa. Under the new construction of fingerprints, the decadal stratospheric temperature trends are shown as red lines in Fig. 3.10b. The decadal CO_2 trend at 70hPa is 1.88±0.80(2σ) ppmv yr^{-1} while up to 1hPa the magnitude of CO_2 trend reduces by 0.63±1.00(2σ) ppmv yr^{-1} (2σ). However, the two new CO_2 fingerprints are so similar that their error correlation is as high as 0.99.

3.3.3 Synergy of microwave and infrared radiances

Distinguishing between carbon dioxide change and stratospheric temperature changes becomes more difficult and posterior uncertainty in stratospheric temperature changes becomes worse when AMSU-A radiances are not included in the spectral fingerprints. The estimated stratospheric temperature trends are shown as black lines in Fig. 3.7 and the corresponding error covariance plots are shown as black ellipses in Fig. 3.8 when the AMSU-A channels are removed from the spectral fingerprints. There are three consequences of

removing the AMSU-A data: (1) the estimated CO_2 change becomes less certain ($1.05\pm0.60 ppmvyr^{-1}$), (2) the posterior uncertainty of estimated stratospheric temperature changes becomes worse, and (3) errors in stratospheric temperature changes become more strikingly anti-correlated between adjacent layers. The correlation of errors between carbon dioxide change and stratospheric temperature changes becomes stronger, all of which is a consequence of the loss of information on carbon dioxide change. Such differences confirm the merit of the AMSU-A radiances in the spectral fingerprinting study: its independence with respect to CO_2 change can help successfully disentangle the similarity among the infrared spectral fingerprints as shown in Fig. 3.4. In practice, Fig. 3.7 and Fig. 3.8 demonstrate that the joint use of AIRS and AMSU-A brightness temperatures not only narrows the uncertainty of estimated changes but also increases the effective vertical resolution of retrieved stratospheric temperature trends.

3.4 Conclusion

We have demonstrated that optimal fingerprinting, when applied to 10 yrs of high spectral resolution infrared data and passive microwave data, can detect decadal changes in stratospheric temperature and carbon dioxide that is unexplained by natural variability within 2-σ uncertainty. The joint use of infrared and microwave brightness temperature anomalies effectively reduces uncertainties of the estimated changes of stratospheric temperature and carbon dioxide. It also improves the vertical resolution of the profile stratospheric temperature changes and the distinction between carbon dioxide and temperature in satellite data. The hyperspectral IR data such as that obtained by AIRS makes it possible to estimate the temperature changes with higher vertical resolution than the previous generation of global

satellite observations. Data from high-quality hyperspectral IR measurements from current and future missions such as AIRS, IASI, CrIS and CLARREO should provide information-rich constrains on long-term trends in the atmosphere, including the stratosphere. Like passive nadir microwave radiance, the GPS radio occultation is also insensitive to CO_2 change but can offer accurate temperature retrievals in the lower and middle stratosphere. Therefore, similar synergistic use of GPS occultation and infrared radiance can be useful for studying climate change as well (Goody et al., 1998; Huang et al., 2010b).

While most climate-change studies use the climatology of geophysical parameters retrieved from satellite observations (the so-called retrieve-then-average approach), this study for the first time shows that optimal fingerprinting can be applied directly to observed radiances to detect climate changes (the average-then-retrieve approach). This study also suggests that, in addition to MSU and SSU that have been extensively used in stratospheric temperature change studies, new generation of hyperspectral sounders such as AIRS can also start to contribute to the studies of stratospheric climate.

3.5 Acknowledgements

The GFDL-CM3 and HadGEM2-CC simulation outputs are obtained from CMIP5 archives via https://pcmdi.llnl.gov/projects/esgf-llnl. The AIRS level-1b data are obtained from NASA GSFC DAAC. The global-mean AMSU-A data are directly obtained from Remote Sensing System via http://images.remss.com/msu/msu_time_series.html. This research is supported by NASA Grants NNX14AJ50G and NNX15AC25G awarded to the University of Michigan. It is also supported by NASA grant NNX14AR33G Awarded to

Harvard University. One co-author Huang is thankful to NOAA/GFDL and Princeton University for hosting his sabbatical, which leads to this study.

References

1. Aumann, H. H., S. Broberg, D. Elliott, S. Gaiser and D. Gregorich, 2006, Three years of AIRS radiometric calibration validation using sea surface temperatures, *J. Geophys. Res.*, **111**, D16S90, doi:10.1029/2005JD006822.

2. Aumann, H. H. and T. S. Pagano, 2008, Using AIRS and IASI data to evaluate absolute radiometric accuracy and stability for climate application, *Proc. SPIE Int. Soc. Opt. En.g*, 7085, doi:10.1117/12.795225.

3. Barnett, T. P., et al., 2008, Human-induced changes in the hydrology of the western United States, *Science*, **319**, 1080-1083, doi:10.1126/science.1152538.

4. Bell, T. L., 1986, Theory of optimal weighting of data to detect climatic change, *J. Atmos. Sci.*, **43**, 1694-1710.

5. Chahine, M. T., et al., 2006, The atmospheric infrared sounder (AIRS): Improving weather forecasting and providing new data on greenhouse gases, *Bull. Am. Meteorol. Soc.*, **87**, 911–926, doi:10.1175/BAMS-87-7-911.

6. Christy, J. R., R. W. Spencer, W. B. Norris, and W. D. Braswell, 2003: Error estimates of version 5.0 of MSU-AMSU bulk atmospheric temperature. *J. Atmos. Oceanic Technol.*, **20**, 613–629, doi:10.1175/1520-0426(2003)20<613:EEOVOM>2.0.CO;2.

7. Clough, S. A., et al., 2005, Atmospheric radiative transfer modeling: A summary of the AER codes, *J. Quant. Spectrosc. Radiat. Transfer.*, **91**, 233–244, doi:10.1016/j.jqsrt.2004.05.058.

8. Dee, D. P., et al., 2011, The ERA-Interim reanalysis: configuration and performance of the data assimilation system, *Quart. J. Roy. Meteor. Soc.*, **137**, 553-597, doi:10.1002/qj.828.

9. Donner, L. J., et al., 2011, The dynamical core, physical parameterizations, and basic simulation characteristics of the atmospheric component AM3 of the GFDL global coupled model CM3, *J. Clim.*, **24,** 3484-3519, doi:10.1175/2011JCLI3955.1.

10. Engel, A., et al,. 2009, Age of stratospheric air unchanged within uncertainties over the past 30 years, *Nature Geoscience*, **2**, 28-31, doi:10.1038/ngeo388.

11. Gaiser, S., H. Aumann, L. L. Sttrow, S. Hannon and M. Weiler, 2003, In-flight spectral calibration of the Atmospheric Infrared Sounder, *IEEE Trans. Geosci. Remote Sens*, **41**, 287-297, doi: 10.1109/TGRS.2003.809708.

12. Goodrum G., et al., 2010, NOAA KLM user's guide. Available at http://www.ncdc.noaa.gov/oa/pod-guide/ncdc/docs/klm/cover.html.

13. Goody, R., J. Anderson and G. North, 1998, Testing climate models: An approach, *Bull. Am. Meteorol. Soc.*,**79**(11), 2541-2549.

14. Hasselmann, K, 1993, Optimal fingerprints for the detection of time-dependent climate change, *J. Climate.,* **6**, 1957-1971.

15. Hasselmann, K, 1997, Multi-pattern fingerprint method for detection and attribution of climate change, *Climate Dyn,* **13**, 601-611.

16. Huang. X., X. Chen, B. J. Soden and X. Liu, 2014, The spectral dimension of longwave feedback in the CMIP3 and CMIP5 experiments, *Geophys. Res. Lett.,* **41**, 7830-7837, doi:10.1175/JCLI-D-14-00436.1.

17. Huang, Y., S. Leroy, P. J. Gero, J. Dykema, and J. Anderson, 2010a, Separation of Longwave Climate Feedbacks from Spectral Observations, *J. Geophys. Res.,* **115**, D07104, doi:10.1029/2009JD012766.

18. Huang, Y., S. S. Leroy, and J. G. Anderson, 2010b, Determining longwave forcing and feedback using infrared spectra and GNSS radio occultation, *J. Climate,*. **23**, 6027-6035, doi:10.1175/2010JCLI3588.1.

19. Jones, M. C., J. S. Marron and S. J. Sheather, 1996, Progress in data-based band width selection for kernel density estimation, *Computational Statistics,* **11**, 337-381.

20. Leroy, S. S., J. G. Anderson and J. A. Dykema, 2006, Testing climate models using GPS radio occultation: A sensitivity analysis, *J. Geophys. Res.,* **111**, D17105, doi:10.1029/2005JD006145.

21. Leroy, S., J. G. Anderson, J. Dykema, and R. Goody ,2008, Testing climate models using thermal infrared spectra, *J. Climate.,* **21**, 1863-1875.

22. Leroy, S. S., and J. G. Anderson (2010), Optical Detection of Regional Trends Using Global Data, *J. Climate.,* **23**, 4438-4446, doi:10.1175/2010JCLI3550.1.

23. Liu, X., W. L. Smith, D. K. Zhou and A. Larar, 2006, Principal component-based radiative transfer model for hyperspectral sensors: theoretical concept, *Applied optics,* **45**, 201-209, doi:10.1364/AO.45.000201.

24. Martell, E.A., 1973, The distribution of minor constituents in the stratosphere and lower mesosphere, *Physics and Chemistry of Upper Atmosphere* 24-33.

25. Martin, G. M., et al., 2011, The HadGEM2 family of met office unified model climate configurations, *Geoscientific Model Development,* **4**, 723-757, doi:10.5194/gmd-4-723-2011.

26. Mears., C. A. and F. J. Wentz, 2009, Construction of the remote sensing systems V3.2 atmospheric temperature records from the MSU and AMSU-A microwave sounders, *J. Atmos. Oceanic Technol.*, **26**, 1040-1056, doi:10.1175/2008JTECHA1176.1.

27. Mears., C. A, F. J. Wentz, P. Thorne and D. Bernie, 2011, Assessing uncertainty in estimates of atmospheric temperature changes from MSU and AMSU using a Monte-

Carlo estimation technique, *J. Geophys. Res.*, **116**, D08112, doi:10.1029/2010JD014954.

28. North, G. R., et al., 1995, Detection of forced climate signals. Part 1: Filter theory, *J. Climate.*, **8**, 401–408.

29. Pagnao., T, S, H. H. Aumann, D. E. Hagan and K. Overoye, 2003, Prelauch and in-flight radiometri calibration of the Atmospheric infrared Sounder (AIRS). *IEEE Trans. Geosci. Remote Sens.*, **41**, 265-273.

30. Pan, F, et al, 2015, Linear Trends and Closures of 10-yr Observations of AIRS Stratospheric Channels, *J. Climate.*, **28**, 8939-8950, doi:10.1175/JCLI-D-15-0418.1.

31. Ramaswamy, V., et al., 2001, Stratospheric temperature trends: Observations and modelsimulation, *Rev. Geophys.*, **39**, 71-122, doi:10.1029/1999RG000065.

32. Ramaswamy, V., et al., (2006) Anthropogenic and natural influences in theevolution of lower stratospheric cooling. *Science*, **311**, 1138-1141, doi:10.1126/scienc.1122587.

33. Randel, W. J. and F. Wu, 2006, Biases in stratospheric and tropospheric temperature trends derived from historical radiosonde data, *J. Climate.*, **19**, 2094-2104, doi:10.1175/JCLI3717.1.

34. Randel, W. J., et al., 2009, An update of observed stratospheric temperature trends, *J. Geophys. Res.*, **114**, D02107, doi:10.1029/2008JD010421.

35. Randel, W. J.., et al., 2016, Stratospheric temperature trends over 1979–2015 derived from combined SSU, MLS, and SABER satellite observations. *J. Climate.*, **29**, 4843-4859, doi: 10.1175/JCLI-D-15-0629.1.

36. Santer, B. D., et al., 2003, Contributions of anthropogenic and natural forcing to recent tropopause height changes, *Science*, **201**, 479-483, doi:10.1126/science.1084123.

37. Santer, B. D., et al., 2007, Identification of human-induced changes in atmospheric moisture content, *Proceedings of the National Academy of Sciences*, **104**, 15248-15253, doi:10.1073/pnas.0702872104.

38. Seidel, D. J., et al., 2011, Stratospheric temperature trends: Our evolving understanding, *Wiley Interdiscip. Rev. Climate change.*, **2**, 592-616, doi:10.1002/wcc.125.

39. Seidel, D. J., et al., 2016, Stratospheric temperature changes during the satellite era, *J. Geophys. Res.*, **121,** 664-681, doi:10.1002/2015JD024039.

40. Strow, L. L., S. E. Hannon, S. De-Souza Machado, H. E. Motteler and D. C. Tobin, 2006, Validation of the atmospheric Infrared Sounder radiative transfer algorithm, *J. Geophys. Res.*, **111**, D09S06, doi:10.1029/2005JD006146.

41. Tans, P. and R. Keeling, 2011, Trends in atmospheric carbon dioxide, *NOAA Earth Systems Research Laboratory.*

42. Tompson, D. W., et al., 2012, The mystery of recent stratospheric temperature trends, *Nature*, **491**, 692-697, doi:10.1038/nature11579.

43. Wang, W, and Zou, C.Z., 2014, AMSU-A-only atmospheric temperature data records from the lower troposphere to the top of the stratosphere. *J. Atmos. Oceanic Technol.*, **31**, 808-825, doi: 10.1175/JTECH-D-13-00134.1.

44. Waugh, D. W. and T. M. Hall, 2002, Age of stratospheric air: Theory, observations, and models, *Rev. Geophys.*, **40**, 1-10, doi:10.1029/2000RG000101.

45. Weng, F., et al., 2005, JCSDA community radiative transfer model (CRTM), *Proc 14th Int ATOVS Study Conf*, 217-222.

46. Zou, C. Z. and W. Wang, 2010, Stability of the MSU-derived atmospheric temperature trend, *J. Atmos. Oceanic Technol*., **27**, 1960-1971, doi: 10.1175/2009JTECHA1333.1.

47. Zou, C.-Z., H. Qian, W. Wang, L. Wang, and C. Long, 2014, Recalibration and merging of SSU observations for stratospheric temperature trend studies, *J. Geophys. Res. Atmos.*, **119**, 13,180–13,205, doi:10.1002/2014JD021603.

48. Zou, C. Z. and H. Qian, 2016, Stratospheric Temperature Climate Data Record from Merged SSU and AMSU-A Observations, *J. Atmos. Oceanic Technol.*, **33**, 1967-1984, doi:10.1175/JTECH-D-16-0018.1.

Chapter 4

The spectral dimension of relative humidity feedbacks in the CMIP5 experiments

4.1. Introduction

It is widely known that relative humidity (RH) change little in the global warming scenario simulated by the GCMs (Ingram, et al., 2002, Myles & Ingram et al., 2002, Pierrehumbert et al., 2007). Both climate models and observations indicate that global water vapor in the atmosphere will increase with global mean surface temperature by $7\%K^{-1}$, as implied by the Clausius-Clapeyron relation in response to surface warming (Frank et al., 2000, 2007; Trenberth et al 2005). Additionally, water vapor feedbacks in GCMs are also consistent with results that hold relative humidity fix (Colman & Mcavaney, 1997; Held & Soden, 2000; Soden & Held, 2006; Sherwood et al., 2010). Due to the tight coupling of temperature and water vapor changes in models, Held & Shell (2012) thought that it is physically logical to combine lapse rate and water vapor feedbacks, and thus proposed relative humidity feedback and explained procedures to calculate the Planck and lapse rate feedbacks under the RH framework. Inspecting sources of model spreads for the estimated climate sensitivity, Caldwell et al. (2016) found that the RH framework reduces covariance

between water vapor and lapse rate feedbacks, between lapse rate and longwave cloud feedbacks, and between other processes as well, making it easier to understand the feedback mechanisms than the conventional approach using specific humidity as a state variable.

In recent year, the radiative kernel method has become a popular approach to computing the radiative feedbacks from GCM archives. The method was pioneered by Soden & Held (2006), Soden et al. (2008), and Shell et al. (2008). The radiative kernel is the response of top of atmosphere (TOA) broadband flux to perturbation of certain state variable. Radiative feedback for that variable is estimated by the product of the radiative kernel and the changes of this variable between two climate states. Traditionally, these radiative feedbacks are studied in terms of broadband flux. Huang et al. (2014) extended the use of broadband radiative kernel approach to longwave spectral dimension. The spectral radiative kernel is the TOA spectral flux change at a given frequency in response to a given atmospheric or surface perturbation. Huang et al. (2014) utilized the radiative kernel technique in computing the longwave spectral radiative feedbacks instead of commonly referred broadband feedbacks. They found that the lapse rate and longwave water vapor feedbacks reveal spectrally dependent difference among GCMs. Given the new feedback framework and potential information contained in spectral longwave feedback, we calculate the spectral RH feedbacks in 16 GCMs. Based on these feedbacks, a few meaningful questions we want to investigate are:

1) Although global average broadband RH feedbacks in all GCMs are close to zero, will they also show consistence in the spectral dimension?

2) How about the spatial distribution of RH feedbacks? Could the spatial feature of RH feedbacks vary from spectrum to spectrum?

3) Can we relate spectral RH feedbacks qualitatively and quantitatively to the change of actual geophysical variables?

Focused on these questions, we will examine the spatial and spectral details of the RH feedbacks among the 16 GCMs and quantitatively analyze vertical profile of RH changes from the spectrally resolved RH feedbacks. The rest of this chapter is arranged as follows. Section 4.2 explains the method to calculate the spectral RH feedbacks in 16 GCMs. The spectral and spatial features of RH feedbacks as well as their consistence with actual RH changes are examined in the Section 4.3. Section 4.3 also discusses the relationship between regional spectral RH feedbacks and actual profiles of RH changes in several locations. Section 4.4 presents conclusions and further discussions.

4.2 Data and Method

We follow Held & Shell (2012) to replace specific humidity with RH as the state variable to compute the spectral climate feedbacks. In Held & Shell (2012), traditional water vapor feedback λ_Q (use specific humidity as the state variable) is split into three parts:

$$\lambda_Q = \lambda_{QL} + \lambda_{QT} + \lambda_H \qquad (4.1)$$

λ_{QT} is the TOA flux response to specific humidity perturbation required by fixing relative humidity while the tropospheric temperature perturbation is uniformly equal to the surface temperature change; λ_{QL} is the TOA flux response to the specific humidity perturbation

required by fixing relative humidity while tropospheric temperature is perturbed by its difference from surface temperature change. λ_H is the RH feedback that we are interested in. To obtain λ_Q, λ_{QT} and λ_{QL}, we follow the spectral radiative kernel approach in Huang et al. (2014). The longwave TOA flux change at a frequency ν in response to a state variable change x_i in a grid box (*lat*,*lon*) at a given time *t* caused by the increase of surface temperature can be approximated as:

$$\Delta R\,(lat, lon, \nu; t) = \sum_{p=1}^{N} \frac{\partial R(lat, lon, \nu; t)}{\partial x_i(p)} \Delta x_i(p) = \mathbf{K}\Delta\mathbf{X} \qquad (4.2)$$

Where the $\frac{\partial R(lat,lon,\nu;t)}{\partial x_i(p)}$ denotes spectral radiative feedback kernel (hereafter we refer the kernel as **K** for brevity) for a state variable $x_i(p)$ (specific humidity or temperature change at *p*-th level). Huang et al. (2014) described how to construct spectral radiative kernels. Specifically, one year of 3-hourly profiles of temperature, specific humidity, cloud fraction, cloud liquid and ice water content as simulated by the GFDL AM2 model (GAMDT 2004) were fed into the PCRTM (Principal component-based radiative transfer model; Liu et al., 2006, Chen et al., 2013) to simultaneously compute longwave spectral radiative kernels for temperature and specific humidity at $10cm^{-1}$ interval. The kernel for specific humidity considers TOA spectral flux response to the change of logarithm of specific humidity, i.e., the fractional change of humidity. For this study, we multiply the set of spectral radiative kernels derived in Huang et al. (2014) by atmospheric state perturbations to obtain spectrally resolved λ_Q, λ_{QT} and λ_{QL}. The atmospheric state perturbations are differences between monthly output of first and last 20 years in 80-year 1% CO_2 simulations form 16 models in the CMIP5 archive.

Table 4.1. Summary of the 16 GCMs in CMIP5	
Model name and resolution	Modeling Center
BCC-CSM1.1 (~2.8°×2.8°)	Beijing Climate Center, China Meteorological Administration
BNU-ESM (~2.8°×2.8°)	Beijing Normal University
CanESM2 (~2.8°×2.8°)	Canadian Centre for Climate Modelling and Analysis
CCSM4 (0.9^0×1.25^0)	National Center for Atmospheric Research
CESM1-CAM5 (0.9° × 1.25^0)	National Center for Atmospheric Research
CNRM-CM5 (~1.4^0×1.4^0)	Centre National de Recherches Meteorologiques, France
GFDL-CM3 (2^0×2.5^0)	NOAA Geophysical Fluid Dynamics Laboratory
GISS-E2-H (2^0×2.5^0)	NASA/GISS, USA
GISS-ES-R (2^0×2.5^0)	NASA/GISS, USA
HadGEM2-ES (~1.3^0×1.9^0)	Met Office Hadley Centre
INMCM4 (1.5^0×2^0)	Russian Institute for Numerical Mathematics, Russian
IPSL-CM5A-LR (1.9^0×3.75^0)	Institute Pierre-Simon Laplace
MIROC5 (1.4^0×1.4^0)	Atmosphere and Ocean Research Institute (The University of Tokyo), National Institute for Environmental Studies, and Japan Agency for Marine-Earth Science and Technology
MPI-ESM-LR (1.875^0×1.875^0)	Max Planck Institute for Meteorology
MRI-CGCM3 (1.125^0×1.125^0)	Meteorological Research Institute
NorESM1-M (1.9^0×0.5^0)	Norwegian Climate Centre

Relevant details of the 16 GCMs are in the table 4.1. After longwave spectral feedbacks λ_Q, λ_{QT} and λ_{QL}, are computed, we subtract λ_{QT} and λ_{QL} from λ_Q to obtain the RH feedback λ_H. Also following the method in Held & Shell (2012), a RH spectral radiative kernel can be constructed from radiative kernels of temperature and specific humidity.

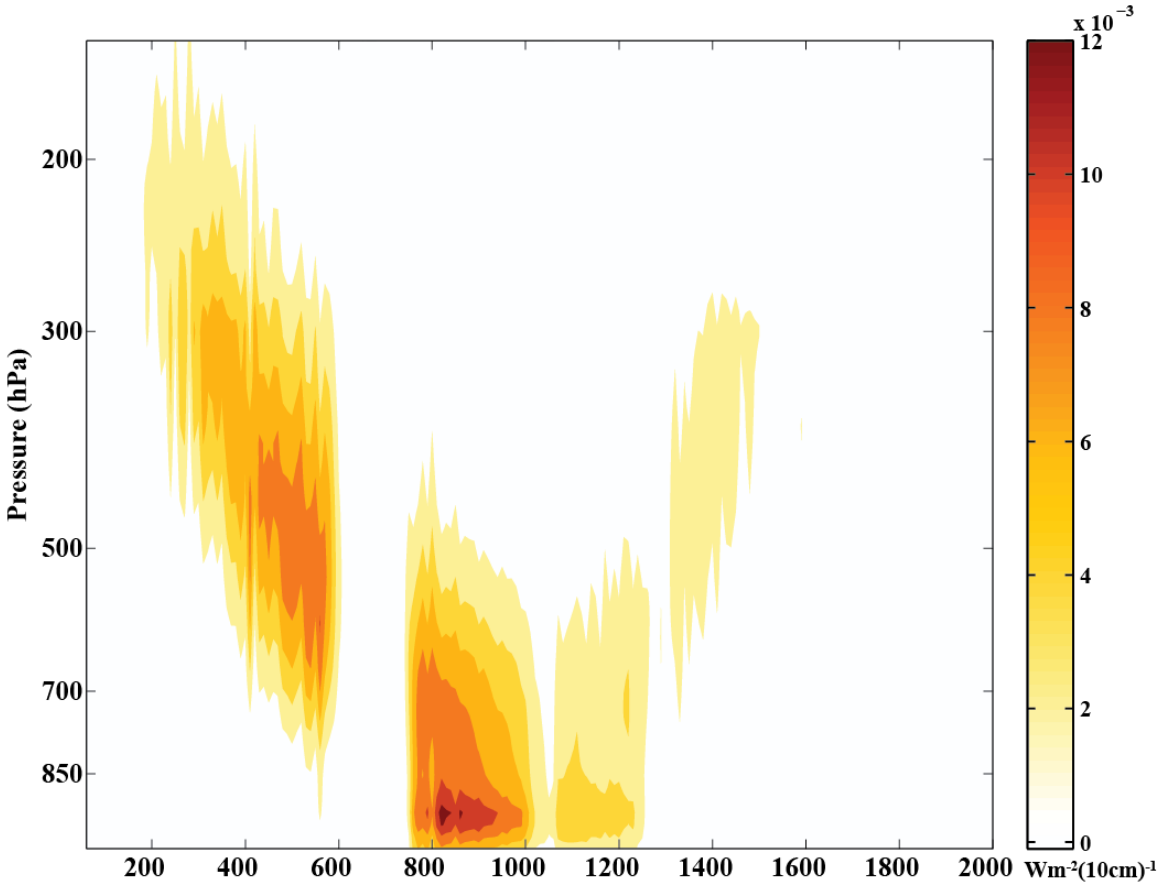

Figure 4.1. The global average spectral radiative kernel for RH. It is the response of global average TOA flux at a given frequency to the fractional change of RH at each pressure level per surface temperature change.

Globally averaged RH spectral radiative kernel derived in this way is show in Fig. 4.1. The RH changes occurring at different levels contribute to radiation changes in different spectral bands. From 60 to 600cm^{-1}, the altitude of RH changes where TOA fluxes are mostly sensitive descends from the upper troposphere to the middle troposphere. In the spectral bands of 800-1200cm^{-1}, the TOA flux is mostly sensitive to the RH changes in the boundary layer.

4.3. Results and Discussion

4.3.1. Features of spectral and spatial distribution of RH feedbacks

Table 4.2. Global average broadband RH feedbacks ($Wm^{-2}K^{-1}$) in 16 CMIP5 GCMs			
BCC-CSM1.1	-0.033	GISS-ES-R	-0.037
BNU-ESM	0.047	HadGEM2-ES	-0.011
CanESM2	0.059	INMCM4	0.0084
CCSM4	-0.062	IPSL-CM5A-LR	-0.022
CESM1-CAM5	-0.094	MIROC5	-0.0027
CNRM-CM5	-0.018	MPI-ESM-LR	0.21
GFDL-CM3	-0.021	MRI-CGCM3	-0.071
GISS-E2-H	0.036	NorESM1-M	-0.076

Table 4.2 lists the global average broadband RH feedbacks of the 16 CMIP5 models, which are obtained by integrating spectral RH feedbacks over the wavenumber on the whole spectrum. All broadband RH feedbacks are approximate to zeros. The average of broadband RH feedback in all models is only -0.0009 $Wm^{-2}K^{-1}$ with a standard deviation of 0.07$Wm^{-2}K^{-1}$. Figure 4.2a shows spectral details of the global average RH feedbacks from the 16 individual models and Fig. 4.2b shows model-mean spectral RH feedback and the standard deviation. The most striking feature in Fig. 4.2a is that spectral RH feedbacks of different GCMs vary quite differently with the frequency, even with their broadband results being alike. As evident from Fig. 4.2, spreads among models are large over a majority part of the longwave spectrum. For a model with positive (negative) broadband RH feedback, its spectral decomposition is not necessarily always positive (negative) as shown in Fig. 4.2a.

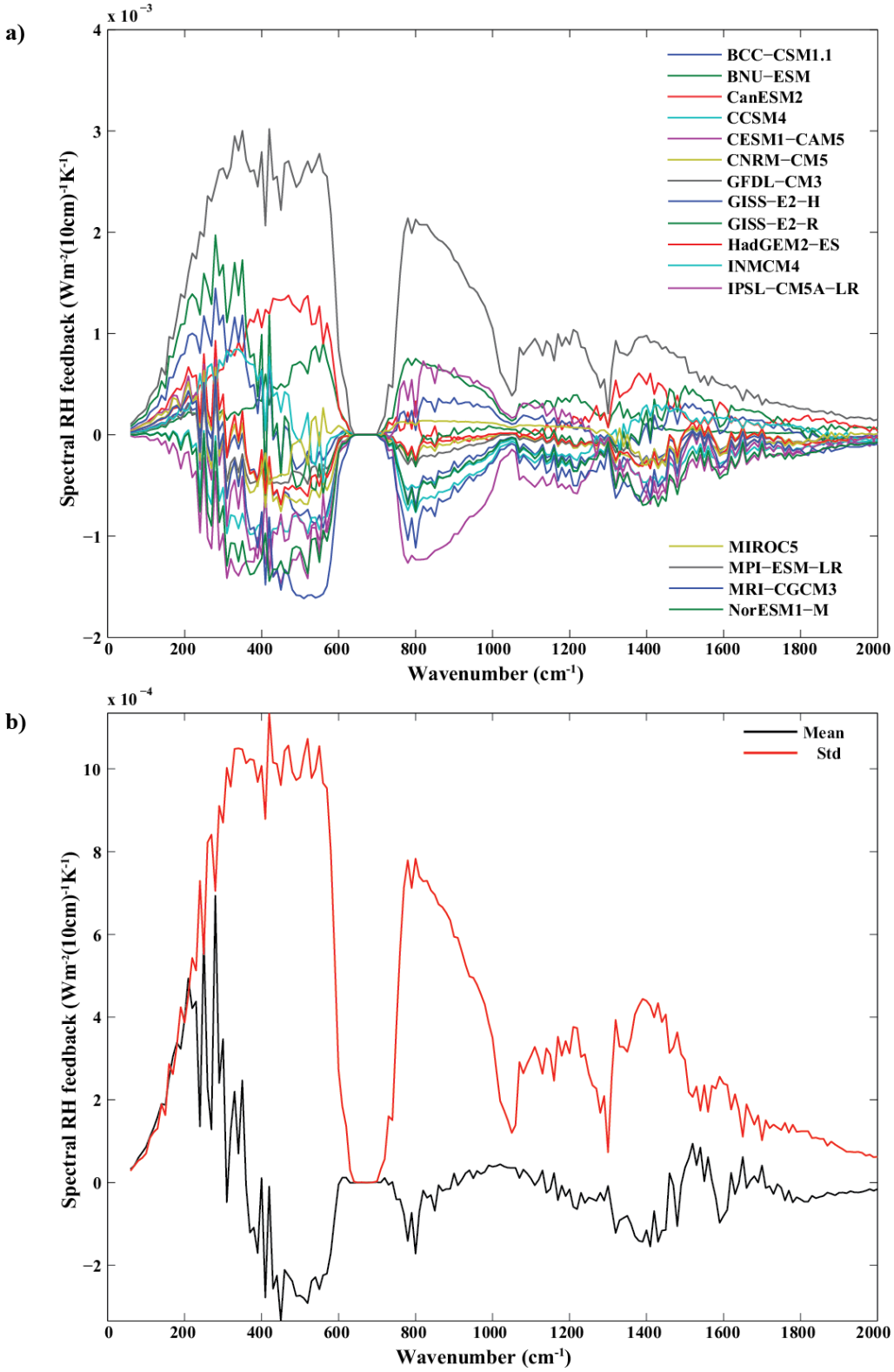

Figure 4.2. (a) Global average spectral RH feedbacks from the 16 GCMs in CMIP5 archive. (b) Mean value and standard deviation of global average spectral RH feedbacks from the 16 GCMs.

Figure 4.3 shows the global map of model- mean broadband RH feedbacks and spectral RH feedbacks over different spectral bands: 60-300, 400-600, and 800-1100cm^{-1}. Areas with statistically significant non-zero RH feedbacks (1% significance level based on student's t-test) are stapled with dots.

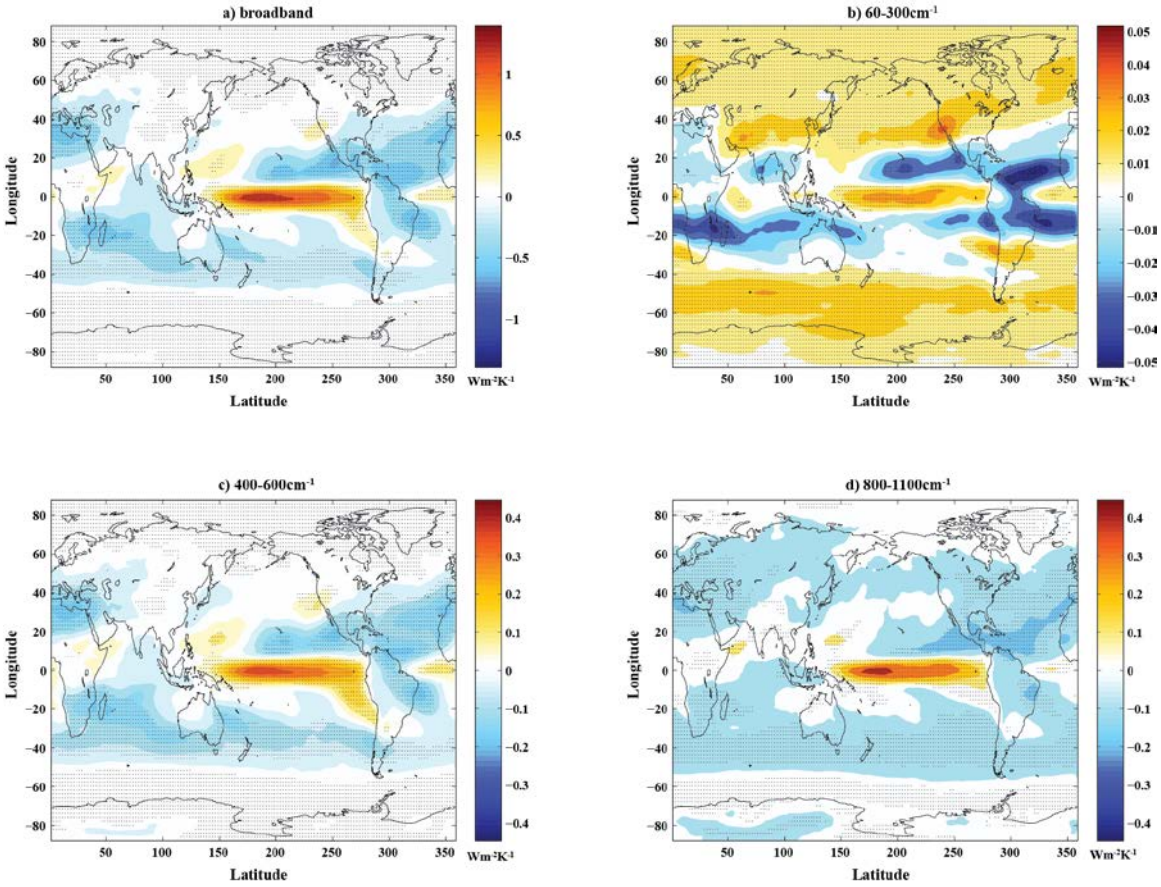

Figure 4.3. The global map of model-mean RH feedbacks from the 16 GCMs over different spectral bands: a) broadband (60-2000cm^{-1}); b) 60-300cm^{-1}; c) 400-600cm^{-1}; d) 800-1100cm^{-1}; The areas where RH feedbacks are nonzero at 1% significance level are marked by dots.

Two major findings can be concluded from Figure 4.3: first, for all spectral bands shown here, the magnitude of local RH feedback is much greater than that of global average. The globally averaged nearly zero RH feedback is a result of spatial compensation and spectral compensation. It is obvious from Fig. 4.3 that some regions exhibit positive RH feedbacks

and some regions, negative RH feedbacks. Second, spatial distribution of the RH feedbacks varies with the spectrum. In the spectral band of 60-300cm^{-1}, the most noticeable patterns are the positive RH feedbacks at high latitudes in both hemispheres and negative RH feedbacks in the tropical Atlantic (5-20°N and 5-20°S). In spectral regions above 300 cm^{-1}, the spatial patterns of RH feedbacks change significantly, with most positive feedbacks confined in the deep tropical Pacific and slight negative feedbacks everywhere else. Except the RH feedback patterns mentioned above, in other locations like mid-latitude and subtropics at around 20-40° in both hemispheres, GCMs behave inconsistently from each other and it is difficult to predict whether the RH feedbacks are positive or negative under global warming.

4.3.2 Relationships between the spectral RH feedbacks and geophysical variables

The global average RH kernel in Fig. 4.1 demonstrates that radiation changes in different spectral bands are contributed from RH changes occurring on different levels. In section 4.3.1 we find varied spatial patterns of RH feedbacks in different spectral bands, and thus we infer that spatial patterns of RH changes on multiple pressure levels could also be different. Figure 4.4 separately demonstrates model-average global map of the RH changes at 300, 500 and 850hPa. Similar to Fig. 4.3, the areas where the mean RH changes are significantly deviated from zeros by student's t-test (at 1% significance) are marked by dots. On 300hPa, the GCMs exhibit significant increase of RH in the high latitude while decrease of RH in the Atlantic tropics (5-20°N and 5-20°S). At 500hPa, in the high latitude, we see nearly little RH change with the most obvious feature being increased RH in the deep tropical Pacific. At 850hPa, except still significant increase of RH in the deep tropical Pacific and

several regions of decreased RH in subtropics, there is little significant change of RH in other regions among GCMs. These features of RH changes on multiple pressure levels are consistent with patterns of significant RH feedbacks mentioned in subsection 4.3.1.

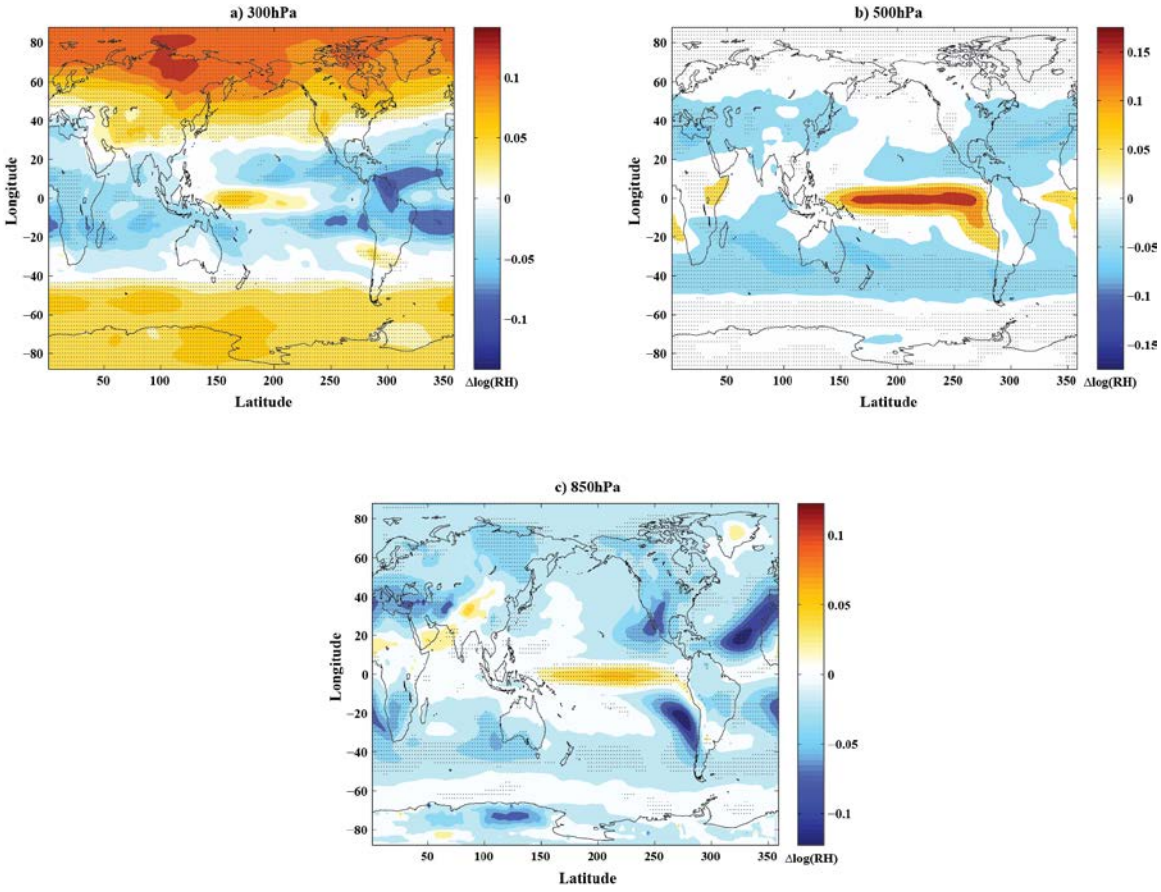

Figure 4.4. The global map of model-mean fractional change of RH among 16 GCMs from the year 1-20 to year 60-80 in the 1% CO_2 experiments at a) 300hPa; b) 500hPa; c) 850hPa. The areas where the RH changes are nonzero at 1% significance level are marked by dots.

Motivated by the statistically significant nonzero spectral RH feedbacks in high latitudes, tropical Atlantic and deep tropical Pacific, we further infer RH changes from spectral RH feedbacks in these regions by inverting the spectral radiative kernel **K** mentioned in equation 4.2. We utilize two methods to solve this inversion problem, which are constrained inversion method and truncated SVD (singular value decomposition) method

introduced in Appendix A. However, before we want to retrieve the regional RH changes from spectral RH feedbacks, one inherent assumption must be validated, that is, the local averages of TOA flux changes due to RH perturbations need to be close enough to approximate results of multiplying locally averaged spectral RH kernels and locally averaged perturbations of RH profiles. The section Appendix B discusses how to test this assumption and whether the assumption is valid in the chosen regions.

4.3.2.1 High latitudes (60-90^{0}S, 60-90^{0}N)

The left columns in Figure 4.5a and 4.5b show the mean value and standard deviations of regional spectral RH feedbacks among 16 GCMs in the high latitude on both hemispheres. For spectral RH feedbacks in the high latitudes, there are two features: 1) the RH feedbacks are positive almost across the whole spectrums, and to a large degree models agree on RH change predictions; 2) broadband RH feedbacks are dominantly contributed from spectral region in the 60-600cm^{-1} and 1200-200cm^{-1}. But in 800-1200cm^{-1}, spectral RH feedbacks in the northern hemisphere behave a little differently from that in the northern hemisphere if we compare the mean value to the standard deviation: in the southern hemisphere GCMs predict small but consistent positive RH feedbacks while in the northern hemisphere GCMs disagree whether the RH feedbacks are positive or negative. From the left columns in Fig. 4.5a and 4.5b, we can infer that in the high latitudes, RH changes are positive and dominant in the upper troposphere. For RH changes in the boundary layer, they could more spread among the GCMs in the northern hemisphere than in the southern hemisphere.

The right columns in Fig. 4.5a and 4.5b separately show mean profiles of regional RH changes in both hemispheres output from 16 GCMs and counterparts retrieved from

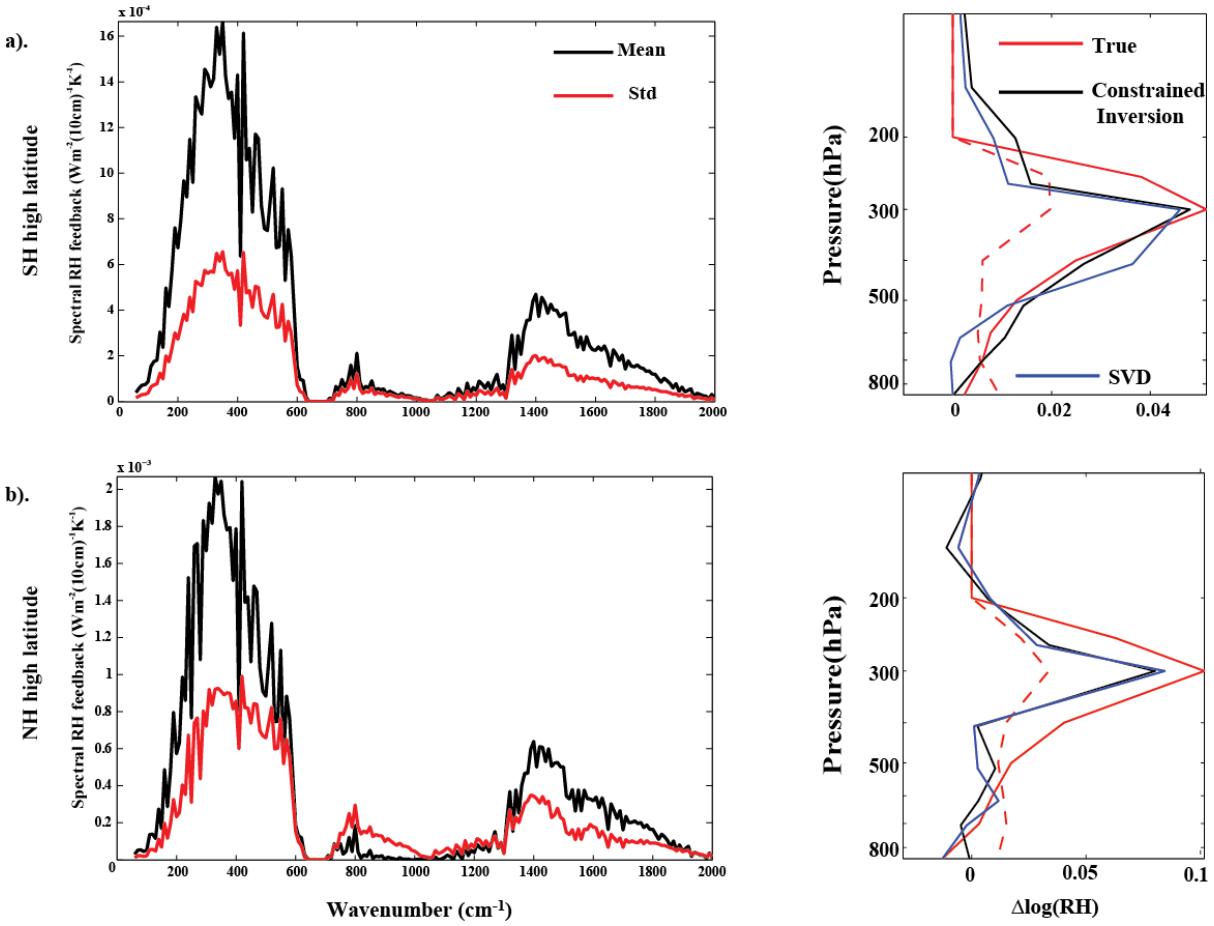

Figure 4.5. (Left column) Mean value (black line) and standard deviation (red line) of regional spectral RH feedbacks among 16 GCMs in the a) high latitude in the southern hemisphere; b) high latitude in the northern hemisphere. (Right column) Model-mean profiles of regional RH changes from the year 1-20 to year 60-80, output from the 1% CO_2 experiments of 16 GCMs (red line), retrieved from the regional spectral RH feedbacks by constrained inversion method (black line), and retrieved by truncated SVD method (blue line) in the regions corresponding to left column. The standard deviation of profiles of regional RH changes among the 16 GCMs (corresponding to the red line) is shown by red dash line.

corresponding regional spectral RH feedbacks by the two inversion methods introduced in Section 4.2.2. Both retrieved and true profiles are consistent with our inference of RH changes from the spectral RH feedbacks. First, in the most troposphere, RH changes are positive, and except in the boundary the standard deviations of true RH changes among the

16 GCMs are smaller than the mean value. Secondly, the RH changes are concentrated in the upper troposphere and there are little contributions under 600hPa. Much of RH changes in high latitude could be explained by the gradient of normal RH state and the poleward shift of climate zones, as argued by Sherwood et al. (2010). The evaluations of our retrieved profiles of RH changes are shown in Fig. 4.8a and Fig. 4.8b. The correlation of our retrieved profiles and true ones is located between 0.7-0.9 for most models but the standard deviations of our retrieved RH changes are smaller than the true ones.

4.3.2.2 Tropical Atlantic (5-20^{0}S(N), 300-350^{0}E)

The left columns in Figure 4.6a and 4.6b show the mean value and standard deviations of regional spectral RH feedbacks among the 16 GCMs in the tropical Atlantic on both hemispheres. For most models, spectral RH feedbacks are negative across the whole spectrums. Compared to RH feedbacks in high latitude, there are more variants among the GCMs since in Fig. 4.6a and 4.6b the magnitude of standard deviation is comparable to the mean value. Besides, on the tropical Atlantic Ocean, the contribution to the broadband RH feedbacks from 800-1200cm^{-1} is comparable to those from 60-600cm^{-1} and 1200-2000cm^{-1}. This infers that on the tropical Atlantic Ocean, RH changes are negative at almost all levels and their changes in both boundary layer and free troposphere both contribute to TOA flux changes, which can be seen from the right columns in Fig. 4.6a and 46b. In Fig. 4.6a and 4.6b, there are two peaks of reduction of RH, one is in the boundary layer and the other one is in the upper troposphere (< ~400hPa). However, in the middle troposphere (about between the 500hPa and 600hPa) and near to the tropopause, RH changes are rather

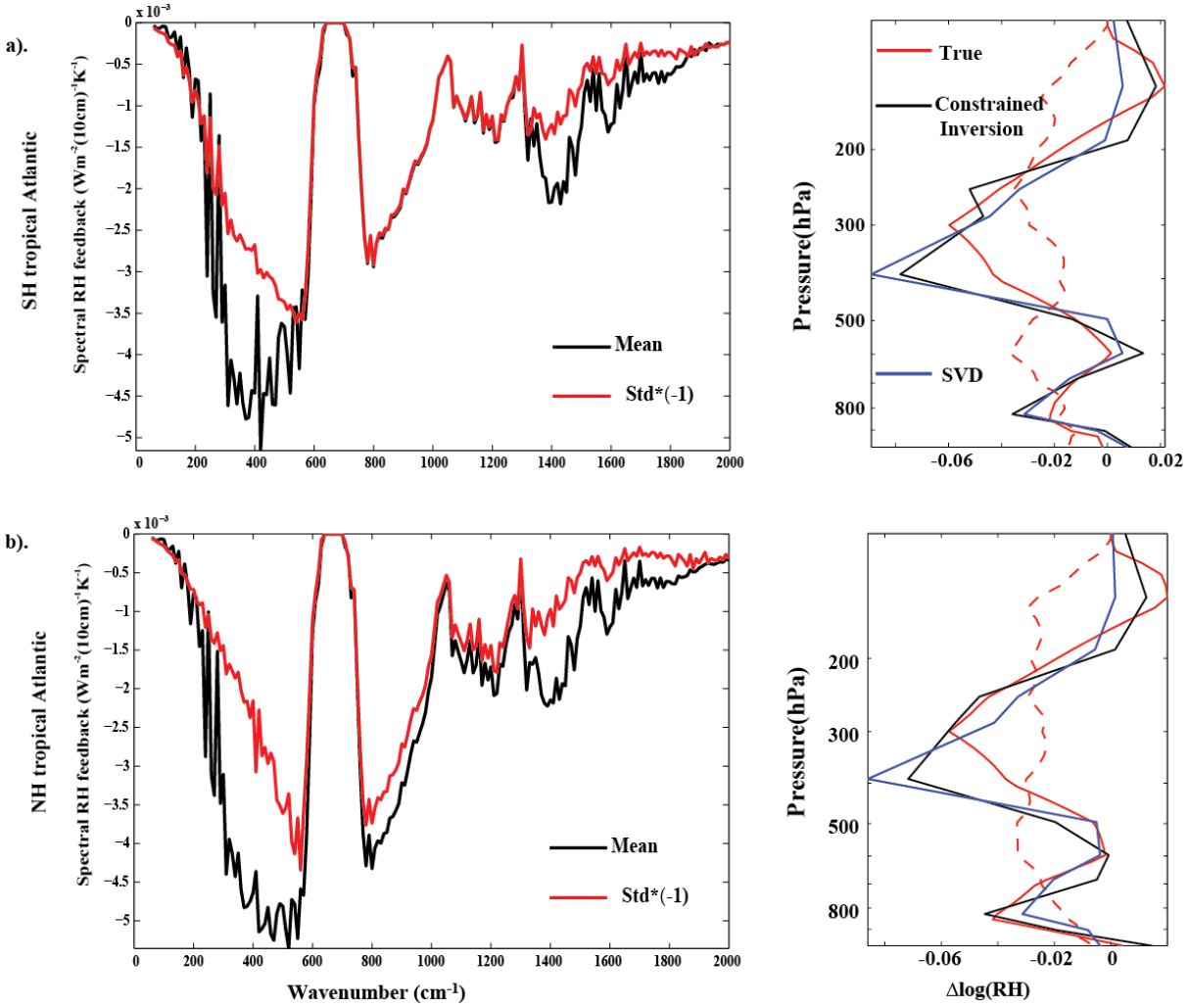

Figure 4.6. Similar to Fig. 4.5 except in the a) tropical Atlantic in the southern hemisphere; b) tropical Atlantic in the northern hemisphere. In the left column, the standard deviation is timed by -1 for the convenience of comparison.

uncertain in the models. These spreads are also revealed in spectral details of RH feedbacks: on the spectrum near to 60cm^{-1} (top troposphere), and near to 600 and 800cm^{-1} (middle troposphere), the standard deviations are close to the mean value. GCMs also predict larger standard deviations than the mean value of RH changes in the top or middle troposphere. The evaluations of our retrieved profiles of RH changes are shown in Fig. 4.8c and Fig. 4.8d. The

correlation of our retrieved profiles and true ones is located between 0.7-0.9 and our retrieved standard deviations are also close to the true ones for most models. However, there are still several models in which the correlation is smaller than 0.7 and the retrieved standard deviations are larger than the true ones. One possible reason for these biases is that the assumption for retrievals mentioned before Section 4.3.2.1 is not so valid in the tropical Atlantic. Discussion about this is in the Appendix B.

4.3.2.3 Deep tropical Pacific (5^0S -5^0N, 200-250^0E)

The left column in Figure 4.7 shows the mean value and standard deviations of regional spectral RH feedbacks in the deep tropical Pacific among the 16 GCMs. Compared to RH feedbacks on the tropical Atlantic Ocean, the spread of spectral RH feedbacks among the GCMs decreases and positive RH feedbacks can be found almost across the whole spectrums. Although RH feedbacks are also positive, their spectral features are different to the spectral RH feedback in the high latitudes. First, the contributions to the broadband RH feedbacks from 800-1200cm^{-1} are much more comparable to the contributions from 60-600cm^{-1}. Second, over 60- 600cm^{-1} the spectral RH feedback in the deep tropical Pacific monotonically increases and abruptly descends to zero when near to 600cm^{-1}, while in the high latitudes, the peak of spectral RH feedback is between 300 and 400cm^{-1}. These features infer that in the deep tropical Pacific Ocean, 1) the RH changes are positive at almost all levels; 2) RH changes in both boundary layer and upper troposphere both contribute to the TOA flux changes; 3) altitude of peaks of RH change could be lower and the RH changes in the middle troposphere could contribute more towards TOA flux changes than counterparts in

the high latitude. The profiles of RH changes in the right column in Fig. 4.7 are also consistent with these inferences. The evaluations of our retrieved profiles of RH changes are

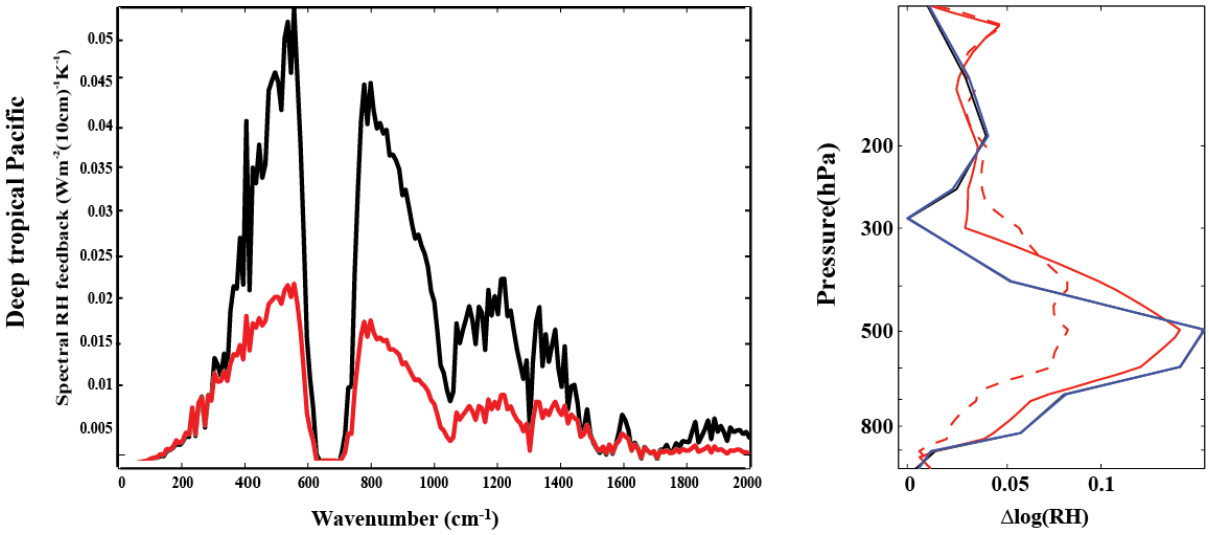

Figure 4.7. Similar to Fig. 4.5 except in the deep tropical Pacific.

shown in Fig. 4.8e and the performance is satisfactory. The correlation of our retrieved profiles and true ones is located near to 0.9 and our retrieved standard deviations are also close to the true ones for most models.

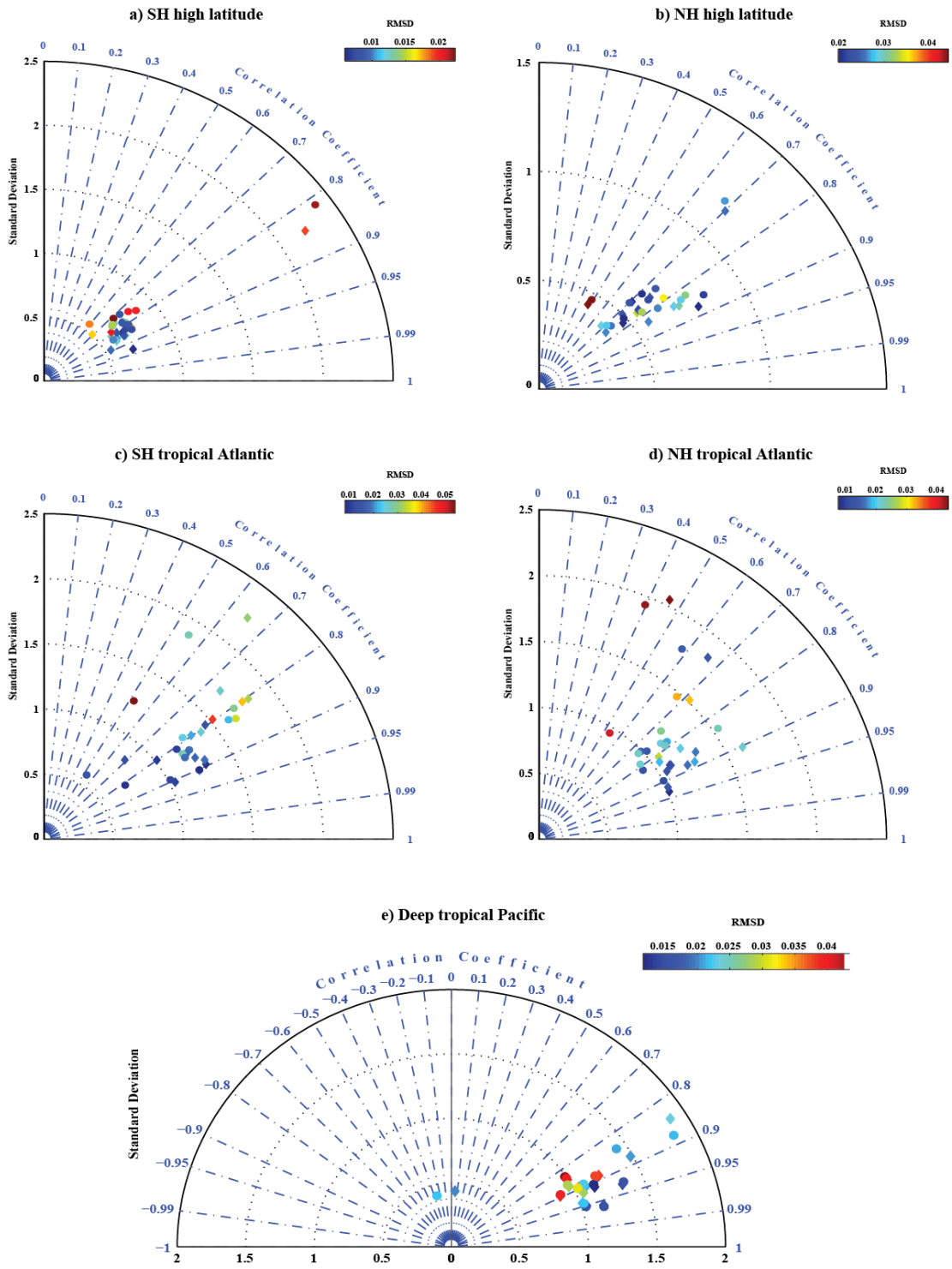

Figure 4.8. Taylor diagrams for the profiles of regional RH changes in the 16 GCMs from the year 1-20 to year 60-80 in five regions. The retrieved profiles of RH changes from the regional spectral RH feedbacks are obtained by constrained inversion method (diamond) and by truncated SVD method (circle). The color demonstrates the root-mean-square deviation from true output of 1% CO_2 experiments from the 16 GCMs.

4.4. Conclusion and Discussion

Applying the spectral radiative kernel technique we derive the spectrally resolved RH feedbacks from 16 GCMs in CMIP5 archives. Although almost all GCMs predict that the global average broadband RH feedbacks are close to zero as expected, the spectral decomposition of broadband feedbacks still reveals wide-spread discrepancies among GCMs. In contrast to little global average broadband RH feedbacks, local average broadband RH feedbacks are much larger and demonstrate some significant spatial patterns. Additionally, these spatial patterns do not keep the same across the whole spectrum. Different spectral regions contribute differently to RH feedbacks. Over the far-IR (60-400cm^{-1}), there exhibit significant positive RH feedbacks in the high latitude while exists negative RH feedbacks in the tropical Atlantic. Over the window region (800-1200cm^{-1}), the most noticeable pattern is the significant positive RH feedbacks in the deep tropical Pacific. In conclusion, the near-zero global average broadband RH feedback is a result of spatial and spectral compensation.

We further utilize the RH radiative kernels to analyze the spectral RH feedbacks over the high latitude, tropical Atlantic and deep tropical Pacific. From the consistence between our retrievals and true profiles of RH change from the GCMs' output, we demonstrate that spectral RH feedbacks can provide more information regarding geophysical variables than normal broadband ones. This also infers that if we can separate observed TOA longwave flux into RH feedbacks, lapse rate feedbacks and other feedbacks, we can also detect the RH changes over a certain spatial and temporal scale (Huang et al., 2010a; 2010b). If we compare the observed TOA longwave flux with the synthetic flux simulated using the atmospheric

profiles from model simulations; we can also attune the errors in simulated geophysical variables from differences in fluxes between observations and simulations.

4.5 Acknowledgement

We acknowledge the modeling groups, the Program for Climate Model Diagnosis and Inter-comparison (PCMDI) and WCRP's Working Group on Coupled Modeling (WGCM) for their roles in making available the WCRP CMIP5 multi-model datasets (Data are available on https://pcmdi.llnl.gov/projects/esgf-llnl).

4.6 Appendix

4.6.1 Appendix A

Two linear inversion methods

To infer **x** from **y** when **y** is approximated by **Kx**, we implement two methods to invert **K** in this chapter. First is the constrained inversion method (Twomey 1977). By this method,

$$\mathbf{x} = (\mathbf{K}^T\mathbf{K} + \lambda\,\mathbf{I})^{-1}\mathbf{K}^T\mathbf{y} \qquad \text{(A4.1)}$$

where **I** is the identity matrix and λ can be obtained by minimizing the Root Mean Square (RMS) deviation after calculating the RMS between the retrieved **x** and true values as a function of λ. In this chapter, the **K** is the spectral RH radiative kernel which relates the TOA flux change **y** to the change of RH profile **x**.

Another method is the truncated SVD (singular value decomposition) method. In SVD decomposition, we express the RH Jacobian **K** in the form:

$$\mathbf{K} = \mathbf{U}\boldsymbol{\Lambda}\mathbf{V}^T \qquad \text{(A4.2)}$$

where **Λ** is the diagonal matrix of singular values and **U** and **V** are orthogonal matrices of its left and right singular vectors. Using this eigenvector basis, the $\mathbf{K}^{-1}$ can be approximately by:

$$\mathbf{K}^{-1} = \boldsymbol{V}_t\boldsymbol{\Lambda}_t^{-1}\boldsymbol{U}_t \qquad \text{(A4.3)}$$

where the subscript *t* means that only *t* largest eigenvalues and their corresponding eigenvectors are remained. The dropped eigenvalues and eigenvectors would greatly

contribute to error terms. The $\mathbf{K}^{-1}$ can relate the RH spectral feedbacks to profiles of RH changes by multiplying $\mathbf{K}^{-1}$ with RH spectral feedbacks and surface temperature

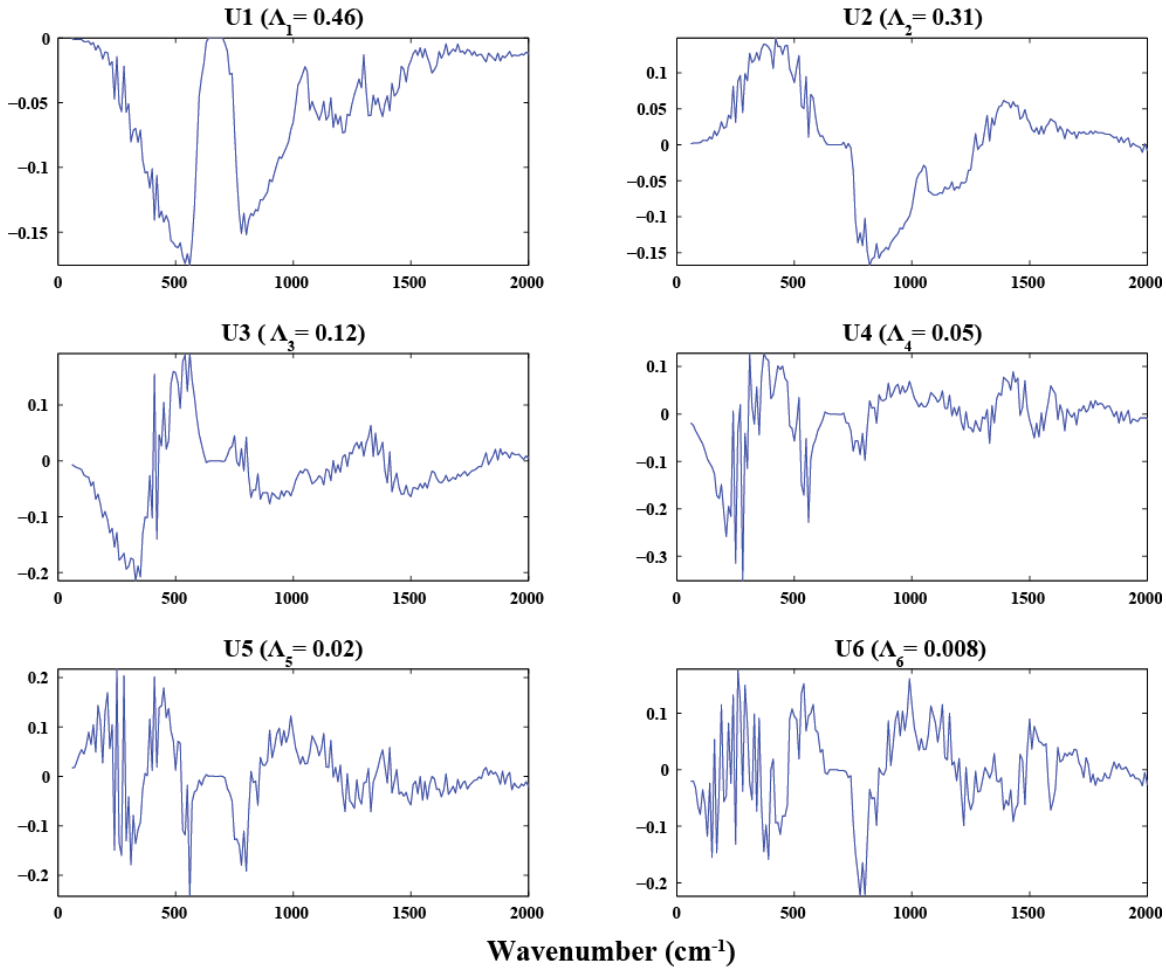

Figure 4.A1. The first six components of left singular vectors from the SVD (singular value decomposition) of global average RH radiative kernels and their corresponding eigenvalues are indicated.

change. Figure 4.A1 and 4.A2 show the first six left singular vectors in **U** and right singular vectors in **V** when their corresponding eigenvalues are in descending order. From the first singular vector in **U** and **V**, negative RH changes through the whole troposphere can be inferred from negative radiation changes across the whole spectrums when contributions in far-IR (60-600cm^{-1}) and window regions (800-1200cm^{-1}) are comparable to each other.

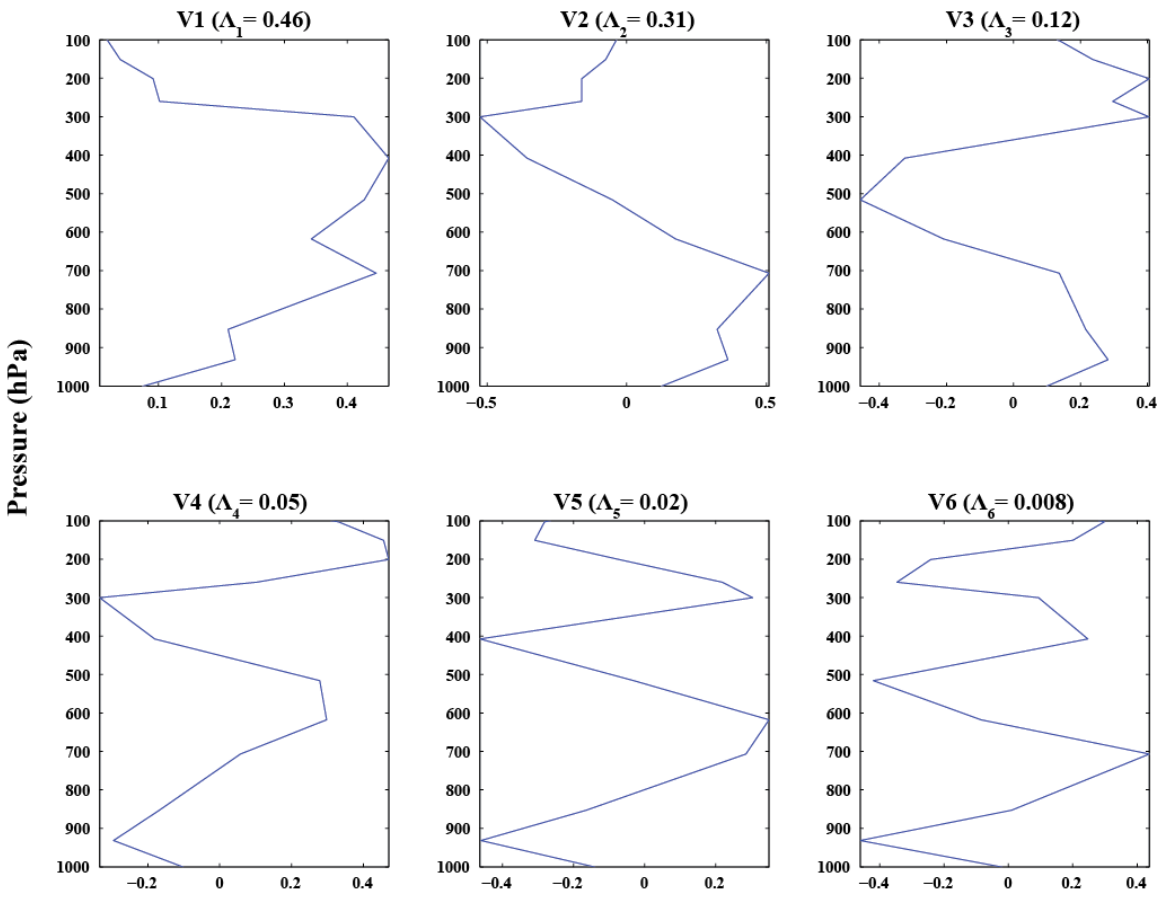

Figure 4.A2. The first six components of right singular vectors from the SVD (singular value decomposition) of global average RH radiative kernels and their corresponding eigenvalues are indicated.

From the second singular vector in **U** and **V**, an increase of RH in lower troposphere while a decrease in upper troposphere can be inferred from positive radiation changes in far-IR while negative changes in window regions.

4.6.2 Appendix B

An assumption in retrieving the average changes of RH profiles from the average changes of TOA fluxes

In subsection 4.3.2 we try to retrieve the regional profiles of 20-year mean RH changes $\overline{\Delta RH(lat, lon, time)}$ in certain region from the local average changes of TOA fluxes $\overline{\Delta R(lat, lon, time)}$ due to the RH perturbations. The retrieval is performed through the local average spectral RH kernel $\overline{K(lat, lon, time)}$. However, the local average changes of TOA fluxes $\overline{\Delta R(lat, lon, time)}$ are obtained in two steps: firstly multiply RH kernel *K(lat, lon, time)* with RH perturbation *ΔRH(lat, lon, time)* to get TOA flux changes Δ*R(lat, lon, time)* on each gridbox (*lat*, *lon*) for every month (*time*) in 20 years; Secondly we spatially and temporally average Δ*R(lat*, *lon*, *time)* to get the $\overline{\Delta R(lat, lon, time)}$. Thus one assumption must be validated before the retrieval:

$$\overline{K \cdot \Delta RH} \cong \overline{K} \cdot \overline{\Delta RH}. \qquad \text{(B4.1)}$$

The left side is the average TOA flux changes $\overline{\Delta R(lat, lon, time)}$ on which we applied the retrieval and the right side is the average changes of RH profiles we would like to obtain.

To test the assumption, we perform the following experiments in each of the five regions in subsection 4.3.2. Firstly, we test whether the equation (B4.1) is validated for spatial average. We get the annual mean perturbations of RH profiles *ΔRH(lat, lon)* in one year and the annual mean spectral RH kernel *K(lat, lon)* on each grid box. Then we get the average $\overline{K(lat, lon)}$, $\overline{\Delta RH(lat, lon)}$, and $\overline{K(lat, lon) \cdot \Delta RH(lat, lon)}$ over all grid boxes. Secondly, we test whether the equation (B4.1) is validated for temporal average in a similar way. We get the monthly locally averaged perturbations of RH profiles in one year *ΔRH(mon)* and the local average of monthly spectral RH kernel *K(mon)*. Then we get the annual mean $\overline{K(mon)}$, $\overline{\Delta RH(mon)}$, and $\overline{K(mon) \cdot \Delta RH(mon)}$ for the 12 months. The average TOA flux

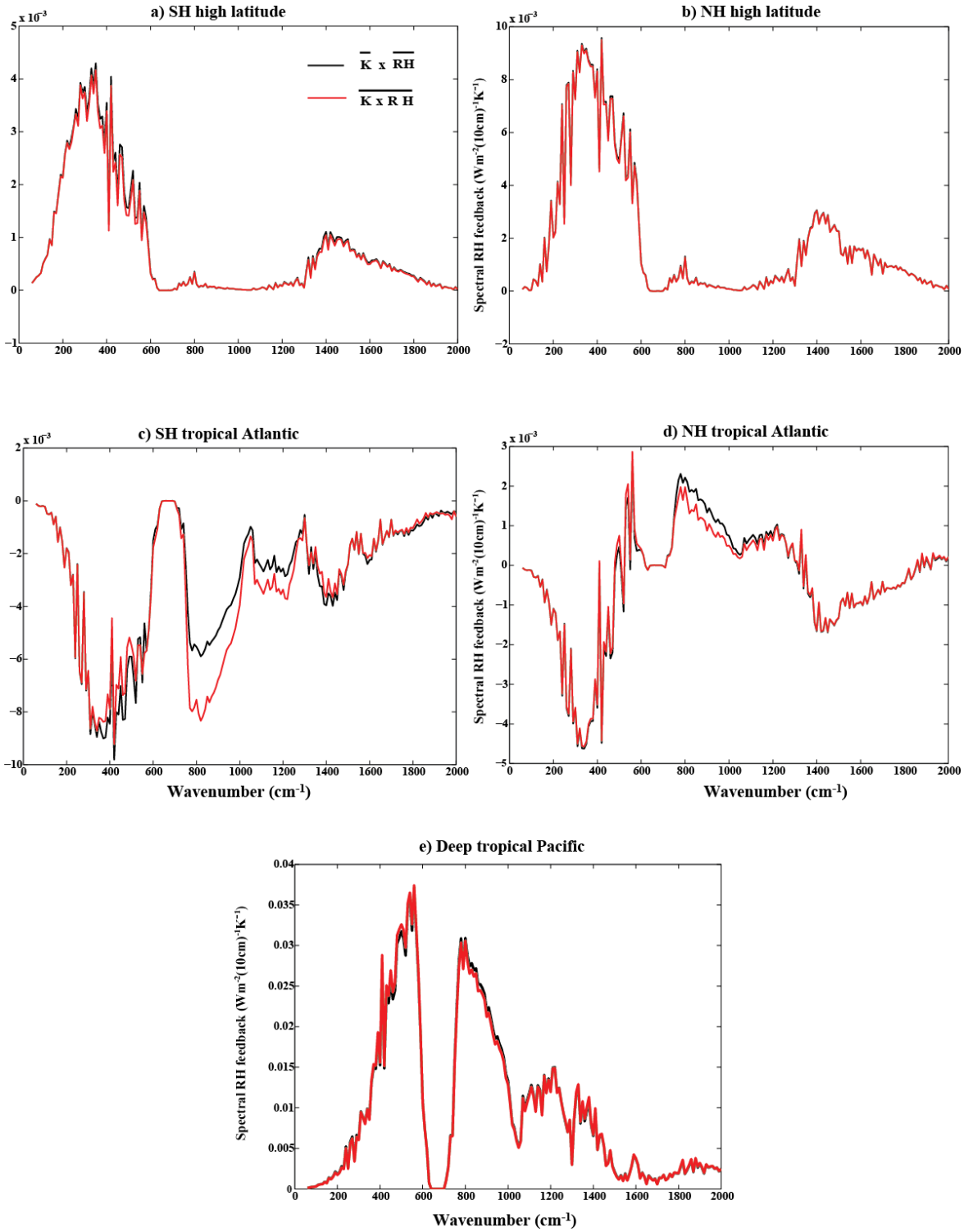

Figure 4.B1. The spatial average of TOA radiance changes due to RH perturbations, i.e., $\overline{K \cdot \Delta RH}$ and $\overline{K} \cdot \overline{\Delta RH}$, in the a) high latitude in the southern hemisphere (60- 90^{0}S); b) high latitude in the northern hemisphere (60-90^{0}N); c) tropical Atlantic in the southern hemisphere (5-20^{0}S, 300-350^{0}E); d) tropical Atlantic in the northern hemisphere (5-20^{0}N, 300-350^{0}E); e) deep tropical Pacific (5^{0}S -5^{0}N, 200-250^{0}E).

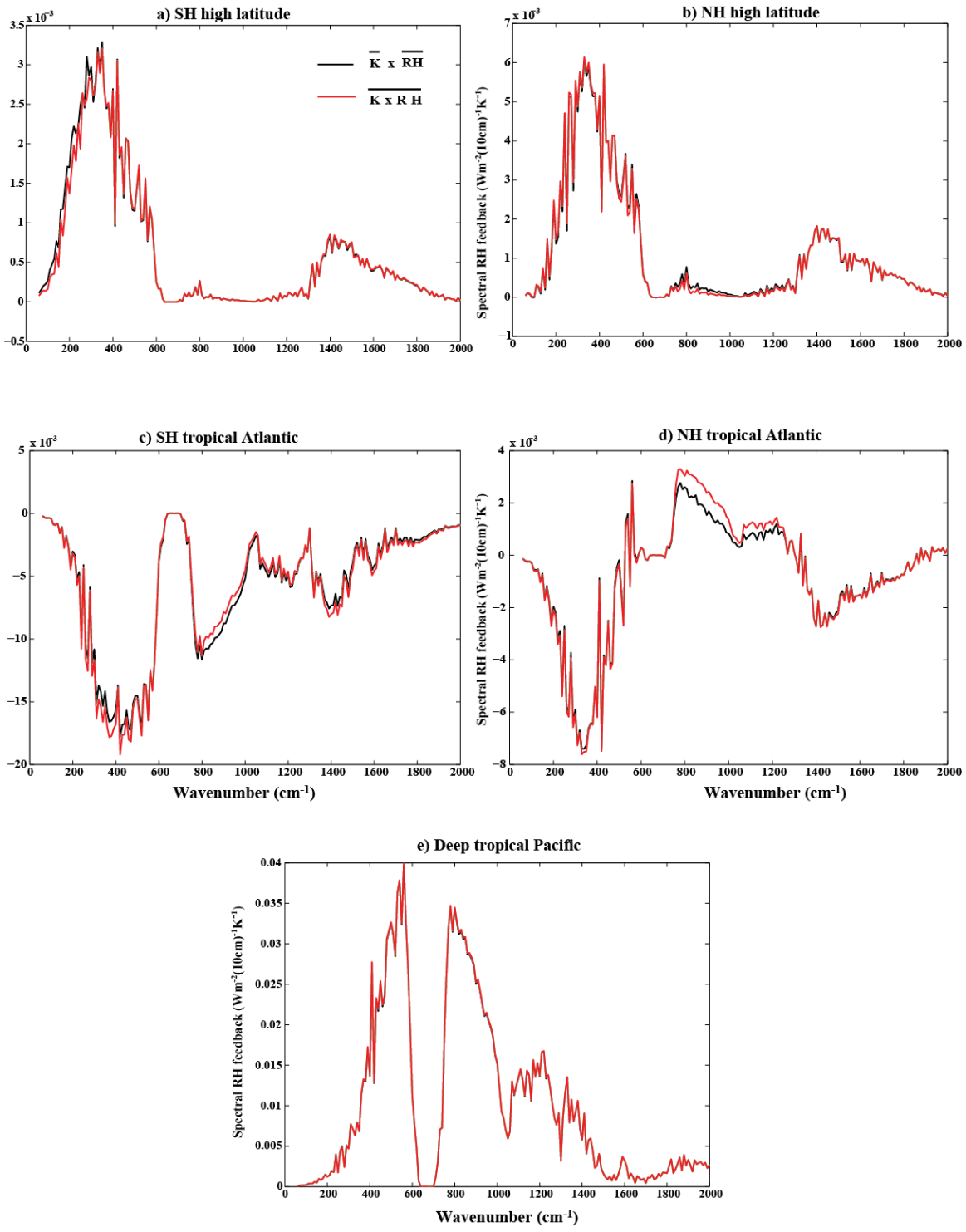

Figure 4.B2. The temporal average of TOA radiance changes due to RH perturbations, i.e., $\overline{K \cdot \Delta RH}$ and $\overline{K} \cdot \overline{\Delta RH}$ in the five regions explained in Fig.4. B1.

changes due to RH perturbations, i.e., $\overline{K \cdot \Delta RH}$ and $\overline{K} \cdot \overline{\Delta RH}$, for spatial average and temporal average are separately shown in Fig. 4.B1 and 4.B2 in the five regions. Over the tropical Pacific Ocean, whatever the operation order, first multiplying *K* and ΔRH and then average or first average *K* and ΔRH and then multiplying, the two lines almost overlap each other. In the high latitudes on both hemispheres, to large degree, the equation (B4.1) is validated. However, over the Sub-Tropical Atlantic Ocean, the operation order matters. The average TOA flux changes by $\overline{K \cdot \Delta RH}$ and $\overline{K} \cdot \overline{\Delta RH}$ are not consistent with each other, which means that our retrieved local average changes of RH profiles are probably deviated from the true values.

Reference

1. Caldwell, Peter M., et al., 2016, Quantifying the sources of intermodel spread in equilibrium climate sensitivity. *Journal of Climate* **29**, 513-524, doi:10.1175/JCLI-D-15-0352.1.

2. Colman, R., and B. J. McAvaney, 1997, A study of general circulation model climate feedbacks determined from perturbed SST experiments. *J. Geophys. Res.*, **102,** 19383–19402.

3. Dessler, A. E., 2010, A determination of the cloud feedback from climate variations over the past decade, *Science* **330**, 1523–1527, doi:10.1126/science.1192546.

4. Frank J. Wentz & Matthias Schabel, 2000, Precise climate monitoring using complementary satellite data sets, *Nature* **403**, 414-416, doi:10.1038/35000184

5. Frank J. Wentz, Ricciardulli. L, Hilburn. K, Mears. C, 2007, How Much More Rain Will Global Warming Bring? *Science* **317**, 233-235, doi: 10.1126/science.1140746

6. GFDL Global Atmospheric Model Development Team, 2004, The new GFDL global atmosphere and land model AM2–LM2: Evaluation with prescribed SST simulations. *J. Clim.*, **17**, 4641–4673.

7. Held, I. M., and B. J. Soden, 2000, Water vapor feedback and global warming. *Annu. Rev. Energy Environ.*, **25,** 441–475, doi: 10.1146/annurev.energy.25.1.441

8. Held, Isaac M., and Karen M. Shell, 2012, Using relative humidity as a state variable in climate feedback analysis. *Journal of Climate* **25**(8), 2578-2582. doi: 10.1175/JCLI-D-11-00721.1

9. Huang, X., X. Chen, B. J. Soden, and X. Liu, 2014, The spectral dimension of longwave feedback in the CMIP3 and CMIP5 experiments, *Geophys. Res. Lett.*, **41**, 7830–7837, doi:10.1002/2014GL061938.

10. Huang, Y., S. Leroy, P. J. Gero, J. Dykema, and J. Anderson, 2010a, Separation of Longwave Climate Feedbacks from Spectral Observations, *J. Geophys. Res*., **115**, D07104, doi:10.1029/2009JD012766.

11. Huang, Y., S. S. Leroy, and J. G. Anderson, 2010b, Determining longwave forcing and feedback using infrared spectra and GNSS radio occultation, *J. Climate*,. **23**, 6027-6035, doi:10.1175/2010JCLI3588.1.

12. Ingram, W. J., 2002, On the robustness of the water vapor feedback, GCM vertical resolution and formulation. *J. Clim.* **15**, 917–921.

13. Liu X., W. L. Smith, D. K. Zhou, and A. Larar, 2006, Principal component-based radiative transfer model for hyperspectral sensors: theoretical concept. *Appl. Opt.*,**45,** 201-209.

14. Myles R. Allen & J. I. William, 2002, Constraints on future changes in climate and the hydrologic cycle, *Nature***419**, 224-232, doi:10.1038/nature01092.

15. Pierrehumbert, R.T., Brogniez, H. and Roca, R., 2007. On the relative humidity of the Earth's atmosphere. *The General Circulation.*

16. Shell, K.M., J. T. Kiehl, and C. A. Shields, 2008, Using the radiative kernel technique to calculate climate feedbacks in NCAR's Community Atmospheric Model. *J. Clim.*, **21**, 2269–2282. doi: 10.1175/2007JCLI2044.1

17. Sherwood, S. C., W. Ingram, Y. Tsushima, M. Satoh, M. Roberts, P. L. Vidale, and P. A. O'Gorman, 2010, Relative humidity changes in a warmer climate, *J. Geophys. Res.*, **115**, D09104, doi:10.1029/2009JD012585.

18. Soden, B. J., and I. M. Held, 2006, An assessment of climate feedbacks in coupled ocean-atmosphere models, *J. Clim.*, **19**, 3354–3360, doi: 10.1175/JCLI3799.1

19. Soden, Brian J., et al., 2008, Quantifying climate feedbacks using radiative kernels. *Journal of Climate* **21**(14), 3504-3520.

20. Soden, B. J., and G. A. Vecchi, 2011, The vertical distribution of cloud feedback in coupled ocean-atmosphere models, *Geophys. Res. Lett.*, **38**, L12704, doi:10.1029/2011GL047632.

21. Trenberth, Kevin E., John Fasullo, and Lesley Smith, 2005, Trends and variability in column-integrated atmospheric water vapor. *Climate dynamics* **24**, 741-758.

22. Twomey, S., 1977: Introduction to the Mathematic of Inversion in Remote Sensing and Indirect Measurements. Elsevier Sciencetific, 242 pp.

Chapter 5

Summary and Future work

5.1 Summary

The main theme explored in this thesis was the direct usage of spectrally resolved radiation in climate studies. This study has examined decadal stratospheric changes through the usage of hyper-spectral infrared radiances observed by AIRS and synthetic radiances based on model simulations and reanalysis data set. Further, the spectral dimension of relative humidity feedbacks among the CMIP5 GCMs has been examined. Main focus of these explorations was what new insights into the climate change and variability we can draw, based on model simulation and reanalysis data, from the spectral dimension of hyper-spectral measurements such as AIRS and their counterparts.

This research began by estimating the linear trends of global-mean radiances at 50 AIRS stratospheric channels in the CO_2 ν_2 band. AIRS radiance measurements were used, so did two sets of synthetic radiances, one based on output from a free-running GFDL AM3 model forced by the observed SST over the same period of AIRS observations and the other based on ECMWF ERA-interim reanalysis. AIRS lower-stratospheric channels have a

cooling trend of no more than 0.23 K decade^{-1} in terms of brightness temperature while its middle-stratospheric channels consistently show a statistically significant cooling trend as large as 0.58 K decade^{-1} in brightness temperature. Regarding the synthetic radiances, the results based on the GFDL AM3 model conform slightly to the trends observed while the trends based on the ERA-interim provide an opposite result. This reaffirms that cautions must be taken in the use of reanalysis stratospheric data in the study of trend and variability over multiple years.

Based on the observed radiance trends above, this study then directly derived actual stratospheric temperature and CO_2 changes in the presence of natural variability using optimal fingerprinting technique (average-then-retrieve approach). This study has demonstrated that it is practical to apply optimal fingerprinting to the observed infrared radiances with high spectral resolution. The rich information in AIRS stratospheric channels improves the vertical resolution of retrieved profile of stratospheric temperature changes. The stratospheric cooling increases with height: the globally average cooling rate in the lower stratosphere (30–59hPa) is 0.39±0.32(2σ) K decade^{-1} and for the two middle stratospheric layers (14–30hPa and 6–14hPa) it is 0.46 K decade^{-1}, respectively, all with a 2-σ uncertainty around 0.23 K decade^{-1}; The cooling rate in the upper stratosphere above 6hPa is 0.65±0.11 K decade^{-1}. Further, in this study it was noted that microwave radiance observed by AMSU can help distinguish between the CO_2 fingerprint and temperature fingerprints and thus synergistic use of microwave and infrared radiances can effectively reduce uncertainties in the estimation of stratospheric temperature and CO_2 changes.

Spectral details in the radiative feedbacks can provide more information about vertical profiles of actual physical variables than the widely used broadband radiative feedbacks. This study has calculated the spectrally resolved relative humidity feedbacks among 16 CMIP5 GCMs utilizing the spectral radiative kernel technique. The spectral decomposition reveals wide discrepancies of RH changes among the GCMs that otherwise could be covered by approximately zero broadband RH feedback over the entire globe. Different spatial regions and spectral bands contribute differently to the broadband RH feedbacks. As a result, the near-zero broadband RH feedback is a result of spatial compensation and spectral compensation. We further applied the average-then-retrieve approach to the simulated spectral flux which is the spectral RH feedback. The profiles of regional RH changes over the high altitude, tropical Atlantic and deep tropical Pacific were inferred using both constrained inversion method and truncated SVD method. They are largely consistent with the true profiles of RH changes as simulated by each individual GCM, which demonstrates feasible "average-then-retrieve" venues to infer changes of actual geophysical variables from spectral observations.

5.2 Future work

This research has demonstrated that the average-then-retrieve approach can be applied on the hyper-spectral infrared radiances from AIRS and passive microwave data from AMSU to detect decadal stratospheric temperature and CO_2 changes. Besides AIRS, other ongoing missions such as IASI and CrIS also provide hyper-spectral infrared radiances with quality comparable or even superior to AIRS. There also has been more than a decade of GPS radio occultation observations (Wichert et al., 2001), which is insensitive to not only CO_2 but also

cloud changes. Synergistic use of GPS occultation and hyper-spectral infrared radiance can be useful for inferring changes in the stratosphere and troposphere. The hyperspectral measurements provide information-rich constraints on long-term trends not only for the stratospheric properties, but also for the tropospheric temperature, humidity, cloud and surface properties. We can extend the application of average-then-retrieve approach from the CO_2 band to other spectral regions for tropospheric climate studies.

However, some problems still exist in the average-then-retrieve approach. These problems include the design of signals, estimates of natural variabilities, construction of error covariance matrix just to mention a few. The objective of future work is to resolve these problems and to improve the method separating the contribution of tropospheric, surface and cloud property changes from the spectral radiance changes.

To achieve this objective, we propose to start with synthetic infrared radiance simulated from the model output. Because the true profiles of tropospheric properties are ready from the model output as training datasets, they enable us to evaluate retrieved tropospheric changes and trace the errors in retrievals. We could simulate time-evolving hyper-spectral infrared radiance through the satellite simulator PCRTM (Principle Component-based Radiative Transfer Model, Liu et al., 2006). This is based on the atmospheric profiles output from GFDL (Geophysical Fluid Dynamics Laboratory) CM3 1% CO_2 experiment. Meanwhile, we could construct natural variability of corresponding spectrum and spectral fingerprints due to the perturbations of tropospheric, surface and cloud properties. This is based on long-term control runs also performed by GFDL CM3.

After all training datasets are prepared; we would detect the tropospheric, surface and cloud property changes from the synthetic infrared radiance and compare them to true changes in model output with the aim of examining retrieval performance. Prior to retrieval we would find the optimal temporal and spatial scale for averaging purposes. Then we would be able to explore how the design of fingerprints like their vertical resolution would affect retrieval results. More importantly, we could get the true error covariance and evaluate the covariance matrix used in the retrieval process.

Other potential improvements in the method are in the fingerprint similarity and the detection of cloud changes. For example, to disentangle fingerprints, we propose to replace the traditional specific humidity with relative humidity to reduce the similarity between temperature and specific humidity fingerprints. In the case of the detection of cloud changes, the possible difficulties that exist are construction of cloud fingerprints and fingerprint ambiguities between clouds and other tropospheric properties. Some potential solutions to these difficulties are worth considering. First, we could construct the cloud fingerprints and separate the cloudy scenes according to the cloud types. Yue et al., (2016) have derived the observation-based longwave cloud radiative kernels for multiple cloud types and used these kernels to estimate the short-term variations of cloud forcing and cloud feedbacks. Second, we could separate clear scenes from cloudy scenes to retrieve temperature and humidity changes. Third, we could consider the complementary use of other observations like microwave radiance, GPS radio occultation data and reflected solar radiances (Jin et al., 2016).

After investigating how to improve the average-then-retrieve approach with synthetic radiances, we would apply it to monitor the changes of tropospheric temperature, humidity, surface and cloud properties from satellite observations. Meanwhile, the improved average-then-retrieve approach also would provide a new opportunity to test climate models more rigorously by comparing the spectrally resolved flux. This research has already revealed how the spectral details in RH feedback are associated with underlying physical processes, and advocated more analysis of radiative feedbacks in the spectral dimension. It is important to highlight that model simulations can provide the signals of Planck feedback, relative humidity feedback, lapse rate feedback and other feedbacks. Subsequently, these signals could be separated from satellite-observed spectra changes through optimal fingerprinting technique and be compared with the corresponding predictions in GCMs. This idea has been investigated in some previous works. Leroy (1998) provided some Bayesian aspects and Huang et al (2010a; 2010b) tested this idea on simulated spectra. Evidently future research can investigate how to directly apply this technique to observed hyper-spectral radiation in the terms of climate feedback constraints.

Reference

1. Huang, Y., S. Leroy, P. J. Gero, J. Dykema, and J. Anderson, 2010a, Separation of Longwave Climate Feedbacks from Spectral Observations, *J. Geophys. Res*., **115**, D07104, doi:10.1029/2009JD012766.
2. Huang, Y., S. S. Leroy, and J. G. Anderson, 2010b, Determining longwave forcing and feedback using infrared spectra and GNSS radio occultation, *J. Climate*,. **23**, 6027-6035, doi:10.1175/2010JCLI3588.1.
3. Jin, Z & M. Sun, 2016, An initial study on climate change fingerprinting using the reflected solar spectra, *J. Climate* **29**(8):2781-2796.

4. Leroy, S. S., 1998, Detecting climate signals: Some Bayesian aspects, *J. Climate*, **11**, 640-651.

5. Liu X., W. L. Smith, D. K. Zhou, and A. Larar, 2006, Principal component-based radiative transfer model for hyperspectral sensors: theoretical concept. *Appl. Opt.*,**45,** 201-209.

6. Wickert, J., et al., 2001. Atmosphere sounding by GPS radio occultation: First results from CHAMP. *Geophys. Res. Lett*, **28**(17): 3263-3266.

7. Yue, Q, et al., 2016, Observation-based Longwave cloud radiative kernels derived from the A-Train. *J. Climate* **29**(6):2023-2040.